

**Structural studies on geometrically frustrated
systems: AlV_2O_4 and LiMn_2O_4 - Role of temperature,
pressure and chemical substitution**

By

S. Kalavathi

(Enrollment No: PHYS02200704024)

**Indira Gandhi Center for Atomic Research,
Kalpakkam -603102, Tamil Nadu, India**

*A thesis submitted to the
Board of studies in Physical Sciences
In partial fulfillment of requirements
For the Degree of*

DOCTOR OF PHILOSOPHY

of

**HOMI BHABHA NATIONAL INSTITUTE
Mumbai**



August, 2013

Homi Bhabha National Institute

Recommendations of the Viva Voce Board

As members of the Viva Voce Board, we certify that we have read the dissertation prepared by **Ms. S. Kalavathi** entitled “**Structural studies on geometrically frustrated systems: AlV_2O_4 and LiMn_2O_4 - Role of temperature, pressure and chemical substitution**” and recommend that it may be accepted as fulfilling the dissertation requirement for the Degree of Doctor of Philosophy.

_____ **Date:**

Chairman – C. S. Sundar

_____ **Date:**

Convener/Guide – P. Ch. Sahu

_____ **Date:**

External Examiner

_____ **Date:**

Member – A. Bharathi

_____ **Date:**

Member – A. K. Arora

Final approval and acceptance of this dissertation is contingent upon the candidate's submission of the final copies of the dissertation to HBNI.

Date:

Place:

CERTIFICATE

I hereby certify that I have read this dissertation prepared under my direction and recommend that it may be accepted as fulfilling the dissertation requirement.

Date:

(P.Ch. Sahu)

Place:

Thesis Supervisor

STATEMENT BY AUTHOR

This dissertation has been submitted in partial fulfillment of requirements for an advanced degree at Homi Bhabha National Institute (HBNI) and is deposited in the Library to be made available to borrowers under rules of the HBNI.

Brief quotations from this dissertation are allowable without special permission, provided that accurate acknowledgement of source is made. Requests for permission for extended quotation from or reproduction of this manuscript in whole or in part may be granted by the Competent Authority of HBNI when in his or her judgement the proposed use of the material is in the interests of scholarship. In all other instances, however, permission must be obtained from the author.

(S. Kalavathi)

DECLARATION

I, hereby declare that the investigation presented in the thesis has been carried out by me. The work is original and has not been submitted earlier as a whole or in part for a degree / diploma at this or any other Institution / University.

(S. Kalavathi)

... to all those who yearn for free thought, liberation and autonomy

ACKNOWLEDGEMENTS

I would like to place on record my deep sense of gratitude to my thesis supervisor Dr. P. Ch. Sahu, a soft spoken gentleman who made it appear an easy feat to overcome my 'high pressure days' and "Herculean moments". My salutations to him for the silent, but solid, support he rendered throughout the thesis work and also for the eagerness and speed he evinced in aiding me meet all the deadlines.

Dr. H K Sahu, deserves my whole hearted thanks for initiating discussions on 'frustrated systems' that motivated me to take up this thesis work. Many discussions with him have enriched my understanding.

I am grateful to Sri. V Sankara Sastry, my Thesis Advisor and former Head, X-Ray Crystal Growth Section, for his total support and encouragement. Thanks to him especially for introducing me to finer aspects of experimentation when I made a transition from superconductivity to diffractometry.

My special thanks to Prof. Quentin Williams, University of California, for many an e-discussion during the high pressure experiments. I thank Dr. Selva Vennila Raju, Dr. A K Sinha and Sri. Manvendra Narayan Sing for their support during synchrotron experiments. I thank the beam line in-charge of BL 12.2.2 , LBNL, USA, West B1-CHESS, USA and the Head, ISUD, INDUS-2, Indore for allotting beam time for my experiments. Thanks are to Dr. Awadesh Mani and Sri. T R Devidas for the resistivity measurements, Dr. S Amirtha Pandian for Electron Energy Loss Spectroscopic measurements and Dr. Sharat Chandra for electronic structure calculations. Thanks to Dr. Antony Arulraj for his useful tips in Rietveld refinement of synchrotron powder diffraction data. I thank Dr. P K Ajikumar, Dr. M Kamruddin and Dr. T R Ravindran for many TG-DTA and Raman measurements.

I am thankful to the Chairman and to all the members of the Doctoral committee for their valuable suggestions. I thank Dr. C S Sundar, Director, Materials Science, Group, Sri. S C Chetal former Director, IGCAR and Dr. P R Vasudeva Rao, Director IGCAR for permitting me to use the facilities in the center for pursuing my research work.

It is a very different experience taking up a thesis work along with one's daughter and erstwhile students. I thank my daughter M S Upasana, M.S, and my students R Govindarajan and E Jeya Prasath for taking time out of their thesis work to share anecdotes and cheer me up. Thanks to my son K S Swaparjith and my present students G Gopinath, V Manikandan and S Murugan for putting up with my time constraints.

My heart felt thanks to Lalitha Ganesan, for her support especially during the last few months, in maintaining the home front and giving me the leisure to focus on writing the thesis.

I thank my dear sisters, affectionate sisters-in-law and brothers-in-law for their periodic enquiries about the progress of my thesis work and for their words of encouragement.

I must thank Ms. Soumee Chakraborty, Mr. Karthikeyan, Ms. Madhu Smita Sahu and Mr. Hirojith Loushambam, the younger members also doing their thesis work in MSG, for giving rejuvenating company during all the days that I stayed late in the laboratory and for infusing their youthful energy into me.

My sincere thanks to Dr. S Tripura Sundari and Dr. R Ramaseshan for their suggestions and help in improving the style of presentation of the thesis.

I thank Sri. R Baskaran, Sri D V Natarajan, Sri R V Subba Rao Dr. S. Ilango, Dr G Amarendra, Dr. J Janaki, O Annalakshmi and Ms T Jayanthi my good friends, for their concern and care.

Dr. T S Radhakrishnan, always wanted me to take up and complete my Ph.D ever since I joined the department. He introduced me to all the nuances of low temperature experiments during my nearly two decades of work in the Low Temperature Lab. I thank him for this. I also owe a lot to Sri M P Janawadkar and Sri M C Valsakumar for their elucidation of the theoretical aspects that assisted me in savouring the subtleties involved.

I thank all the members and colleagues of MSG with whom I have shared three decades of my enjoyable and unexchangeable professional life. Special thanks to my colleagues in XCGS for their co-operation.

I thank my life partner, Sridhar V, for standing shoulder to shoulder in all my endeavors. I owe a lot to him for helping me consolidate my thoughts, views and dreams by his non stop, sometimes frustrating, but on the whole liberating, critical questions. His exercises in converting idealism to actionable forms within the given boundary conditions, his incessant attempts to move the boundaries to give more breathing space for idealism to survive in its pristine form, his restless mind that constantly thinks and works for ameliorating the struggles of first generation learners and his effervescent never-say-die spirit will forever remain a permanent source of inspiration.

(S. Kalavathi)

| CONTENTS | | Page No. |
|------------------|--------------------------------------------------------------------------------------------------------------------------|---------------------|
| CHAPTER 1 | Geometrically frustrated spinel systems and ordering of charges – A brief review | 1 |
| 1.1 | The concept of Geometrical frustration – Historical development | 2 |
| 1.2 | Geometric frustration in ‘water ice’ | 5 |
| 1.3 | Cation ordering in the pyrochlore spinel sub-lattice and the Verwey transition | 8 |
| 1.4 | A short review of the spinel oxides exhibiting charge frustration | 10 |
| 1.4.1 | Recent results of structural analysis of Fe_3O_4 below Verwey transition | 10 |
| 1.4.2 | Columnar ordering of charges in LiMn_2O_4 | 12 |
| 1.4.3 | Octamer formation in CuIr_2S_4 | 14 |
| 1.4.4 | Novel heptamer formation in AlV_2O_4 | 15 |
| 1.4.5 | Frustration to order in LiRh_2O_4 | 18 |
| 1.5 | Short summary of the spinel compounds exhibiting charge order from frustration | 20 |
| | Motivation and thesis organisation | 22 |
| CHAPTER 2 | Sample preparation, characterization and high temperature powder XRD study of AlV_2O_4 | 26 |
| 2.1 | Introduction | 26 |
| 2.2 | Details of the laboratory diffractometer, alignment calibration and high temperature attachment | 28 |
| 2.2.1 | Description, alignment and calibration of the laboratory source powder diffractometer | 28 |
| 2.2.2 | The High temperature attachment for powder diffraction | 32 |
| 2.3 | Characterization of the sample | 34 |
| 2.3.1 | Powder XRD characterization | 34 |
| 2.3.2 | Identification of structural model | 38 |
| 2.3.3 | Confirmation of structure using electron diffraction | 41 |
| 2.4 | Rietveld refinement | 42 |
| 2.5 | High temperature powder XRD experiments | 45 |
| | Summary of results and conclusions | 48 |
| CHAPTER 3 | Pressure induced frustration in charge ordered spinel AlV_2O_4 | 50 |
| 3.1 | Introduction | 50 |
| 3.2 | A brief review of the effect of pressure on the charge frustrated spinel compounds | 52 |
| 3.3 | High pressure powder diffraction studies on AlV_2O_4 | 54 |
| 3.3.1 | Diamond anvil cell assembly and experimental details | 54 |
| 3.3.2 | Transformation of AlV_2O_4 from rhombohedral to cubic structure | 55 |
| 3.3.3 | Rietveld Refinement of powder diffraction data under non-hydrostatic pressure | 57 |
| 3.3.4 | Variation of lattice parameter under non-hydrostatic pressure | 59 |
| 3.4 | Hydrostatic pressure studies on AlV_2O_4 | 61 |

| | | |
|------------------|--------------------------------------------------------------------------------------------------------------------------------------------------------------|------------|
| 3.4.1 | Details of the experiment | 61 |
| 3.4.2 | Structural transformation confirmed under hydrostatic pressure | 61 |
| 3.4.3 | Variation of volume/formula unit under hydrostatic pressure | 63 |
| 3.4.4 | Equation of state (EOS) of the charge ordered rhombohedral phase | 65 |
| 3.5 | Discussion of the results of the high pressure experiments on AlV_2O_4 | 66 |
| | Summary and conclusions | 70 |
| CHAPTER 4 | Valence state, hybridization and electronic band structure in the charge ordered AlV_2O_4 | 72 |
| 4.1 | Details of the charge ordered structure of AlV_2O_4 | 72 |
| 4.2 | Vanadium Orbitals and Electron Energy Loss Spectroscopy | 74 |
| 4.2.1 | Hybridization of vanadium–oxygen orbitals in AlV_2O_4 | 74 |
| 4.2.2 | Electron energy loss spectroscopy - technique | 76 |
| 4.2.3 | Electron energy Loss spectroscopy studies on AlV_2O_4 and other vanadium oxides | 79 |
| 4.2.3.1 | EELS spectrum of the charge ordered AlV_2O_4 | 79 |
| 4.2.3.2 | EELS spectrum of the other vanadium oxides | 80 |
| 4.2.3.3 | The white line ratio | 81 |
| 4.2.3.4 | The shift in excitation edge | 83 |
| 4.2.3.5 | Comparison of oxygen K- edge | 84 |
| 4.3 | Band structure calculation | 86 |
| 4.3.1 | Parameterization of the electronic structure calculation on AlV_2O_4 | 86 |
| 4.3.2 | Band structure of the rhombohedral and cubic phase of AlV_2O_4 | 89 |
| 4.3.3 | Density of states of the rhombohedral and cubic phase of AlV_2O_4 | 91 |
| 4.3.4 | Charge disproportionation in AlV_2O_4 | 93 |
| 4.3.5 | Corroboration from band structure calculation for pressure and temperature driven frustration in AlV_2O_4 | 96 |
| | Summary of results and Conclusions | 99 |
| CHAPTER 5 | Suppression of charge ordering by Ru substitution in LiMn_2O_4 | 102 |
| 5.1 | Nature of Charge ordering in LiMn_2O_4 | 103 |
| 5.2 | Motivation for the substitution of Ru for Mn in LiMn_2O_4 | 105 |
| 5.3 | Synthesis, characterization and four-probe resistivity measurements of $\text{LiMn}_{2-x}\text{Ru}_x\text{O}_4$ ($x = 0.025, 0.05, 0.075, 0.1, 0.15, 0.2$) | 106 |
| 5.3.1 | Synthesis of pristine and Ru substituted LiMn_2O_4 | 106 |
| 5.3.2 | Characterization of pristine and Ru substituted LiMn_2O_4 | 107 |
| 5.3.3 | Four probe Electrical resistance studies on pristine and Ru substituted LiMn_2O_4 | 111 |
| 5.3.3.1 | Measurement of resistance at low temperatures using a dip-stick apparatus | 111 |
| 5.3.3.2 | Results of the resistance studies | 113 |
| 5.4 | Low Temperature synchrotron powder XRD measurements on $\text{LiMn}_{2-x}\text{Ru}_x\text{O}_4$ | 117 |

| | | |
|------------------|---------------------------------------------------------------------------------------------------------------------------|------------|
| 5.4.1 | Details of the ADXRD Beam line BL-12 at INDUS-2 [18-19] | 118 |
| 5.4.2 | LTXRD attachment at BL-12 beam line in INDUS-2 | 118 |
| 5.4.3 | Result of the Ambient temperature powder XRD | 120 |
| 5.4.4 | Results of the LTXRD measurements | 121 |
| 5.4.5 | Phase diagram for $\text{LiMn}_{2-x}\text{Ru}_x\text{O}_4$ | 128 |
| | Summary and conclusions | 129 |
| CHAPTER 6 | Summary of the results and scope for future work | 133 |
| 6.1 | Structural transition under high temperature and high pressure in AlV_2O_4 | 133 |
| 6.1.1 | Rhombohedral (charge ordered) to cubic (charge frustrated) transition on application of temperature | 133 |
| 6.1.2 | Observation of pressure induced frustration on charge state | 134 |
| 6.2 | Charge state of vanadium in the charge ordered rhombohedral AlV_2O_4 | 135 |
| 6.2.1 | Charge state of vanadium in the charge ordered phase examined using electron energy loss spectroscopy | 135 |
| 6.2.2 | ab-initio band structure calculation on the rhombohedral (charge ordered) and cubic (frustrated) AlV_2O_4 | 135 |
| 6.3 | Structural transition on Ru substitution in LiMn_2O_4 | 136 |
| 6.3.1 | Tracing the charge order transition using four probe | 136 |
| 6.3.2 | The competing role of Ru and temperature in the charge ordering of LiMn_2O_4 | 137 |
| 6.4 | Further studies on the charge ordering in spinel system | 137 |
| | List of Publications | 140 |

| FIGURE CAPTIONS | Page No. |
|---------------------------------------------------------------------------------------------------------------------------------------------------------------------------------------------------------------------------------------------------------------------------------------------------------------------------|-----------------|
| Figure 1.1 Pair wise anti aligning interaction on a (a) triangular arrangement and (b) Tetrahedron arrangement ; Two dimensional lattices that sustain frustration (c) triangular lattice and (d) kagome` lattice. | 3 |
| Figure 1.2 Crystal structure of Hexagonal Ice | 5 |
| Figure 1.3 Possible configurations with two-in and two-out criterion | 7 |
| Figure 1.4 The pyrochlore sub-lattice in spinel | 9 |
| Figure 1.5 Structural model for Fe ₃ O ₄ proposed by Verwey | 11 |
| Figure 1.6 Columnar charge ordering in LiMn ₂ O ₄ –Projection along [001] Green-Li; Blue- Mn ³⁺ ; Magenta- Mn ⁴⁺ ; Oxygen atoms are removed for clarity | 13 |
| Figure 1.7 Formation of octamers of Ir ³⁺ (red) and Ir ⁴⁺ (blue) in CuIr ₂ S ₄ when viewed in the [111] cubic direction [31] | 14 |
| Figure 1.8 3:1 ordering of vanadium ions in AlV ₂ O ₄ | 15 |
| Figure 1.9 Structure of rhombohedral AlV ₂ O ₄ in the hexagonal setting. V1 atoms are represented by red, V2 atoms by pink and V3 by dark brown octahedra, aluminum atoms are surrounded by light blue tetrahedron and oxygen atoms are in green. Notice the presence of vanadium heptamers. | 17 |
| Figure 1.10 Structure of LiRh ₂ O ₄ in the cubic phase | 18 |
| Figure 1.11 The five spinel systems that exhibit charge frustration in the cubic structure Fd-3m. All of them relieve the frustration through structural transition by forming unique clustering brought about by the participation of orbitals | 21 |
| Figure 2.1 The STOE $\theta - \theta$ diffractometer operating in the Bragg- Brentano geometry | 29 |
| Figure 2.2 Schematic of a diffractometer in the Bragg-Brentano Geometry | 30 |
| Figure 2.3 Calibration of the diffractometer - Data presented is for Standard Si powder | 32 |
| Figure 2.4 High Temperature attachment to the powder diffractometer. The Ta sample holder, W-Re thermocouple and the Be window are | 33 |

marked for ease of identification.

- Figure 2.5** Formation of AlV_2O_4 ; during the first heat treatment (red), un- 35
reacted raw materials are seen. A subsequent heat treatment
results in partial formation of AlV_2O_4 (black).
- Figure 2.6** Formation of AlV_2O_4 ; (a) partially reacted raw materials; (b) 36
formation of AlV_2O_4 with Al_2O_3 impurity phase; (c) persistent
presence of Al_2O_3 along with AlV_2O_4 ; (d) dissociation of AlV_2O_4
as seen from the emergence of V_2O_3 peaks.
- Figure 2.7:** Formation of AlV_2O_4 ; (a) Formation of AlV_2O_4 at the synthesis 37
step with some amount of Al_2O_3 (b) Retention of AlV_2O_4 with
 Al_2O_3 impurity phase; (c) result of second heat treatment showing
about 6% of Al_2O_3 .
- Figure 2.8** The R-3m structural model with 3:1 ordering of Vanadium ions. Al 38
and O ions are hidden for clarity. V1 ions are shown in red and V2
ions are shown in green.
- Figure 2.9** The Heptamer structural model; The loner V1 ions are in red. 39
Within the heptamer molecule, V2 ions are shown in pink and V3
ions are in green. Al and O are hidden for clarity.
- Figure 2.10** Powder diffraction pattern of AlV_2O_4 from angle 2θ ranging from 40
 16° to 32° . The diffraction peaks in red correspond to the 3:1
model, in blue correspond to the Heptamer model and pink
corresponds to the present work.
- Figure 2.11** Powder diffraction pattern of AlV_2O_4 indexed as per the heptamer 41
structural model
- Figure 2.12** Typical electron diffraction pattern of AlV_2O_4 showing super 42
lattice spots
- Figure 2.13** Rietveld refinement of the ambient pressure, room temperature x- 44
ray diffraction data for AlV_2O_4 and the small impurity phase
 Al_2O_3 (lower calculated pattern). Points represent the
experimental data, the continuous line represents the fitted data
and the curve shown at the bottom is the difference plot.
- Figure 2.14** High temperature powder diffraction of AlV_2O_4 . Beyond 440°C 46
the $(0\ 1\ 8)_R$ and the $(1\ 1\ 0)_R$ reflections (around 30° two theta)
merge to $(2\ 2\ 0)_C$ and also the $(0\ 2\ 16)_R$ and the $(2\ 2\ 0)_R$ peaks
(around 64° two theta) merge to $(4\ 4\ 0)_C$ - explained in the text.
- Figure 2.15** Variation of the d-spacing corresponding to the $(0\ 2\ 16)$ plane and 48

- (220) plane as a function of temperature
- Figure 3.1** Diamond Anvil Cell assembly. Arrow mark indicates the location of the diamond. The culet size is 300 micron. 54
- Figure 3.2** A portion of the powder diffraction data as a function of pressure for AlV_2O_4 . For pressures beyond 22 GPa, AlV_2O_4 shows the charge frustrated cubic phase. Note that the charge disordered phase is retained even after pressure release. Al_2O_3 is denoted by asterisks. 56
- Figure 3.3** Rietveld refinement of the ambient temperature x-ray diffraction data for AlV_2O_4 at 3.9 GPa. Points represent the experimental data, the continuous line (blue) represents the fitted data and the curve shown at the bottom (pink) is the difference plot. 57
- Figure 3.4** Variation of lattice parameters of the rhombohedral phase (a_R and $c_R/3$) and cubic phase (a_c). Inset shows the relative variation of the rhombohedral lattice parameters as a function of pressure for AlV_2O_4 . 60
- Figure 3.5** Powder diffraction patterns of AlV_2O_4 obtained under hydrostatic pressure. The applied pressure in GPa is mentioned on each pattern. 62
- Figure 3.6** Observed variation of volume/formula unit as a function of pressure in the charge ordered rhombohedra and frustrated cubic phases 64
- Figure 3.7** Relative variation of rhombohedral lattice parameter as a function of hydrostatic pressure for AlV_2O_4 65
- Figure 3.8** Equation of state of AlV_2O_4 obtained by fitting the P-V data to third order Birch-Murnaghan equation 66
- Figure 3.9** Structure of AlV_2O_4 in the relevant directions; (a) Rhombohedral phase in the (0-10) projection with three different vanadium ions; (b) Cubic phase in (0-11) projection. 68
- Figure 4.1** Structure of rhombohedral AlV_2O_4 in the hexagonal setting. V1 atoms are represented by red, V2 atoms by pink and V3 by dark brown octahedra, aluminum atoms are surrounded by light blue tetrahedral and oxygen atoms are shown in green. Notice the presence of vanadium heptamers. 73
- Figure 4.2** Schematic of energy level structure of transition metal in the octahedral co-ordination of oxygen 75

| | | |
|--------------------|-----------------------------------------------------------------------------------------------------------------------------------------------------------------------------------------------------------------------------------------------------------------------------------------------------------------------------------------------------------------------------------------------------------------------------------------------------------------------------------------------------|-------|
| Figure 4.3 | Schematic of the EELS attachment in TEM | 76 |
| Figure 4.4 | Typical EELS spectrum of commercial V ₂ O ₅ . The layers represent different energy loss regions depicting different processes as explained in the text. | 77 |
| Figure 4.5. | Electron Energy Loss spectrum of AlV ₂ O ₄ Note: Oxygen K-edge starts at 538 eV immediately after the L ₂ -edge of Vanadium at 527 eV | 79 |
| Figure 4.6 | EELS spectra for V ₂ O ₅ , VO ₂ , V ₂ O ₃ and AlV ₂ O ₄ in the energy range corresponding to the L _{2,3} edge and O-K edges | 81 |
| Figure 4.7 | L _{3,2} ratio versus vanadium oxidation state | 82 |
| Figure 4.8 | Vanadium L ₃ edge onset versus oxidation state. Squares represent the experimentally measured chemical shift. Solid line shows the fit to $E = a_1V_{ox} + a_2$. | 84 |
| Figure 4.9 | Rhombohedral structural model of AlV ₂ O ₄ showing the heptamer formed by V2 sandwiched between two V3 trimers and the lone V1. Green spheres denote oxygen and light blue denotes aluminum. | 88 |
| Figure 4.10 | Spin polarized band structure of: (a) rhombohedral and (b) cubic AlV ₂ O ₄ . The high symmetry coordinates are also marked in the rhombohedral case in order to conform to the labeling scheme of Cai <i>et al</i> | 90 |
| Figure 4.11 | Calculated total and partial density of states for rhombohedral and cubic AlV ₂ O ₄ . (a) Shows the total and atom decomposed DOS for rhombohedral phase. (b) All the DOS for V atoms is contributed by the V 3d orbitals, as no difference between the total and d orbital contribution can be seen. (c) Total and atom decomposed DOS for the cubic phase. It shows a half-metallic behavior as the spin-up channel is metallic, while the spin-down channel is insulating. | 92-93 |
| Figure 4.12 | Total energy as a function of Volume / Formula unit for AlV ₂ O ₄ . Filled triangles and filled circles represent the experimentally observed volume/FU; open triangle and circles represent relaxed volumes/FU for the cubic and rhombohedral phase. Solid line indicates fit to Birch-Murnaghan equation of state. | 97 |
| Figure 4.13 | Structure of AlV ₂ O ₄ in the relevant directions; (a) Rhombohedral phase in the 0-10 projection with three different vanadium ions; | 98 |

| | | |
|--------------------|------------------------------------------------------------------------------------------------------------------------------------------------------------------------------------------------------------------------------------------|---------|
| | (b) Cubic phase in 0-11 projection | |
| Figure 5.1 | Powder diffraction pattern of pristine LiMn_2O_4 . Blue lines at the bottom correspond to the best quality reference data (ICDD card No. 35-0782) | 108 |
| Figure 5.2 | Powder diffraction pattern of pristine and Ru substituted LiMn_2O_4 | 109 |
| Figure 5.3 | Variation of lattice parameter in $\text{LiMn}_{2-x}\text{Ru}_x\text{O}_4$ Vs Ru concentration | 110 |
| Figure 5.4 | Typical SEM picture of (a) pristine LiMn_2O_4 (b) $x=0.075$ sample showing triangular morphology characteristic of the cubic spinel system | 111 |
| Figure 5.5 | Schematic of the Low Temperature resistivity dip stick | 113 |
| Figure 5.6 | Variation of resistance with temperature. Ru concentration is mentioned in the legend | 114-115 |
| Figure 5.7 | Variation of resistivity as a function of Ru concentration in $\text{LiMn}_{2-x}\text{Ru}_x\text{O}_4$ | 117 |
| Figure 5.8 | The LTXRD attachment at BL-12 in INDUS-2. The Be dome for holding the sample under vacuum at low temperature and the MAR detector are indicated by the arrows. The continuous flow cryostat resting on the frame is seen above the dome. | 119 |
| Figure 5.9 | Powder diffraction pattern of the pristine LiMn_2O_4 at ambient temperature | 120 |
| Figure 5.10 | LTXRD pattern of LiMn_2O_4 showing the splitting of the Cubic (511) reflection | 121 |
| Figure 5.11 | LTXRD pattern of $\text{LiMn}_{1.975}\text{Ru}_{0.025}\text{O}_4$ showing the splitting of the Cubic (511) reflection. Data collection during cooling. | 122 |
| Figure 5.12 | LTXRD pattern of $\text{LiMn}_{1.975}\text{Ru}_{0.025}\text{O}_4$ showing the splitting of the Cubic (511) reflection; Data collection during warming. | 122 |
| Figure 5.13 | Variation of lattice parameter with temperature in $\text{LiMn}_{1.975}\text{Ru}_{0.025}\text{O}_4$. The cubic to the orthorhombic structural transition occurs between 270 and 275 K. | 123 |
| Figure 5.14 | LTXRD pattern of $\text{LiMn}_{1.96}\text{Ru}_{0.04}\text{O}_4$ showing the splitting of the Cubic (511) reflection; Data collection during cooling and warming. | 124 |
| Figure 5.15 | LTXRD pattern of $\text{LiMn}_{1.95}\text{Ru}_{0.05}\text{O}_4$ showing the splitting of the Cubic (511) reflection; Data collection during Cooling and | 125 |

warming.

Figure 5.16 LTXRD pattern of $\text{LiMn}_{1.25}\text{Ru}_{0.075}\text{O}_4$ showing the splitting of the Cubic (511) reflection; Data collection during Cooling and warming. 126

Figure 5.17 LTXRD pattern of $\text{LiMn}_{1.9}\text{Ru}_{0.1}\text{O}_4$ showing the splitting of the Cubic (511) reflection; Data collection during Cooling and warming. 127

Figure 5.18 Phase diagram for $\text{LiMn}_{2-x}\text{Ru}_x\text{O}_4$ showing the cubic and orthorhombic phases 128

| LIST OF TABLES | | Page No. |
|-----------------------|----------------------------------------------------------------------------------------------------------------------------------------------------------------------------------------------------------------------------------------------------------------------------------------------------------------------------------------------------------------------------------------------------------------------------------------------------------------------------------------------------------------------------------|---------------------|
| Table 2.1 | Structural parameters of AlV_2O_4 at room temperature showing fractional co-ordinates and the isotropic atomic displacement ($U_i/U_e \cdot 100$) \AA^2 from Rietveld refinement of powder diffraction data collected with laboratory Cu-K α x-ray source. The lattice parameters are: $a = b = 5.7613(2)$ \AA and $c = 28.6876(10)$ \AA (hexagonal notation). The cell volume = $824.65(4)$ \AA^3 . The R factor $R_p = 13.5\%$ and the reduced $\chi^2 = 2.442$. | 45 |
| Table 3.1 | Structural parameters of AlV_2O_4 at room temperature and 3.9 GPa showing fractional co-ordinates and the isotropic atomic displacement ($U_i/U_e \cdot 100$) \AA^2 from Rietveld refinement of powder diffraction data collected with $\lambda = 0.4959 \text{\AA}$. | 58 |
| Table 3.2 | Variation of V-V distances in the kagome plane (V3-V3) and across the kagome` and triangular planes (V1-V3 and V2-V3) obtained from refining of the non-hydrostatic pressure data. | 59 |
| Table 4.1 | O-K edge for V_2O_5 , VO_2 , V_2O_3 and AlV_2O_4 from this work and also from [3] | 85 |
| Table 4.2 | Summary of structural information on AlV_2O_4 obtained from Rietveld refinement of powder data and DFT computations from the present work and data drawn from references [1] and [2] | 95 |
| Table 5.1 | Ionic Radii and electron count for Mn and Ru | 107 |

CHAPTER 1

Geometrically frustrated spinel systems and ordering of charges –A brief review

Electron correlation in condensed matter always seems to throw up a plethora of novel, exotic and complex phenomena that routinely destabilize every attempt to formulate or formalize understanding. In the last few decades several challenges are posed by the high temperature superconductors, colossal magneto resistance materials, spin glasses, frustrated systems and so on. Experimental and theoretical tools have been stretched to their limits to comprehend the complexities, but the horizon of convergence appears to recede farther and farther. Amongst the complex, correlated condensed matter systems, ‘frustrated systems’ are a class in itself and they exhibit novel ground states like spin liquids, spin ice and valence bond solids. The spinel compounds amongst these are unique in exhibiting such unconventional ground states. Ordering of the charge degree of freedom in a spinel system is a rare and contested phenomenon. Very few spinel compounds have shown coupling of the charge degree of freedom with the lattice as against a number of those that have shown frustration and ordering of spin degrees of freedom. Charge ordering out of a frustrated lattice has been observed in the spinel compounds like Fe_3O_4 [1], AlV_2O_4 [2], LiMn_2O_4 [3], LiRh_2O_4 and CuIr_2S_4 [4]. LiV_2O_4 is another unique spinel compound where charge and spin remain frustrated down to very low temperatures ($<1\text{K}$) and charge ordering occurs under pressure [5]. Interestingly this is the only compound that shows heavy fermion behaviour in transition metal

compounds. Another spinel oxide of relative similarity namely, LiTi_2O_4 is a type II superconductor with a T_c of about 13K [6]. Apart from the coupling of charge and spin degrees with the lattice, coupling of orbital degrees with lattice is observed in some spinel compounds. For instance MgTi_2O_4 shows orbital ordering by the formation of dimers [7]. The formation of ‘multimers’, like dimers, trimers, heptamers and octomers is believed to be the path through which the system moves from a charge frustrated state to a charge ordered state. Experimental evidence through electron diffraction and x-ray diffraction support the formation of such multimers below the charge ordering transition temperature. Yet direct observation of charge ordering is still elusive. It is also to be noticed that among the few known materials mentioned above, no unique mechanism has emerged, to explain the observed phenomenon of order from frustration. A lot more experimental and theoretical efforts are called for.

This introductory chapter is divided into various sections to contextualize and motivate the present thesis. Section 1 reviews the concept of geometrical frustration. Section 2 explains frustration in the context of water ice. Section 3 describes the cation ordering in the pyrochlore lattice. Section 4 and 5 present a short review and summary of the spinel oxides exhibiting charge frustration. Section 6 summarizes the motivation and organization of this thesis.

1.1 The concept of Geometrical frustration – Historical development

Whenever a conflict arises between some fundamental interaction and the underlying lattice geometry, a geometrical frustration is said to result. The effect of such a geometrical frustration is the finite entropy at zero Kelvin indicating existence of a degenerate ground state. The recognition of the existence of such a geometrical

frustration dates back to 1936 when Giaque and Stout [8] measured specific heat on hexagonal water-ice and showed finite entropy (0.8 cal/deg/mole) at zero Kelvin which was explained by Linus Pauling [9] by considering the configurational entropy using the Bernal-Fowler [10] ice-rules. In general frustration can be of two types. Geometrical frustration is one of them and the other is frustration in accommodating two components with minimum energy configuration irrespective of the underlying geometry of the space. Spin glasses [11-12] form good example of the latter.

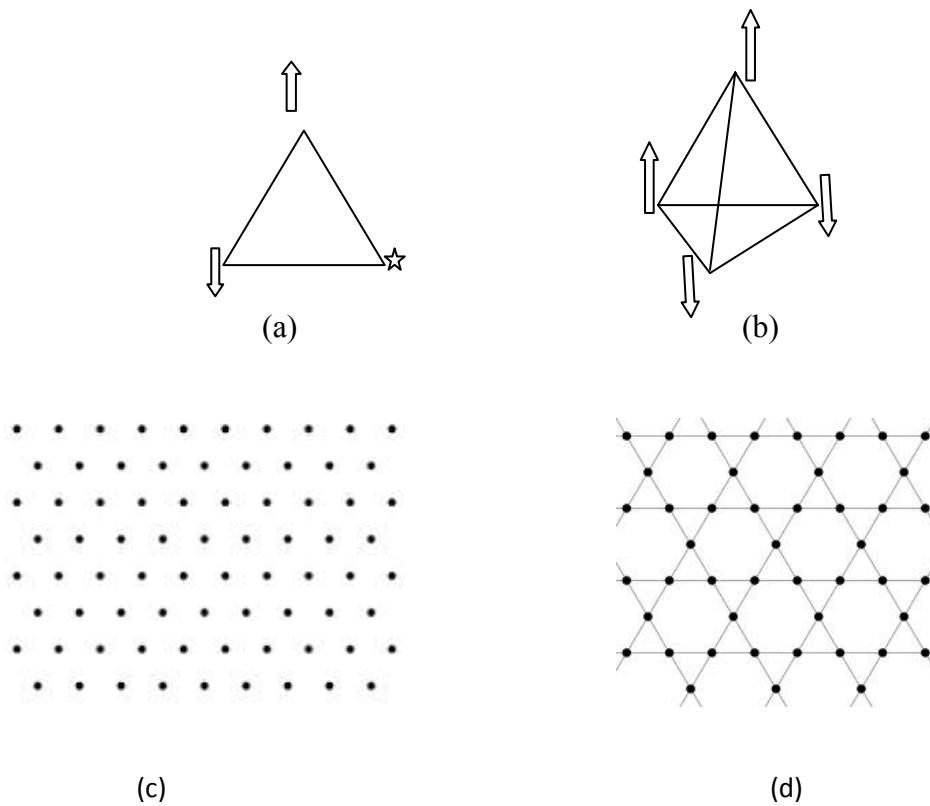


Figure 1.1 Pair wise anti aligning interaction on a (a) triangular arrangement and (b) Tetrahedron arrangement ; Two dimensional lattices that sustain frustration (c) triangular lattice and (d) kagome` lattice.

A typical example of geometrical frustration is anti-ferromagnetic interaction of Ising spins on a triangular lattice. In such a lattice the pair-wise anti-aligning of spins is incompatible with the underlying triangular lattice and the ground state becomes de-

generate. The number of possible ground state configurations increase as one moves from a triangular lattice to a pyrochlore lattice. There are a few lattices which have inherent tendencies for geometrical frustrations to occur. They are the triangular lattice and the kagome' lattice in two dimensions and the pyrochlore lattice in three dimensions. To understand the existence of degenerate ground states accompanying geometric frustration, consider the case of pair-wise anti aligning of spins on a triangle as shown in Figure 1.1 (a). On a triangle after positioning the two anti-aligned spins, the third one can be placed either up or down. So the ground state can keep flipping between the two possibilities without an extra cost in energy. A similar situation exists on a tetrahedron as shown in Figure 1.1 (b). Once again if pair-wise anti aligning of spins has to be realized on this geometry, it shows incompatibility and hence frustration. But a configuration with two spins up and two spins down can still be attempted. There are eight such possibilities which are energetically favorable, thereby resulting in 8-fold degenerate ground state.

The pyrochlore lattice with parallel Ising spins is also frustrated and is similar to the 'water ice'. Discovery of finite residual entropy in $\text{Ho}_2\text{Ti}_2\text{O}_7$ [13] demonstrated the first experimental observation of 'spin ice' on a pyrochlore lattice. In general minimization of the number of underlying constraint maximizes the ground state degeneracy of the interacting species. In all of these lattices severe frustration results, for example, when pair-wise anti parallel spin interaction have to be incorporated. A variety of experimental and theoretical works have been carried out in the case of frustrated magnetism [14]. A similar scenario as in the case of 'water ice' is anticipated if multivalent cations occupy the pyrochlore sub-lattices present in cubic spinel systems. In comparison with the frustrated magnetic systems, very few compounds have shown

frustration of charges. Since, it all started with ‘water ice’, it is essential to understand the nature of geometrical frustration in hexagonal ice.

1.2 Geometric frustration in ‘water ice’

Figure 1.2 shows the crystal structure of Ice Ih (Space Group P63/mmc (194)); Symmetry: D_{6h} [15]. In a hexagonal ice crystal each H_2O molecule has four nearest neighbors arranged near the vertices of a regular tetrahedron centered about the molecule of interest.

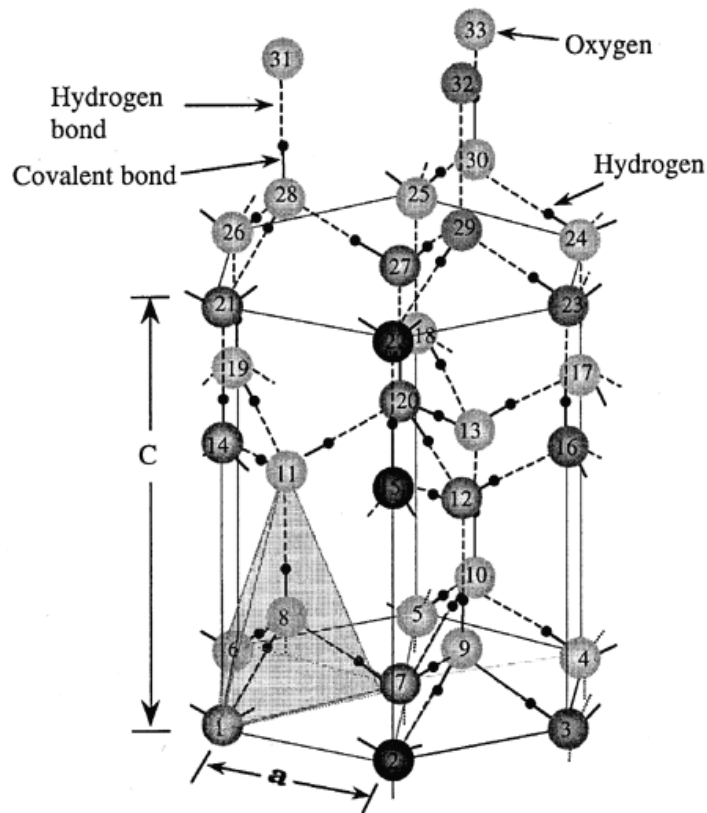


Figure 1.2 *Crystal structure of Hexagonal Ice*

The oxygen atom of each molecule is strongly covalently bonded to two hydrogen atoms, while the molecules are weakly hydrogen bonded to each other. When projected

onto the plane perpendicular to the c-axis, the molecular stacking sequence is . . . ABBAABBA ... The lattice parameters are: $a = 4.523 \text{ \AA}$ and $c = 7.367 \text{ \AA}$. The c/a ratio (1.628) is very close to the ideal ratio (1.633) and is independent of temperature. The ice Ih unit cell is relatively open (packing factor less than 0.34), and this accounts for ordinary ice being less dense than water. In building this structure, Bernal-Fowler proposed a rule that must be followed for the stability of the structure for the ideal crystal based on the assumptions that:

Each oxygen atom is bonded to two hydrogen atoms at a distance of 0.95 \AA to form a water molecule.

Each molecule is orientated so that its two hydrogen atoms face two, of the four, neighboring oxygen atoms that surround in tetrahedral coordination;

1. The orientation of adjacent molecules is such that only one hydrogen atom lies between each pair of oxygen atoms;
2. Ice (Ih) can exist in any of a large number of configurations, each corresponding to a certain distribution of hydrogen atoms with respect to oxygen atoms.

Based on these assumptions, the Bernal-Fowler rule states that “two protons stay near each of the oxygen and one proton must be on each O-O bond”. Each of the oxygen is at a distance of 2.76 \AA and the retained O-H bond distance is 0.95 \AA . Each oxygen must have two hydrogen at 0.95 \AA and two hydrogen at 1.81 \AA . The structural constraint demanding tetrahedral positioning of oxygen coupled with the requirement of molecular integrity of H_2O leads to frustration in proton-proton (hydrogen ion) interaction. In

general the protons would like to be far apart from the considerations of electrostatic interaction.

The possible configurations of organizing the frustrated protons on a tetrahedron can be enumerated as follows. Representing the protons by arrows as shown in figure 1.3, with an arrow pointing in implying 'near' and an arrow pointing out implying 'far', it can be seen that in general there are sixteen possibilities. This reduces to six when the 'ice rule', (namely, two-near and two-far) is applied. These six configurations, with two-in and two-out, are presented within the box.

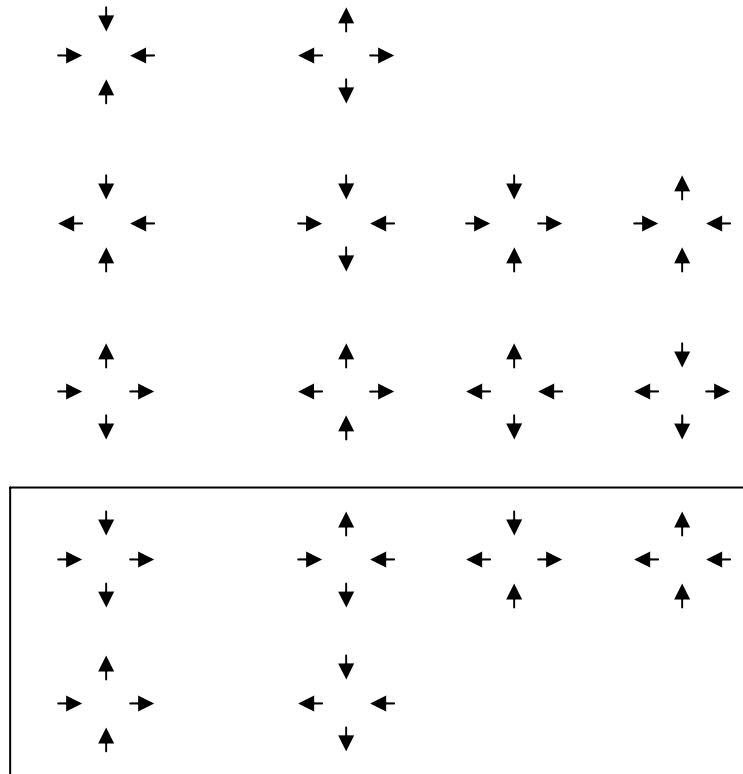


Figure 1.3 Possible configurations with two-in and two-out criterion.

It must also be considered that, of the four hydrogen bonds (between the oxygen ions) in which one water molecule participate, two are occupied by its hydrogen atoms and two are unoccupied. The chance that a given direction is available to a hydrogen atom is therefore 1/2, and as there are two hydrogen atoms to be placed, the probability that this can be done is $1/2 \cdot 1/2 = 1/4$. Thus if there are a total of N molecules, the total number of configurations is then $W = (6/4)^N = (3/2)^N$ contributing to finite entropy.

$$S_0 = k_B \ln(\Omega) = Nk_B \ln\left(\frac{3}{2}\right) = 0.81 \text{ Cal/deg/mol}$$

This agrees well with the experimentally measured entropy value [1]. Thus frustration leads to ground state degeneracy.

1.3 Cation ordering in the pyrochlore spinel sub-lattice and the Verwey transition

Analysis of the ordering of the ions in the hexagonal ice demonstrates that whenever pyrochlore lattice is to be occupied by species with a specific pair-wise interaction a degenerate ground state can be anticipated. The recognition of frustration and finite entropy in water ice has resulted in modeling spins on triangular and pyrochlore lattices. Earliest calculations by Wannier [16] consider the case of Ising spins on triangular lattice and show that the ground state of the model is macroscopically degenerate while occupying such a tetrahedron. Subsequent calculations by Anderson consider ordering of cations on the octahedral sites of an inverse spinel system and spins in a normal spinel system. A formula unit in the spinel system is represented as AB_2O_4 , where, in the case of normal spinel the 8A ions form tetrahedron and the 16 B-ions form octahedral lattice. In the case of inverse spinel, 8-B ions form the tetrahedron and (8A+8B) ions form the octahedral. Focusing attention on the octahedral site, it is easy to

anticipate that there can be cation disorder due to the multiple possibilities of occupation of the octahedral sites by the A and B ions. The lattice formed by this octahedral site is like that of a pyrochlore *i.e.* corner sharing tetrahedron. Figure 1.4 shown here depicts the pyrochlore lattice. Each of the black dots (lattice points) is decorated by a basis of octahedral unit with a cation at the center of the octahedra and oxygen ions at the vertices.

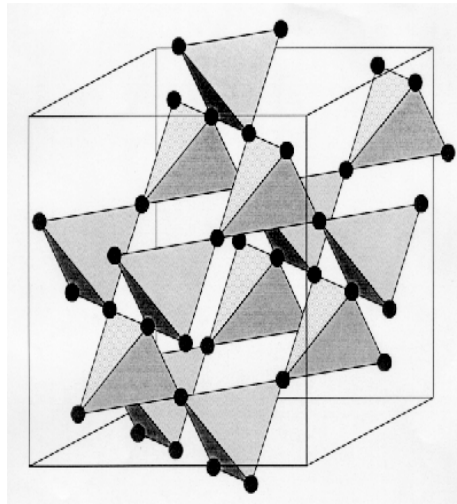


Figure 1.4 *The pyrochlore sub-lattice in spinel*

Such a corner sharing tetrahedral lattice possesses an underlying diamond cubic symmetry as against the hexagonal symmetry observed in the case of tetrahedrons present in the water ice. Anderson imposed a criterion [17] that, if the A and B ions are represented by '+' and '-', then according to this criterion the '+' and '-' arrange themselves so that there is maximal number of '+;- 'pairs. This implies that in each tetrahedron 2 '+' and 2 '-' are placed. At this stage the similarity between the present case and the water ice emerges clearly and there are as earlier six possible ways of

arranging the two '+' and two '-' on any one tetrahedron. It can be observed from the figure that there are two sets of tetrahedral (each set inverted with respect to the other) and that the tetrahedron of one set touches only the tetrahedron of the other. If there are N lattice points there are N/4 tetrahedra on one set and similarly N/4 on the other. Considering the probability that any one tetrahedra has the correct configuration is 3/8, the number of possible correct configurations (two '+' and two '-') works out to be:

$$W = \left(\frac{3}{8}\right)^{(N/4)} \cdot 6^{N/4}$$

Thus the cations on the pyrochlore lattice can transform from an infinite random occupation possibilities to a finite number of possibilities and hence the Verwey transition indicating choice of one such possibility.

1.4 A short review of the spinel oxides exhibiting charge ordering from frustration

1.4.1 Recent results of structural analysis of Fe₃O₄ below Verwey transition

Verwey showed that in Fe₃O₄ there exists an electrical and magnetic transition, at around 125 K. He proposed that Fe³⁺ (3d⁵_{HS}) and the Fe²⁺ (3d⁶_{HS}) order periodically on the B sub-lattice causing such a transition. Ever since the proposal, this structural model claiming ordering of Fe has been highly debated. Analysis of single crystal neutron diffraction data [18] showed that no charge ordered pattern emerged. This claim too was disputed because of the twinning of the crystal domains that comes in the way of resolving the single crystal data. Later another analysis based on combined refining of neutron and X-ray diffraction data [19], claimed a weak charge modulation breaking up

the structure into 1-d stripes. This model was again contested and lost ground based on the results of resonant scattering experiments [20].

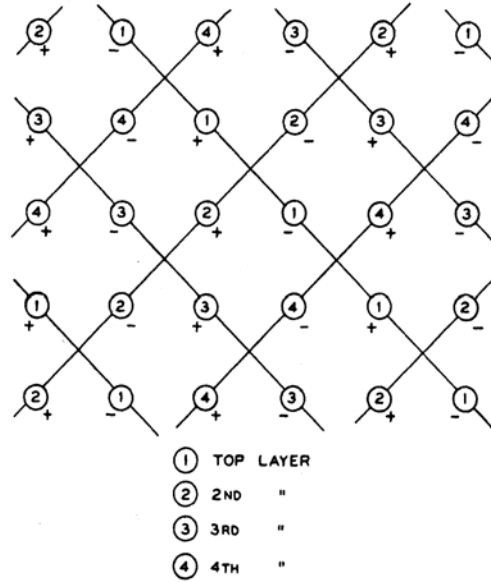


Figure 1.5 Structural model for Fe_3O_4 proposed by Verwey

Very recent high energy X-ray diffraction experiments [21] from an almost single domain (40 μ m) grain claim that Verwey's hypothesis of 1:1 order of Fe^{2+} and Fe^{3+} is correct to a first approximation. The low temperature structure condenses to Cc super structure with 16 inequivalent octahedral B-sites. However the absence of bimodal distribution of formal Fe charge, considerations of Fe-O bond distances, associating the anomalously short $Fe^{2+}-Fe^{3+}$ distance with delocalization of a single charge over one Fe^{2+} and two adjacent Fe^{3+} , this study predicts formation of 'trimerons' as the quasi particles of the system. Hence the current picture on Fe_3O_4 is that the ordered Cc structure is a super cell of the parent cell with $\sqrt{2}a \times \sqrt{2}a \times 2a$ – New order parameter $-t_{2g}$ occupancies. The Verwey model is replaced by an orbital ordering picture involving charge disproportionation. In the recent times, it is recognized that Fe_3O_4 is a multiferroic

[22], apart from being ferrimagnetic ($T_N=851\text{K}$), below the Verwey transition temperature. Thus the spinel Fe_3O_4 is still being studied, even 75 years after the discovery of Verwey transition and it appears that every attempt to understand this system throws up more questions than answers.

1.4.2 Columnar ordering of charges in LiMn_2O_4

LiMn_2O_4 is an important battery electrode material and is synthesized using a variety of techniques and studied extensively. It goes through a structural transition at around 290 K [23] which in fact comes in the way of tapping the full potential of this battery material. Initially this structural transition was attributed to the Jahn-Teller distortion of Mn^{3+} ions and efforts to increase the oxidation state of Mn by incorporating Li for Mn were carried out [24-25].

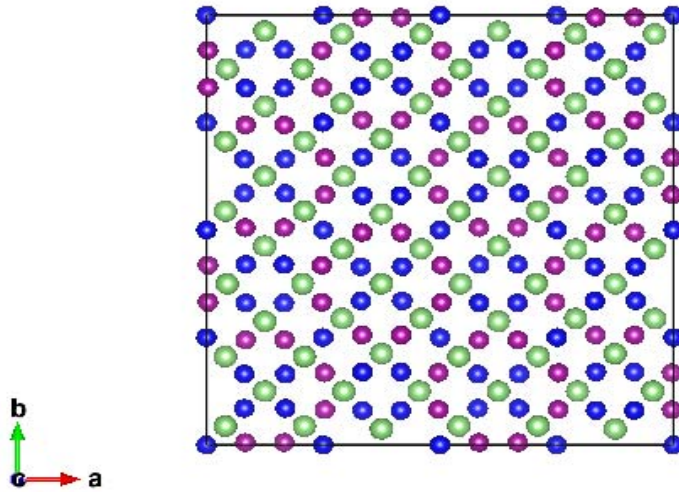


Figure 1.6 *Columnar charge ordering in LiMn_2O_4 –Projection along $[001]$;Green-Li; Blue- Mn^{3+} ; Magenta- Mn^{4+} ; Oxygen atoms are removed for clarity.*

Later detailed analysis of neutron diffraction data [26] showed that the LiMn_2O_4 undergoes a structural phase transition from the high temperature cubic structure to an orthorhombic structure with the formation of $3a \times 3a \times a$ superstructure of the high temperature cubic cell. The most significant factor that characterizes the charge ordered state is the Mn-O bond distance. While in the charge frustrated cubic ($Fd-3m$) spinel phase there is a unique Mn-O distance of $1.9609(3) \text{ \AA}$, the charge ordered orthorhombic ($Fddd$) structure with five different Mn sites as in figure 1.6, shows two different Mn-O distances; two of the Mn sites show an Mn-O distance of 1.91 \AA indicating the existence of Mn^{4+} and the other three of them show an Mn-O of 2.01 \AA that correspond to Mn^{3+} . EXAFS measurements [27] carried out as a function of temperature confirms the existence of two different Mn-O distances.

This study also brings forth the presence of a large static lattice disorder due to the slightly varying Mn-O distances around each Mn ion. The charge ordering occurs as a columnar ordering of Mn^{3+} and Mn^{4+} , in such a way that two kinds of columns of Mn^{3+} one including a Li at the center and the other without a Li are surrounded by octagonal cylinders of Mn^{4+} . Magnetic ordering in this material is still unsettled, since there is wide difference in the results of neutron diffraction experiments. Low temperature neutron diffraction [28] study shows anti ferromagnetic ordering and hence complete removal of spin frustration in this system. Yet another study shows coexistence between anti-ferromagnetic long range ordering and diffuse scattering [29]. One more study claims complete absence of magnetic ordering [30]. Susceptibility measurements have shown an abrupt jump at the transition temperature and the Curie constant and Weiss temperature are estimated to be $C=4.86 (15) \text{ emu K mol}^{-1}$ and $\theta = -300 (20) \text{ K}$, respectively [21].

Around 65 K there is a splitting between the field cooled (FC) and zero field cooled (ZFC) susceptibility. On further cooling, the FC susceptibility reaches a maximum at 45 K. These observations imply AFM fluctuations in the material and probably an ordering of spins at 45 K. Electrical resistivity shows an upturn at the transition, characteristic of the charge ordering transition going from semi-conducting to localized behavior [29].

1.4.3 Octamer formation in CuIr_2S_4

CuIr_2S_4 is another spinel system which has shown charge ordering from frustration. In this system Cu assumes a valency of 1^+ and hence Ir has to exist as a multivalent ion and it assumes $^{+3}$ and $^{+4}$ formal oxidation states.

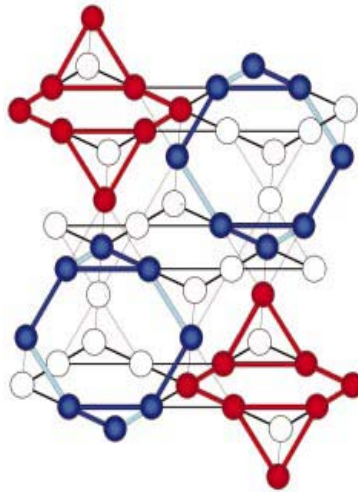


Figure 1.7 *Formation of octamers of Ir^{3+} (red) and Ir^{4+} (blue) in CuIr_2S_4 when viewed in the $[111]$ cubic direction [31]*

It shows metal-insulator transition at 230 K accompanied by a complete loss of magnetic moments [31]. Determination of crystallographic structure below this temperature shows a charge ordered state that is attributed to a unique formation of spin dimers. The charge ordered state described by the triclinic structure is supposed to be made of isomorphous octamers as shown in Figure 1.7, involving isovalent bi-capped hexagonal rings. Spin

dimer formation is strictly expected only in 1-d system due to the coupling of spins to the lattice degree of freedom as in spin Peierls compounds like CuGeO_3 [32]. In the case of CuIr_2S_4 it is the Ir^{4+} with unpaired electrons in the d_{xy} orbitals that show varying Ir-Ir distances within the octamers and thus are supposed to form the spin dimers. Of all the charge ordered spinel compounds CuIr_2S_4 is studied extensively. They have shown that the metal-insulator transition in CuIr_2S_4 is very delicate and is easily destroyed under irradiation with X-rays [33] or , substitution of Ni at A-site or Ti, Rh and Cr at B-site [34] (and references there in) .

1.4.4 Novel heptamer formation in AlV_2O_4

The spinel compound AlV_2O_4 opens up another new way of ordering of charges. Aluminum, a trivalent cation resides on the A site, and vanadium occupies the pyrochlore B-lattice with an average valency of 2.5. Interestingly AlV_2O_4 shows a semiconductor to insulator transition at around 700 K with a slight reduction in magnetization. A structural transition from cubic to rhombohedral (R-3m) has been observed to accompany the resistive transition indicating charge ordering. Thus AlV_2O_4 gives a unique opportunity of probing the charge ordered state at ambient temperatures.

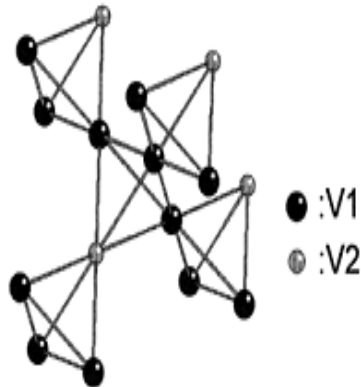


Figure 1.8 *3:1 ordering of vanadium ions in AlV_2O_4*

When charge ordering from frustration was discovered in AlV_2O_4 , [2] to maintain charge neutrality, it was proposed that the vanadium ions with an average valency of 2.5 in the cubic phase splits into V1 ions with valency $2.5-\delta$ and V2 ions with valency $2.5+3\delta$. It was thought that this compound is a good example of ordering of vanadium ions as 3:1 (V1:V2) in every vanadium tetrahedral as shown in Figure 1.8. But subsequent detailed analysis of electron diffraction data indicated super lattice peaks at $(\frac{1}{2} \frac{1}{2} \frac{1}{2})$ kind of positions which required a totally different structural model to explain the observation. Based on the observation of super lattice spots and refinement of synchrotron powder diffraction data, a totally novel ‘heptamer’ clustering of vanadium ions with a left out ‘lone’ vanadium ion has been proposed to model the structure [35]. Vanadium occupies a single site in the frustrated spinel state, but in the charge ordered rhombohedral phase (R-3m), there are three different V sites V1, V2, V3. Based on the V-O bond distances it is assumed that the valence state of V1, V2 and V3 are +3, +2 and +2.5. When viewed from the [1 1 1] direction of the cubic cell, the three vanadium are arranged as layers of V1-V3-V2-V3-V1-V3-V2-V3 ...

This structural model is shown in figure 1.9. The V3 trimers (brown) of adjacent planes along with the V2 (pink) form the heptamer cluster of seven vanadium atoms. The V1 (red) are considered to be loners as they do not bond with the neighbors. The magnetic susceptibility below 600 K could be fitted with a Curie -Weiss term and spin gap term. Existence of Curie-Weiss term till very low temperatures implies suppression of magnetic ordering. In AlV_2O_4 it implies that, though the charges have ordered below 700 K, the spins on vanadium continue to remain frustrated. This work also brings out that substitution of Mg for Al and Cr for V suppress the charge ordering. ^{51}V and ^{27}Al

NMR measurement [36] observes variation of knight shift ^{51}K and ^{27}K as a function of temperature.

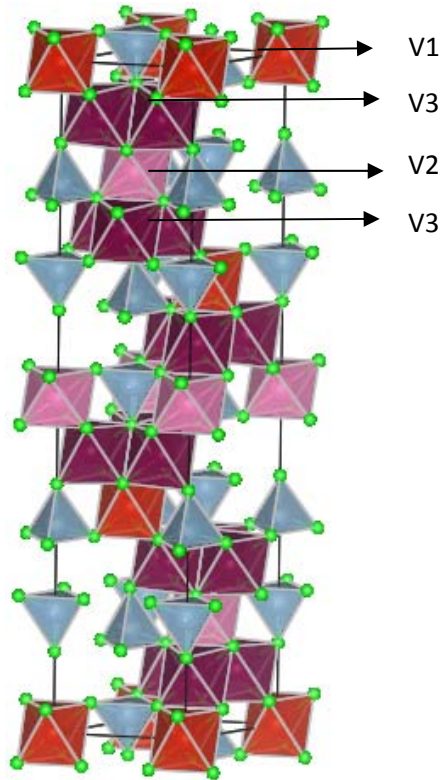


Figure 1.9 Structure of rhombohedral AlV_2O_4 in the hexagonal setting. V1 atoms are represented by red, V2 atoms by pink and V3 by dark brown octahedra, aluminum atoms are surrounded by light blue tetrahedron and oxygen atoms are in green. Notice the presence of vanadium heptamers.

The observed knight shifts could be fitted using the expression for susceptibility suggested in terms of spin gap and Curie–Weiss terms. At the local level it confirms existence of spin singlet behavior of the heptamer clusters and triplet behavior of the lone vanadium V1. Interestingly the hyperfine coupling constant (B) measured from the ratio of the knight shift and the susceptibility works out to be $-82 \pm 8 \text{ kOe} / \mu_{\text{B}}$ which in terms of orbital occupancy translates to a value comparable to VO_2 (one valence electron) and

less than V_2O_3 (two valence electrons). It is to be noted that the nature of charge distribution is still very interpretative in AlV_2O_4 .

Results of the first principles density functional theory computations [37] confirm heptamer clustering within the rhombohedral charge ordered structure. From the V-V distance obtained on the converged structure, it is proposed that the charge distribution on the vanadium ions may be $V1^{2.5-\delta_1}$, $V2^{2.5+\delta_2}$ and $V3^{2.5+(\delta_1-\delta_2)/6}$ with $\delta_1 > \delta_2 > 0$; Electron energy loss spectroscopy measurements on AlV_2O_4 [38] record a unique three peak structure in the O- K edge and an average charge state of 2.5 on the vanadium ions. The origin of the heptamer formation is supposed to emerge from 1-D orbital ($V-d_{xy}$) chains [39]. From these studies it can be concluded that the low temperature charge ordered structure is explained by the heptamer cluster formation of vanadium ions. This kind of cluster formation is unique and it is to be examined how robust is this heptamer cluster in the presence of various parameters. The available results indicate that the cluster formation may be very delicate. It is also observed that charge distribution on the vanadium ions is yet to be established conclusively.

1.4.5 Frustration to order in $LiRh_2O_4$

Very recently another new spinel compound $LiRh_2O_4$ has been synthesized [40] and observed to show a valence bond solid ground state following a band Jahn Teller effect. Rh in the B site has probably 1:1 ratio of Rh^{3+} ($S = 0$, $4d^6$), and Rh^{4+} ($S = 1/2$, $4d^5$). In contrast with the other charge frustrated spinel systems, $LiRh_2O_4$ shows two transitions. Initially on cooling from ambient temperature down to 230 K, the resistivity

remains flat. At 230 K, it appears to show a weak increase till down to 170 K. But at 170 K, the resistivity increases several orders of magnitude.

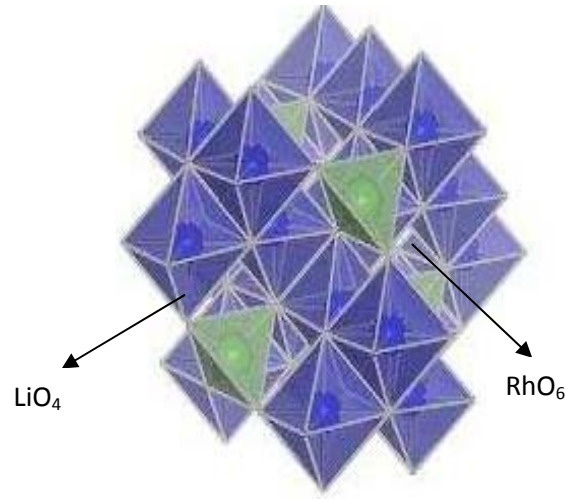


Figure 1.10 Structure of LiRh_2O_4 in the cubic phase [40]

Also the ambient temperature cubic structure transforms to a tetragonal structure ($I 4/a m d$) at 230 K and it further undergoes a transition to orthorhombic structure at 170 K. At present the transition at 230 K is identified as band Jahn–Teller transition and the other one at 170 K is considered to be a charge ordered transition induced by the band Jahn-Teller effect. Magnetic susceptibility shows that the system moves from an orbital disordered paramagnetic metal to orbital ordered paramagnetic metal to a charge and orbital ordered, insulating non magnetic valence bond solid. Specific heat measurements made using DSC indicate a large change in entropy $0.24 \text{ R/mole Rh}^{4+}$ and $0.70 \text{ R/mole Rh}^{4+}$. The density of states near the Fermi surface is predominantly from the transition metal ions and they make a flat band in the case of charge ordered materials. This density of states, couple with the degeneracy in the orbital degree of freedom in the case of

LiRh_2O_4 , resulting in band Jahn-Teller instability. An increased thermo electric power ($80 \mu\text{V/K}$ at 800 K) measured in LiRh_2O_4 is supposed to auger well with this argument. Eventually this band Jahn-Teller instability is supposed to drive the system to a valence bond solid state.

1.5 Short summary of the spinel compounds exhibiting charge order from frustration

To sum up, the five spinel compounds Fe_3O_4 , LiMn_2O_4 , CuIr_2S_4 , AlV_2O_4 and LiRh_2O_4 known so far, have shown charge frustration. In all of them the high temperature charge frustrated state is characterized by the cubic structure. They explore the configuration space in a completely different manner as they relieve the frustration with finitely many possible ground states to a particular charge ordered state, some times through orbital ordering. All of them apart from Fe_3O_4 are normal spinels existing in a cubic structure ($Fd-3m$). In all of them, the pyrochlore B sub-lattice is randomly occupied by the multiple valent transition metal ions. All of them show a “Verwey transition” like increase in resistivity of varying magnitudes as they are cooled. The resistive transition is accompanied by a structural transition.

But they assume totally different structures in their charge ordered state. None of them satisfy the Anderson’s 1:1 criterion and some of them show charge disproportionation with non integral charge states. Superlattice reflections observed in the electron diffraction patterns, have served as important input in arriving at the structural model in each of these compounds. Thus the study of frustrated spinel systems compellingly takes us to unknown territories with unpredictably plenty of possibilities into a hitherto uncharted and unexplored ground state landscapes.

Spinel systems exhibiting charge order

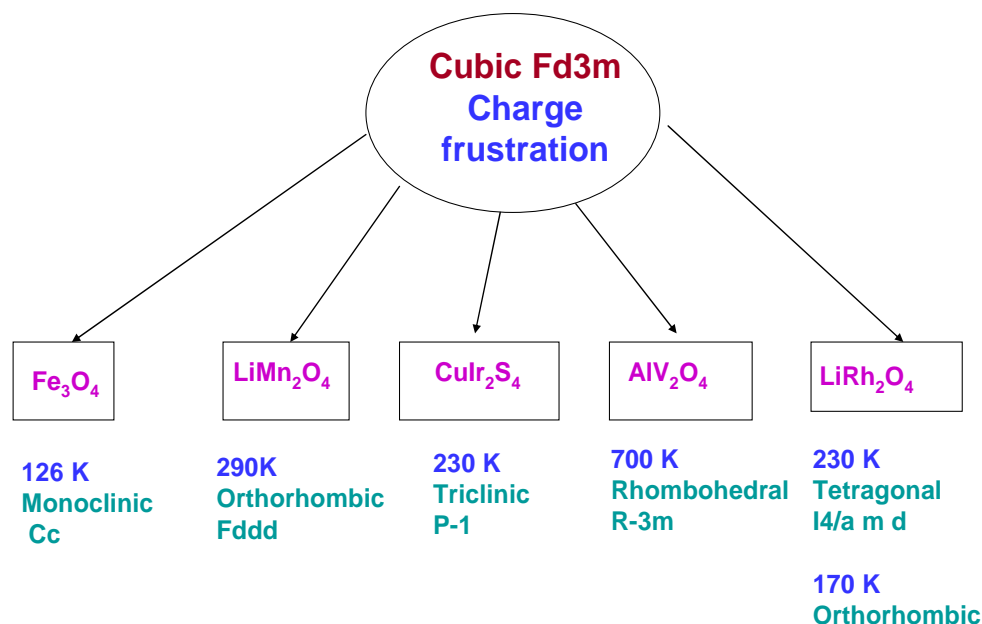


Figure 1.11 The five spinel systems that exhibit charge frustration in the cubic structure $Fd-3m$. All of them relieve the frustration through structural transition by forming unique clustering brought about by the participation of orbitals.

Owing to the complex nature of the structure and ordering, these charge frustrated spinel systems are very challenging to synthesize, to solve the crystal structure in the ordered state and to understand the role of various parameters on the charge ordered state. As it is evident a lot more needs to be studied about these just emerging systems in terms of experimentation and theoretical formulation to explore further and to reach ultimately to the mechanism of ordering from frustration. With this background it becomes essential to express the reason behind the specific choice of AlV_2O_4 and LiMn_2O_4 as the two compounds chosen for study under this thesis.

1.6 Motivation and thesis organisation

Amongst the spinel systems showing charge ordering from frustration, AlV_2O_4 stands apart, since it is the only spinel compound known so far that shows charge ordering at around 700 K. This unique feature offers a possibility to access the charge ordered state at ambient temperature. The ordering of charges itself appears to be through a novel clustering of vanadium ions in the form of a heptamer molecular unit. LiMn_2O_4 offers another interesting scenario since it shows partial charge ordering through the formation of octagonal columnar structures. Though abundantly studied for its functionality as a battery material, the charge ordering aspect is still less probed. Only a few published works exist indicating the challenges posed by these materials and hence it is motivating to synthesize and study these systems in some more detail. Also, in the parlances of strongly correlated electronic systems with myriads of surprises under their fold, the phenomenon and the physics of charge ordering itself is highly contested, more so from frustration, and hence it motivates further probing.

Thus, the present thesis engages in studying these two charge frustrated spinels (AlV_2O_4 and LiMn_2O_4) by tweaking the thermodynamic variables like pressure and temperature and tuning the charge concentration by substitution. Condensed matter tools like powder diffraction, resistivity measurement, electron energy loss spectroscopy measurements and computation of electronic structure are used in this thesis.

Thesis organization

The above review of the conceptual aspects of frustration including typical examples of charge ordering from frustration with respect to spinel system and motivation for the

investigation carried out in the present thesis work from Chapter 1. Chapter 2 discusses the aspects of synthesis and powder X-ray diffraction characterization of AlV_2O_4 and the results of the systematic high temperature powder XRD measurements confirming the structural transition from room temperature charge order phase to high temperature charge frustrated phase. Chapter 3 describes the results of synchrotron powder XRD measurements in a diamond anvil cell under hydrostatic and non hydrostatic pressures showing for the first time that the charge ordered AlV_2O_4 is driven back to frustration under high pressure. Results of the electron energy loss spectroscopy measurements and Density Functional calculations are presented in chapter 4. In chapter 5, synthesis, characterization, results of four probe resistance measurement and results of the low temperature synchrotron powder XRD measurements of another interesting charge frustrated spinel compound LiMn_2O_4 with partial substitution of Ru for Mn is presented. Finally, chapter 6 describes the conclusions of the present thesis and lists the scope for future study.

References

- [1] E.J.Verwey, Nature **144** (1939) 327
- [2] Ken-ichiro Matsuno, Takuro Katsufuji, Shigeo Mori, Yutaka Moritomo, Akihiko Machida, Eiji Nishibori, Masaki Takata, Makoto Sakata, Naoki Yamamoto and Hidenori Takagi, J. Phys. Soc. Jpn **70** (2001) 1456
- [3] A.Yamada, M.Tanaka, Mater. Res. Bull.**30** (1995) 715
- [4] T. Furubayashi, T. Matsumoto, T. Hagino and S. Nagata, J. Phys. Soc. Japan **63** (1994) 3333
- [5] S. Kondo, D.C. Johnston, C.A. Swenson et al., Phys. Rev. Lett. **78**, (1997) 3729
- [6] D. C. Johnston: J. Low Temp. Phys. **25** (1976) 145
- [7] M. Isobe and Y. Ueda, J. Phys. Soc. Jpn.**71** (2002) 1848; M. Schmidt, W. Ratcliff, P. G. Radaelli, K. Refson, N. M. Harrison and S.W. Cheong, Phys. Rev. Lett. **2** (2004) 56402

- [8] W.F. Giauque, and J.W. Stout, J. Am. Chem. Soc. **58** (1936)1144
- [9] Linus Pauling, J. Am. Chem. Soc. **57** (1935) 2680
- [10] J. D. Bernal & R. H. Fowler, J. Chem. Phys. **1** (1933)515
- [11] Yuri B Kuda ,Sov Phys-Usp **55** (2012)1169
- [12] A.P. Young, Pramana, J. Phys. **64** (2005)1087
- [13] M. J. Harris et al., Phys. Rev. Lett. **79** (1997) 2554.
- [14] *Frustrated Spin Systems*, ed. H.T. Diep, World Scientific(Singapore)2004
- [15] Erland M. Schulson JOM **51** (1999) 21
- [16] G. H. Wannier, Phys. Rev. **79** (1950) 357
- [17] P.W. Anderson, Phys. Rev. **102** (1956)1008
- [18] M. Iizumi, T.F. Koetzle, G. Shirane, S. Chikazumi, M. Matsui and S. Todo, Acta Crystallogr. B. **38** (1982) 2121
- [19] J. P. Wright, J. P. Attfield and P. G. Radaelli ,Phys. Rev. Lett. **87** (2001) 266401
- [20] G. Subias, J. Garcia, J. Blasco, M.G. Proietti, H. Renevier and M.C. Sanchez
Phys. Rev. Lett. **93** (2004)156408; Subias G, Garcia J, Proietti M G, Blasco J,
Renevier H, Hodeau J L and Sanchez M C , Phys. Rev. B **70** (2004) 2155105
- [21] Mark S Senn, Jon P. Wright and J. Paul Attfield, Nature **481** (2012)173
- [22] Jeroen van den Brink and Daniel I Khomskii, J. Phys.: Condens. Matter **20** (2008)
434217
- [23] C. Masquelier, M. Tabuchi, K. Ado, R. Kanno, Y. Kobayashi, Y. Maki, O.
Nakamura and J. B. Goodenough, J. Solid State Chem. **123** (1996) 255
- [24] R. J. Gummow, A. DeKock and M. M. Thackeray, Solid State Ionics **69** (1994) 59
- [25] J. B. Goodenough, Annu. Rev. Mater. Sci. **28** (1998) 1
- [26] J. Rodriguez-Carvajal, G. Rouse, C. Masquelier, and M. Hervieu, Phys. Rev.
Lett. **81** (1998) 4660
- [27] A. Paolone, C. Castellano, R. Cantelli, G. Rouse and C. Masquelier, Phys.
Rev. B **68** (2003) 014108
- [28] Izumi Tomeno, Yusuke Kasuya and Yorihiro Tsunoda, Phys. Rev. B, **64** (2001)
094422
- [29] A. S. Wills, N. P. Raju, and J. E. Greedan, Chem. Mater. **11** (1999)1510
- [30] Y. Oohara, J. Sugiyama, and M. Kontani, J. Phys. Soc. Jpn. **68**, (1999) 242
- [31] Hirota, K. D. E. Cox, J.E. Lorenzo, G. Shrone, J. M. Tranquada, M. Hase, K.
Uchinokura, H. Kojima, Y. Shibuya and I. Tanaka, Phys. Rev. Lett. **73** (1994)736
- [32] Furubayashi, T., Matsumoto, T., Hagino, T. & Nagata, S. J. Phys. Soc. Jpn **63**,

(1994) 333

- [33] H. Ishibashi, T. Y. Koo, Y. S. Hor, A. Borissov, P. G. Radaelli, Y. Horibe, S-W. Cheong and V. Kiryukhin, *Phys. Rev. B* **66** (2002) 144424
- [34] Shoichi Nagata, *Chinese Journal of Physics*, **43** (2005) 722
- [35] Y. Horibe, M. Shingu, K. Kurushima, H. Ishibashi, N. Ikeda, K. Kato, Y. Motome, N. Furukawa, S. Mori and T. Katsufuji, *Phys. Rev. Lett.* **96** (2006) 086406
- [36] Yasuhiro Shimizu, Moe Tanaka, Masayuki Itoh and Takuro Katsufuji, *Phys. Rev. B* **78** (2008) 144423
- [37] Yongmao Cai, Zu-Fei Huang, Xing Ming, Chunzhong Wang, Gang Chen, *Journal of Alloys and Compounds* **505** (2010) L23
- [38] Ø. Prytz, E. Flage-Larsen, L. Gu, W. Sigle, P. A. van Aken and J. Taftø, *Phys. Rev. B* **85** (2012) 195112
- [39] Croft M, Kiryukhin V, Horibe Y and Cheong S-W, *New J. Physics* **9** (2007) 86
- [40] Yoshihiko Okamoto, Seiji Niitaka, Masaya Uchida, Takeshi Waki, Masashi Takigawa, Yoshitaka Nakatsu, Akira Sekiyama, Shigemasa Suga, Ryotaro Arita, and Hidenori Takagi, *Phys. Rev. Lett.* **101** (2008) 086404

CHAPTER 2

Sample preparation, characterization and high temperature powder XRD study of AlV_2O_4

This Chapter lists the available literature on the synthesis of AlV_2O_4 and the actual synthesis procedure used in the present work in section 1. The laboratory source X-ray diffraction is largely used for phase analysis, characterization and high temperature XRD in this thesis work. Hence the necessary details of alignment, geometry and calibration of the laboratory diffractometer for ambient and high temperature XRD measurements have been described in section 2. Powder X-ray diffraction characterization and confirmatory electron diffraction characterization of AlV_2O_4 are presented in section 3. Lattice parameter calculation using Rietveld refinement is presented in section 4. Subsequently, section 5 carries the results of the high temperature powder XRD measurements on AlV_2O_4 , confirming the structural transition from the room temperature charge ordered rhombohedral phase to the high temperature charge frustrated cubic phase. The results are summarized at the end of this chapter.

2.1 Introduction

Among the charge frustrated spinel systems with formula AB_2O_4 , the compound AlV_2O_4 is unique, since, at ambient temperatures, it exists in the charge ordered state. In general, in a spinel structure, a cation with valency 3+ occupies the octahedral B site and a cation with valency 2+ occupies the A site to maintain charge neutrality as in MgAl_2O_4

[1]. In the special case of AlV_2O_4 , Al with 3+ valency is forced to occupy the A site with tetrahedral co-ordination. Therefore the multivalent vanadium occupies the octahedral B-site. Charge neutrality demands disproportionation on vanadium. Thus in the cubic phase vanadium is expected to exist as V^{2+} and V^{3+} . A survey of the existing literature points out that AlV_2O_4 is also one of the less probed systems. The earliest mention (1965) of AlV_2O_4 is in ICDD data bank [2] (card # 25-0025). It is mentioned that this compound forms in the tetragonal structure and is supposed to transform reversibly to a cubic phase at 310 °C. There are almost no further studies reported in the literature on AlV_2O_4 . Recently Matsuno *et al* [3] have synthesized AlV_2O_4 , probably with a motivation to examine Anderson's criterion [4] in yet another spinel system. A multivalent vanadium ion in the spinel B-lattice certainly serves as a candidate of choice. AlV_2O_4 is synthesized by Matsuno *et al* [2] using a solid state synthesis route. The synthesis method suggested in their paper has been adopted for the present thesis. The chemical reaction that leads to the formation of the compound is as follows:



To synthesize 1 gm of the sample, following raw materials are required (as per the stoichiometry):

Al - 0.1399 g

V_2O_3 - 0.3886 g and

V_2O_5 - 0.4715 g

Therefore, stoichiometric quantities of Al (Alfa Aesar 99.97%, Melting Point (MP) 660 °C), V₂O₃ (Alfa Aesar 99.7%; MP 1970 °C) and V₂O₅ (Alfa Aesar 99.99%; MP 690 °C) have been weighed, ground thoroughly, made into 8 mm dia and 2 mm thick pellets. The pellets have been placed in a thoroughly cleaned 12 mm dia quartz tube closed at one end. The quartz tube with the pellets, is evacuated to 5×10^{-5} mbar, using a rotary and diffusion pump for about three hours and sealed. Liquid nitrogen cold trap is ensured to be filled during pumping. Then the evacuated quartz tube is introduced into a furnace and the pellets are calcined at 1150° C for 150 hours. At the end of 150 hours, the furnace is switched off and the pellets are taken out. A part of the pellet has been ground finely for characterization using powder X-ray diffraction.

2.2 Details of the laboratory diffractometer, alignment calibration and high temperature attachment

2.2.1 Description, alignment and calibration of the laboratory source powder diffractometer

The powder diffractometer is the most basic tool required for phase analysis of the synthesized sample. It becomes essential to align the diffractometer and calibrate it to get excellent quality data for further analysis. The diffractometer used for the present study is shown in figure 2.1. The STOE make $\theta - \theta$ diffractometer operates from -10° to $+168^\circ$. Precise angular positions (0.001°) can be set by a stepper motor with reproducibility. A minimum step size of 0.001° is possible. Manual control for angle movement is also available. The radius of the measuring circle is 275 mm. The diffractometer can operate in the theta–two theta, two theta and omega scan modes. The tube housing accommodates an X-ray tube of a long, fine focus type with spot size 12 mm x 0.4 mm. The X-ray tube

used in the line focus mode, for the present work is a Philips (9430 027 83001 (PW2783/00)) ceramic tube with a Cu target.

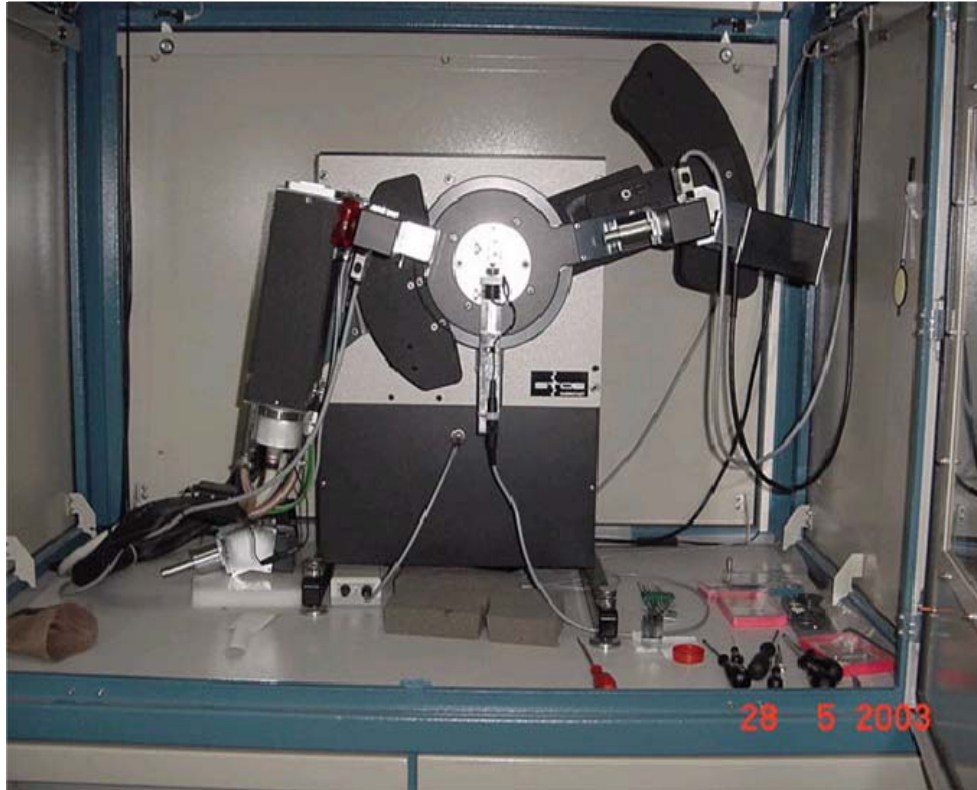


Figure 2.1 *The STOE $\theta - \theta$ diffractometer operating in the Bragg- Brentano geometry.*

The tube is powered by a 4 kW air cooled generator. The target is cooled by chilled water supply line using a dedicated chiller unit. Chilled water is made to circulate at the rate of about 3.75 liter/m so as to cool the Cu target. The X-rays that emanate from the tube at a take off angle of 6° are sent through “Soller slits” for controlling vertical beam divergence without sacrificing the intensity. Such a Soller slit assembly is also available at the diffracted beam end. The sample holder is a zero background plate, in the present case a Silicon (911) single crystal wafer which can be positioned at the center of the

diffractometer circle with the help of a knife edge. A 10 mm x 0.1mm diameter groove is made at the center of this plate for loading finely ground powder samples.

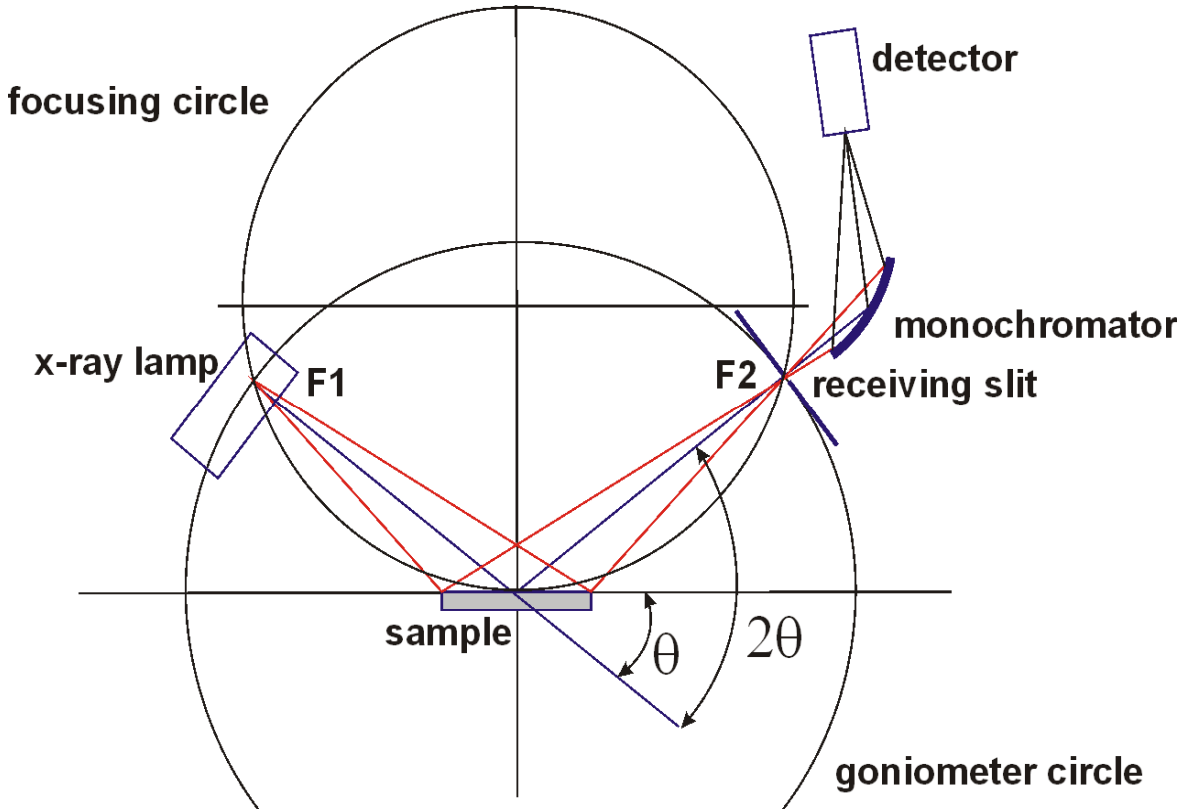


Figure 2.2 Schematic of a diffractometer in the Bragg-Brentano Geometry

The zero background plate and the horizontal sample holder assembly ensure a negligibly small background that can be easily modeled during analysis. The incident and diffracted X-ray beam divergence can be adjusted by a computer controlled precision slit from 0.01 to 2 mm. A secondary monochromator (plane graphite) is also provided for rejecting any stray X-ray contamination. A substantial intensity of the diffracted beam is made possible because of the Bragg-Brentano para-focusing geometry [5-6]. In this geometry the specimen is placed at the center of the diffractometer circle. The X-ray

source, the sample and the detector lie tangentially along the focusing circle as shown in the schematic figure 2. The detector is always at an angle of 2θ and the sample is at θ with respect to the incident beam. In the Bragg-Brentano geometry the diffraction vector is normal to the (911) planes and does not satisfy Bragg's law. Therefore there will be no diffraction peaks from the sample holder. A NaI (Tl) scintillation detector optically coupled to a photo multiplier tube is used for receiving the diffracted beam. For every absorbed X-ray quanta a pulse of about 1 Volt is produced. Since this process requires less than a micro second, the counter operates at the rate of 10^5 counts per second. The diffractometer alignment is ensured on a periodic basis by checking the direct beam, alignment of the tube, alignment of the sample holder with respect to the tube and finally the alignment of the detector with respect to both the sample holder and the tube. Calibration of the diffractometer using NIST standard Si powder is carried out everyday before commencing any experiment. This procedure ensures that there is no inadvertent zero shift of the diffractometer.

A typical XRD data obtained from a standard Si powder collected at 0.05 step size and 12 sec/step is given in the figure 2.3. The data has been collected at a divergent and receiving slit width set to 0.3 mm. The 100% peak corresponding to the reflection from (1 1 1) plane of Si is obtained at a two theta value of $28.443 (+/- 0.001)^\circ$.

This compares exceedingly well with the data for Si in the ICDD data card (# 2714-02). The FWHM is found to be 0.11° . Due care is taken to powder the sample finely, before loading the sample on the Si zero background plate. While the powder is pressed gently for preventing heaping, care is exercised to avoid preferred orientation of the particles. The diffractometer is provided with a dedicated chiller. The high temperature powder

XRD measurements have been carried out on a SIEMENS 500 (theta – two theta) diffractometer to which a high temperature attachment can be included. Alignment and calibration of the diffractometer is carried out routinely as mentioned in the case of STOE make diffractometer. The description of the high temperature attachment is presented in the following section.

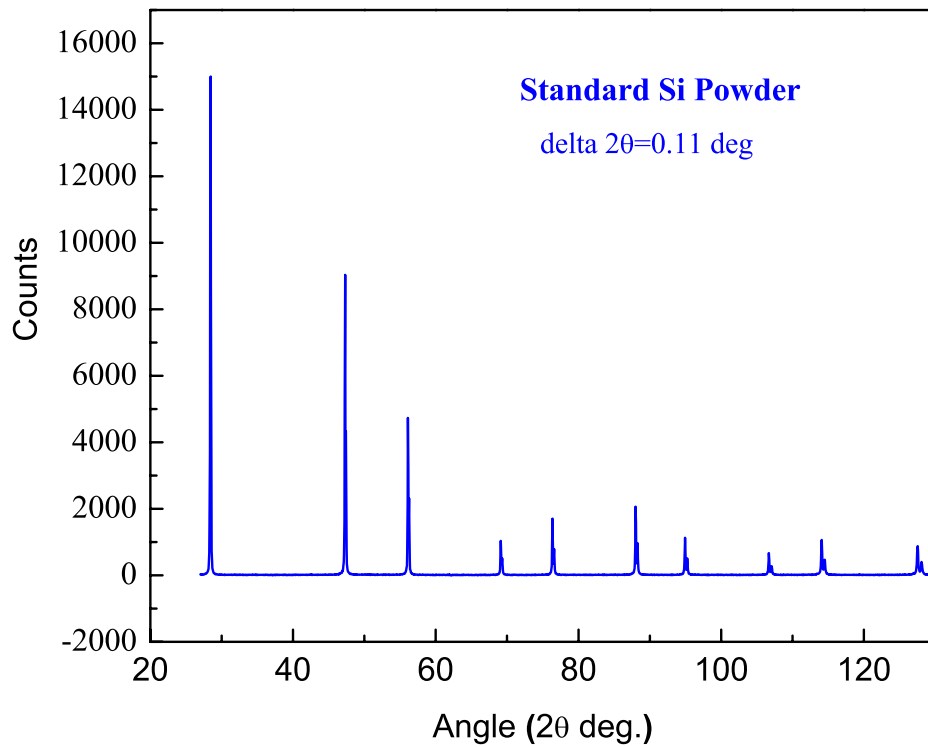


Figure 2.3 Calibration of the diffractometer - Data presented is for Standard Si Powder

2.2.2 The High temperature attachment for powder diffraction

The high temperature attachment enables heating of the specimen in vacuum and obtaining powder diffraction data at every controlled temperature. The commercially procured Edmund Bühler make, model D-7400, HDK-2.3 HT attachment can be

positioned on the Siemens Diffractometer so that the sample is at the center of the diffractometer circle. The sample holder assembly is connected to a turbo molecular pump for evacuation.

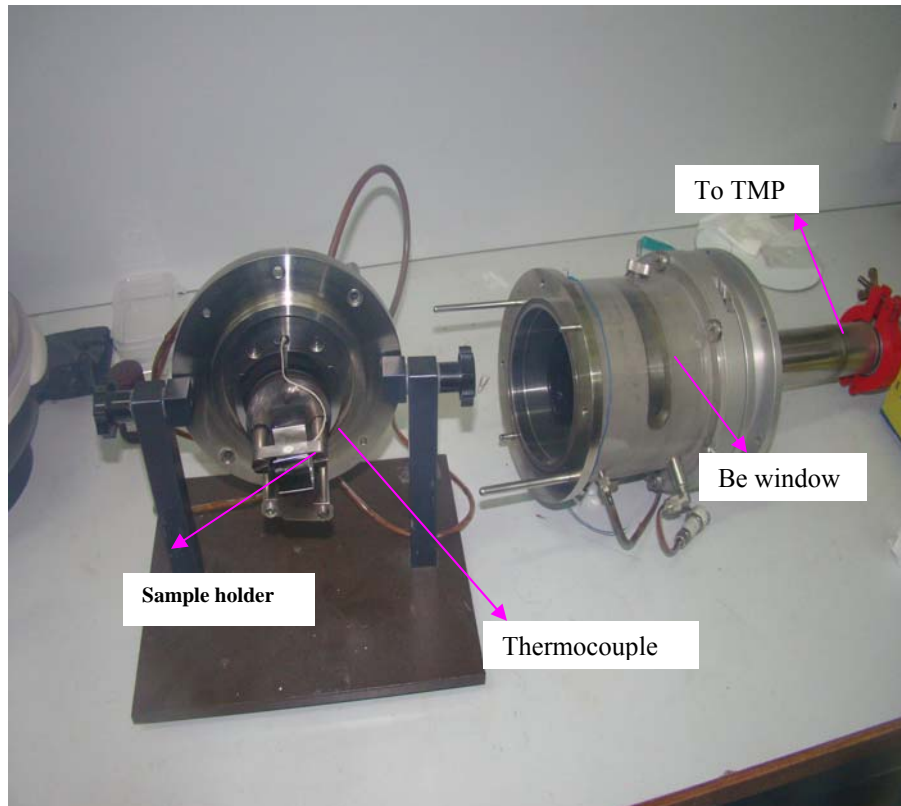


Figure 2.4 *High Temperature attachment to the powder diffractometer. The Ta sample holder, W-Re thermocouple and the Be window are marked for ease of identification.*

The front cylindrical enclosure has a beryllium window for allowing the incoming and diffracted X-ray beam. The sample holder is a tantalum foil with a dent at the center to place the sample powder. A W-Re thermocouple is spot welded at the bottom of the cup to measure and control the temperature. Current flows through the sample holder (Ta foil) and heats up the sample. Heating the radiation shield that surrounds the sample holder controls radiation losses. A PID temperature controller ensures temperature stability which is about 0.1 K at any set temperature, for a period of more than 10 hours

for collecting one set of data points depending on the step size requirement. Before commencing the data collection, alignment of the diffractometer is ensured by obtaining the diffraction pattern for the standard Si powder. Powder XRD data can be obtained by heating the specimen up to about 1500° C.

2.3 Characterization of the sample

2.3.1 Powder XRD characterisation

The structural characterization of the sample begins with the phase analysis of the synthesized powder. A small portion of the synthesized AlV_2O_4 powder is finely ground and placed on the zero background Si sample holder in the STOE diffractometer. Powder diffraction patterns are obtained with 0.1° step size. Data collection is carried out for 10 sec at each step. Formation of AlV_2O_4 appears to be very sensitive to synthesis parameters. Quality of quartz tubes and vacuum are the only known parameters that could be tightened. Since it was observed that the so called ‘identical’ conditions did not yield identical results, a number of batches of samples are synthesized and good quality samples from among them have been picked for further studies. It must also be stressed that there is no deterioration of the chosen good quality samples over the period of two years as substantiated by subsequent XRD characterization carried out many times in between. All batches of samples had Al_2O_3 as impurity. The best samples had about 5% Al_2O_3 . Once formed, Al_2O_3 is very difficult to be removed due to its very high MP (2072 °C). Many times, subsequent grinding and a further heat treatment at 1100 °C have resulted in complete loss of AlV_2O_4 phase. Typical results from the synthesis of AlV_2O_4 are presented here to exemplify the efforts.

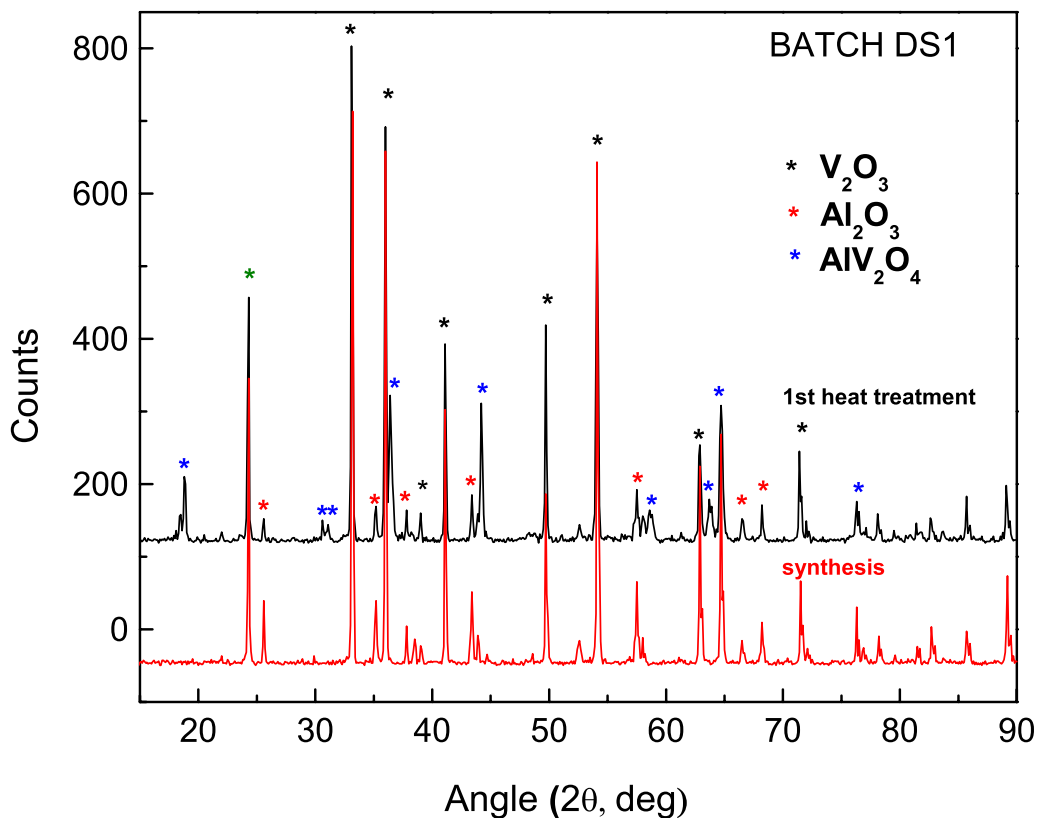


Figure 2.5: Formation of AlV_2O_4 ; during the first heat treatment (red), un-reacted raw materials are seen. A subsequent heat treatment results in partial formation of AlV_2O_4 (black).

Figure 2.5 shows the synthesis effort in one of the batches. Initially the stoichiometric pellets placed in evacuated quartz tube are heated to 1100 °C for 150 hours. Powder XRD characterization (shown in red) clearly indicates presence of un-reacted V_2O_3 and dominant Al_2O_3 peaks implying oxidation of Al. Hence the pellets are reground and pelletized and once again subjected to the same heating schedule in an evacuated quartz tube. It is observed from the spectrum (shown in black) that AlV_2O_4 forms, but a lot of raw materials are lost as Al_2O_3 and V_2O_3 . A further heat treatment results in complete loss of AlV_2O_4 and a variety of vanadium oxides are observed to have formed along with Al_2O_3 .

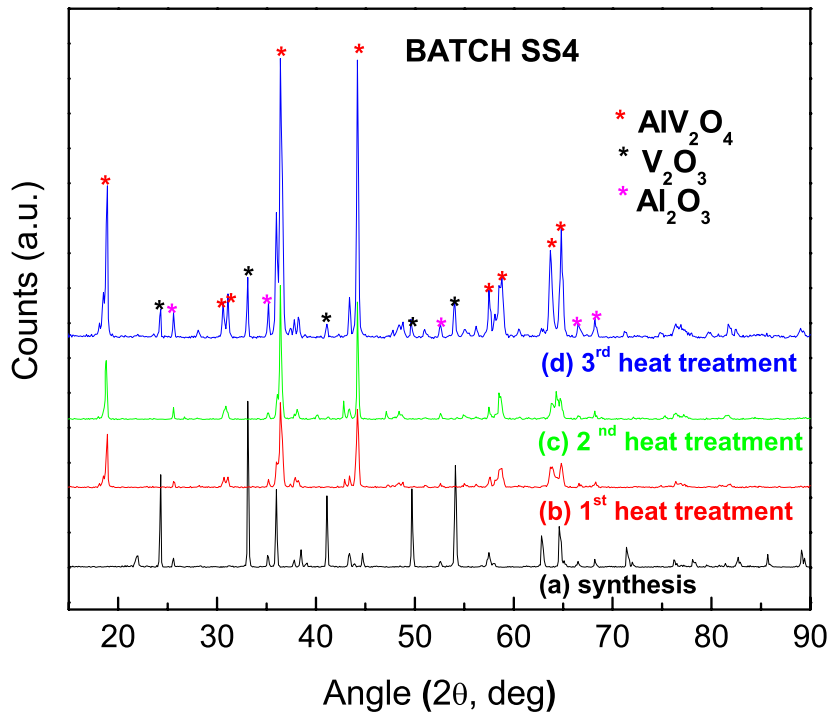


Figure 2.6: Formation of AlV_2O_4 ; (a) partially reacted raw materials; (b) formation of AlV_2O_4 with Al_2O_3 impurity phase; (c) persistent presence of Al_2O_3 along with AlV_2O_4 ; (d) dissociation of AlV_2O_4 as seen from the emergence of V_2O_3 peaks.

Powder XRD pattern corresponding to yet another batch is shown in figure 2.6. Pattern (a) obtained after the initial calcinations, shows partial reaction. Pattern (b) obtained on the sample after grinding, pelletising and heat treating at 1100 °C shows the formation of AlV_2O_4 and presence of Al_2O_3 . Pattern (c) obtained after repeating the same process once again, shows persistent presence of Al_2O_3 and no reflections from V_2O_3 are seen. An attempt to give a final homogenization leads to partial dissociation of AlV_2O_4 to form V_2O_3 and Al_2O_3 as shown in (d).

Once a combination of V_2O_3 and Al_2O_3 are formed, repeated grinding, pelletising and heat treatment to get rid of them is futile in the solid state route. Instead, a fresh

attempt to synthesize must be initiated. Result of another fresh synthesis is presented in figure 2.7.

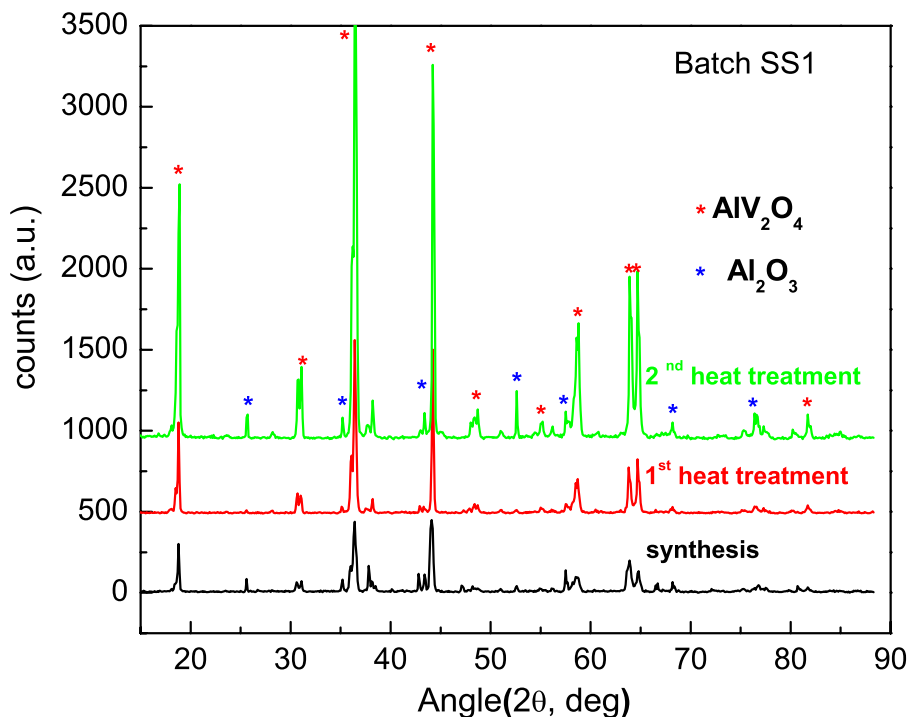


Figure 2.7: Formation of AlV_2O_4 ; (a) Formation of AlV_2O_4 at the synthesis step with some amount of Al_2O_3 (b) Retention of AlV_2O_4 with Al_2O_3 impurity phase; (c) result of second heat treatment showing about 6% of Al_2O_3 .

In this effort, the formation of AlV_2O_4 is observed right at the first calcination at 1100 °C for 150 hrs. (spectrum (a)) along with some Al_2O_3 . A second heat treatment at 1100° C in an evacuated quartz tube reduces the volume fraction of Al_2O_3 . A subsequent heat treatment brought back Al_2O_3 to about 6%. The percentage intensity is calculated by subtracting the background and normalizing the spectrum with respect to the maximum counts (not shown in the graph). At this stage no further heat treatment is taken up and

the sample is stored for further studies. Likewise many batches of samples are synthesized, and the best of them with about 5 to 6% Al_2O_3 are retained for further study.

2.3.2 Identification of structural model

At the time of commencing this thesis work, two structural models have been proposed for AlV_2O_4 in the literature. One proposed by Matsuno *et al* [3] and the other by Horibe *et al* [7].

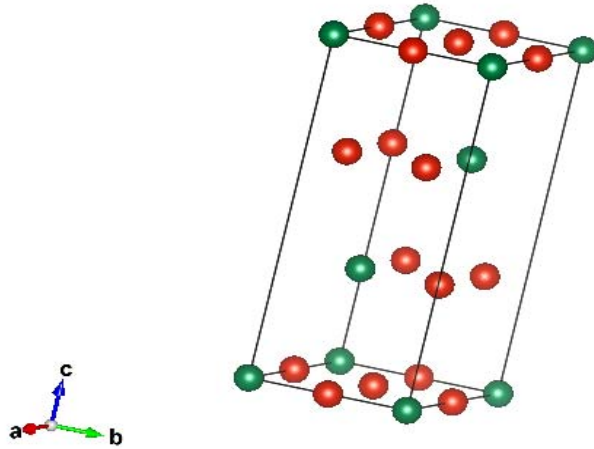


Figure 2.8: The $R-3m$ structural model with 3:1 ordering of Vanadium ions. Al and O ions are hidden for clarity. V1 ions are shown in red and V2 ions are shown in green.

From synchrotron powder diffraction experiments, Matsuno *et al* [3] had identified that at room temperature, the structure of the charge ordered phase of AlV_2O_4 is rhombohedral (space group $R-3m$) with $a_R=5.8438(7)$ Å and $\alpha=58.975(6)^\circ$ (in hexagonal notation $a=5.75304$ Å and $c=14.4242$ Å). The rhombohedral structure formed from a slight distortion of the cubic lattice has two vanadium sites V1 and V2 at Wyckoff position 3d and 1a respectively. Figure 2.8 shows the structural model depicting a 3:1 type charge

ordering of vanadium ions with artificial hiding of Al and O for clarity. Horibe *et al* [7], have also synthesized AlV_2O_4 , observed $(\frac{1}{2}\frac{1}{2}\frac{1}{2})$ type of superlattice spots through electron diffraction and identified the structure to be rhombohedral (R-3m) with three different vanadium atoms (V1, V2 and V3) at Wyckoff positions 3a, 3b and 18 h.

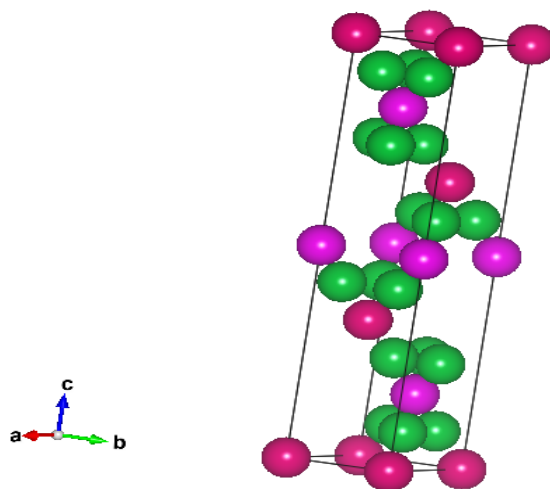


Figure 2.9: The Heptamer structural model; The loner V1 ions are in red. Within the heptamer molecule, V2 ions are shown in pink and V3 ions are in green. Al and O are hidden for clarity.

They propose formation of a heptamer molecule of seven vanadium atoms with a lone non-bonding vanadium atom. The heptamer structural model is shown in figure 2.9 displaying only the vanadium ions for clarity. The V3 trimers (green) with a V2 (pink) form the heptamer. The V1 are the non-bonding loner ions. The V3 trimers form a kagome` plane. V1 and V2 form triangular planes.

The powder XRD pattern of AlV_2O_4 synthesized in the present work (pink) is compared with the calculated patterns from the 3:1model (red) and the heptamer model (blue) in figure 2.10. The reflection indicated with asterisks shows the Al_2O_3 impurity. The patterns have been plotted in an expanded scale. It is observed that the matching is complete between the present work and the ‘heptamer’ model proposed by Horibe *et al*.

The 3:1 model does not seem to account for the observed peaks. Hence for the rest of this work, the heptamer structural model describing a unique charge ordered state in AlV_2O_4 is adopted.

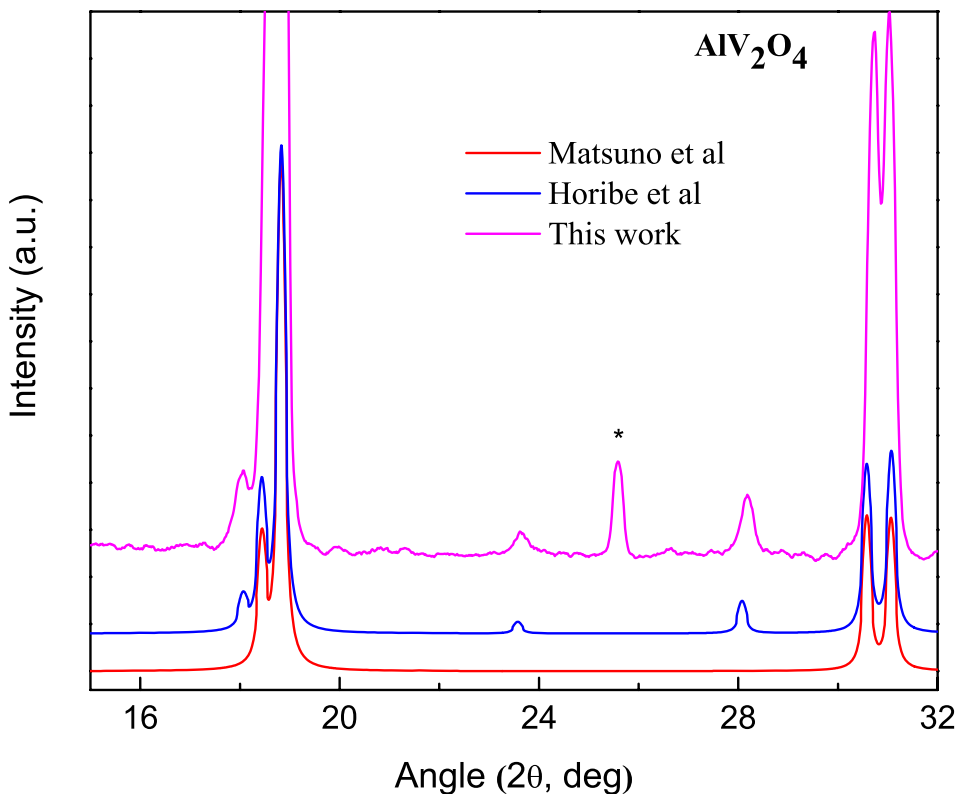


Figure 2.10: Powder diffraction pattern of AlV_2O_4 from angle 2θ ranging from 16° to 32° . The diffraction peaks in red correspond to the 3:1 model, in blue correspond to the Heptamer model and pink corresponds to the present work.

Figure 2.11 shows the powder X-ray diffraction data collected at ambient conditions on a finely ground powder sample of AlV_2O_4 in a slow scan mode using Cu K_α radiation in the STOE diffractometer. The scan is carried out at 0.02° step size with 20 sec/step acquisition time. The divergent and the receiving slits are set at 0.3 mm. Vanadium with high mass absorption coefficient at 8 keV ($221.7 \text{ cm}^2/\text{g}$) as against Al ($50 \text{ cm}^2/\text{g}$) makes it essential to count for longer time to get appreciable statistics. The pattern is indexed

corresponding to the rhombohedral (R-3m) structure as per the heptamer structural model.

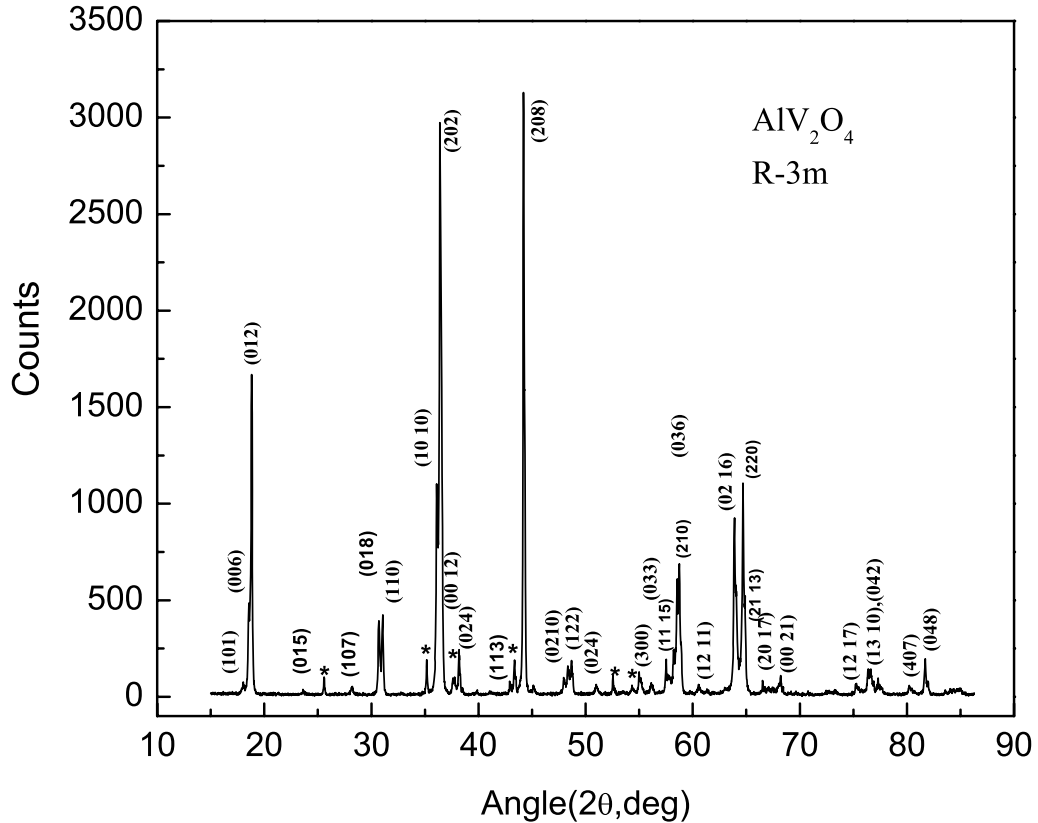


Figure 2.11: Powder diffraction pattern of AlV_2O_4 indexed as per the heptamer structural model

2.3.3 Confirmation of structure using electron diffraction

AlV_2O_4 gives the unique opportunity to observe charge ordering at room temperature. With the motivation to observe the same in the sample synthesized in this work, electron diffraction patterns on many regions of the sample are collected using LIBRA 200 FE HRTEM, a high resolution transmission electron microscope (HRTEM). A few tiny particles of the sample loaded on a carbon mesh have been observed under the microscope and ED patterns are obtained at many locations. One typical location where

the superlattice structure is clearly visible is presented in figure 2.12. The double spots are due to the chosen particle being a little thicker with an orientation mismatch between the layers. With the help of an image processing software [8] and a simulation software for reciprocal lattice, the observed spots are identified to be from $[1 -2 0]$, $[0 -1 10]$, $[-1 1 10]$ planes of the rhombohedral phase and the zone axis is determined to be $\langle 20 10 1 \rangle$ in confirmation with R-3m structure.

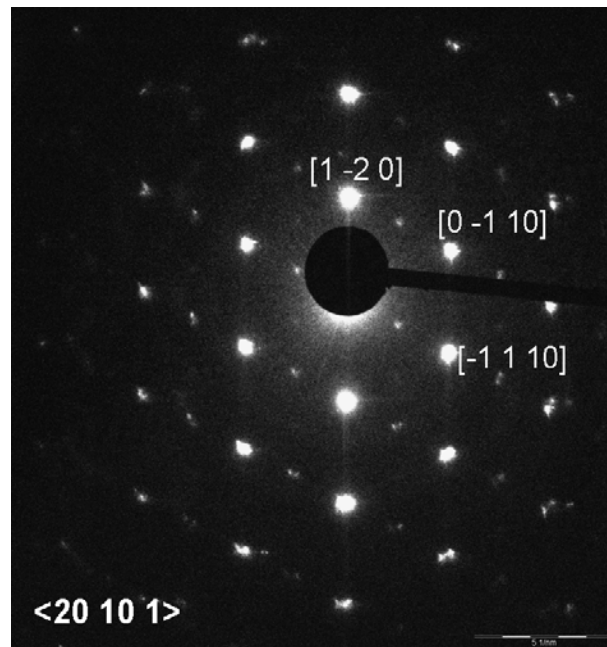


Figure 2.12: Typical electron diffraction pattern of AlV_2O_4 showing super lattice spots

2.4 Rietveld refinement

Rietveld refinement [9-10] of the powder diffraction data to refine the crystal structure can provide a wealth of information about the structural details of the material. In this method the square of the difference between the observed diffraction intensity and the calculated diffraction intensity at every point in the diffraction pattern is minimized

with a weight factor using a non-linear least square algorithm. Let y_i^c and y_i^{obs} represent the calculated and observed intensity at a point i in the diffraction pattern then,

$$\varphi = \sum_{i=1}^n w_i (y_i^{obs} - y_i^c)^2$$

is the function to be minimized. $w^i = [y_i]^{-1}$ is the weight factor. Minimization is carried out with respect to a number of parameters like background, sample displacement, sample transparency, zero shift, peak profile, unit cell dimension, scale factor, preferred orientation, positional parameters, occupancy and atomic displacement (isotropic and anisotropic) parameters. During the course of refinement the parameters are turned on sequentially and allowed to vary till stability is achieved. Every time the calculated pattern is compared with the experimental pattern and also examined by observing the residuals like profile residual R_p , weighted profile residual R_{wp} and goodness of fit χ^2 . When the algorithm is stable these residuals decrease and approach a steady minimum value indicating that the refinement can be terminated. Rietveld refinement using the GSAS package [11-12] is used for refining structural parameters in this thesis.

The powder diffraction data acquired at ambient temperature is refined using Rietveld analysis using the GSAS package [11]. The heptamer structural model has been considered as the initial model and refinement of parameters have been carried out in sequence. A two phase fitting has been carried out with AlV_2O_4 and the impurity Al_2O_3 phase. The background is fitted with the Chebyshev polynomial of the First kind and it is found to attain convergence. The profile shape is refined with the pseudo-Voigt function. No absorption correction is included as the data has been collected in the Bragg-Brentano geometry. The quality of refinement does not improve further beyond an R factor $R_p = 13.5\%$ and the reduced $\chi^2 = 2.442$. This may be due to the fact that this

analysis is carried out on the laboratory source Cu K-alpha radiation with high absorption co-efficient material like vanadium. Better fitting can be achieved with synchrotron data.

Figure 2.13 shows the result of the refinement.

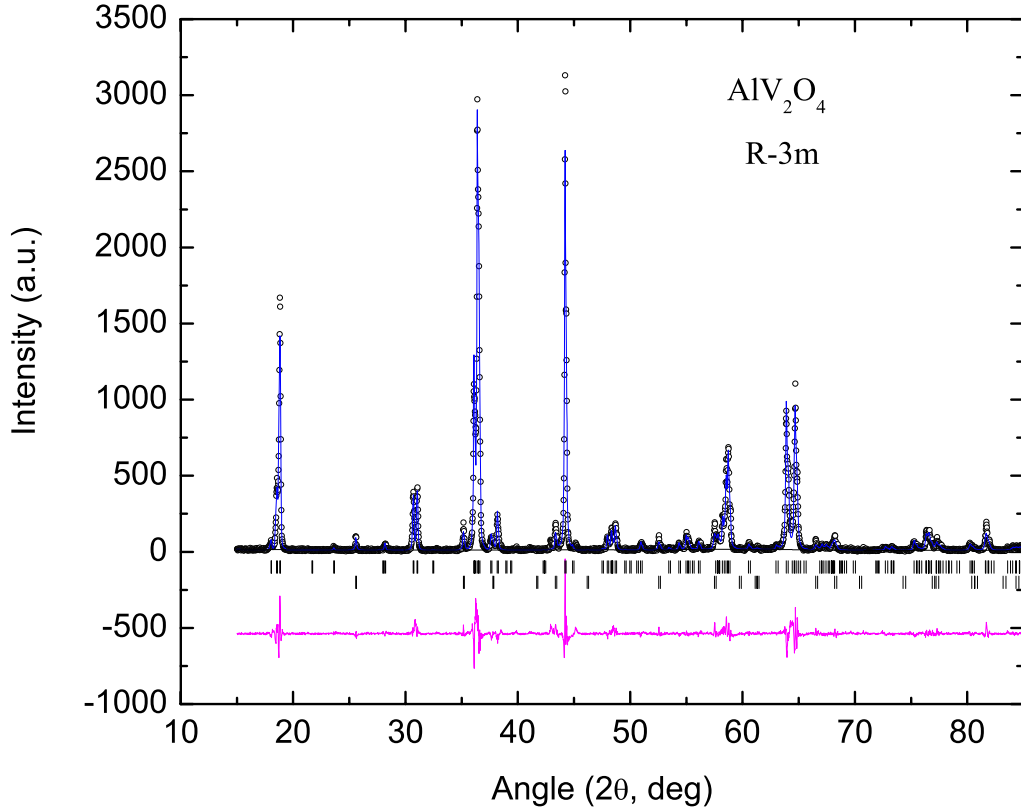


Figure 2.13: Rietveld refinement of the ambient pressure, room temperature x-ray diffraction data for AlV_2O_4 and the small impurity phase Al_2O_3 (lower calculated pattern). Points represent the experimental data, the continuous line represents the fitted data and the curve shown at the bottom is the difference plot.

The refined atom co-ordinates are given in table 1. The refined lattice parameter values are $a = b = 5.7613(2) \text{ \AA}$ and $c = 28.6876(10) \text{ \AA}$ (hexagonal notation) and the unit cell volume $V = 824.65(4) \text{ \AA}^3$. For comparison, the lattice parameter values quoted by Horibe *et al* [7] are $a = b = 5.75148(3) \text{ \AA}$ $c = 28.85407(14) \text{ \AA}$ and the cell volume is 826.615 \AA^3 . As of now in the literature this is the only data for experimental lattice parameter. It is also observed that convergence could be attained with better figure of merit as the cell

refines to the quoted values. In the absence of large number of data in the literature to compare with, it can only be tentatively concluded that, the observed variation in the lattice parameter and the cell volume may be due to anisotropic strains in the sample.

Table 2.1 Structural parameters of AlV_2O_4 at room temperature showing fractional coordinates and the isotropic atomic displacement (U_i/U_e*100) \AA^2 from Rietveld refinement of powder diffraction data collected with laboratory $Cu-K_\alpha$ x-ray source. The lattice parameters are: $a = b = 5.7613(2) \text{\AA}$ and $c = 28.6876(10) \text{\AA}$ (hexagonal notation). The cell volume = $824.65(4) \text{\AA}^3$. The R factor $R_p = 13.5\%$ and the reduced $\chi^2 = 2.442$.

| Name | site | x | y | z | U_i/U_e*100 |
|------|------|-----------|-----------|-----------|---------------|
| Al1 | 6c | 0 | 0 | 0.1840(4) | 1.94 |
| Al2 | 6c | 0 | 0 | 0.6899(1) | 2.28 |
| V1 | 3a | 0 | 0 | 0 | 2.50 |
| V2 | 3b | 0 | 0 | 0.5 | 2.50 |
| V3 | 18h | 0.4882(1) | 0.5117(9) | 0.2490(1) | 3.08 |
| O1 | 6c | 0 | 0 | 0.8773(6) | 2.74 |
| O2 | 6c | 0 | 0 | 0.6305(5) | 2.85 |
| O3 | 18h | 0.5010(3) | 0.4989(7) | 0.1259(2) | 2.26 |
| O4 | 18h | 0.5020(4) | 0.4979(6) | 0.3756 | 1.59 |

2.5 High temperature powder XRD experiments

Powder XRD measurements are carried out on a small part of finely ground powder specimen of AlV_2O_4 as a function of temperature, using the high temperature (HT) attachment to the diffractometer. Before commencement of the experiment, the diffractometer is aligned using a standard Si powder, placed on a Tantalum sample

holder. Once the Si reflections are obtained with variation in the peak positions not exceeding $\pm 0.001^\circ$ reproducibly, the alignment of the diffractometer is considered completed. Then the sample powder is loaded in the Ta sample holder and the HT chamber is evacuated. Powder diffraction data are collected at various temperatures from $15-85^\circ 2\theta$ angular range with a step size of 0.05° and 30 sec acquisition time per step. Data collection time has been roughly about 12 hrs per temperature step. Range of temperature for recording the powder diffraction data is from 410 to 575°C . For the temperatures 430, 440, 500, 550, 575°C powder XRD data covering $2\theta = 15-85^\circ$ are obtained.

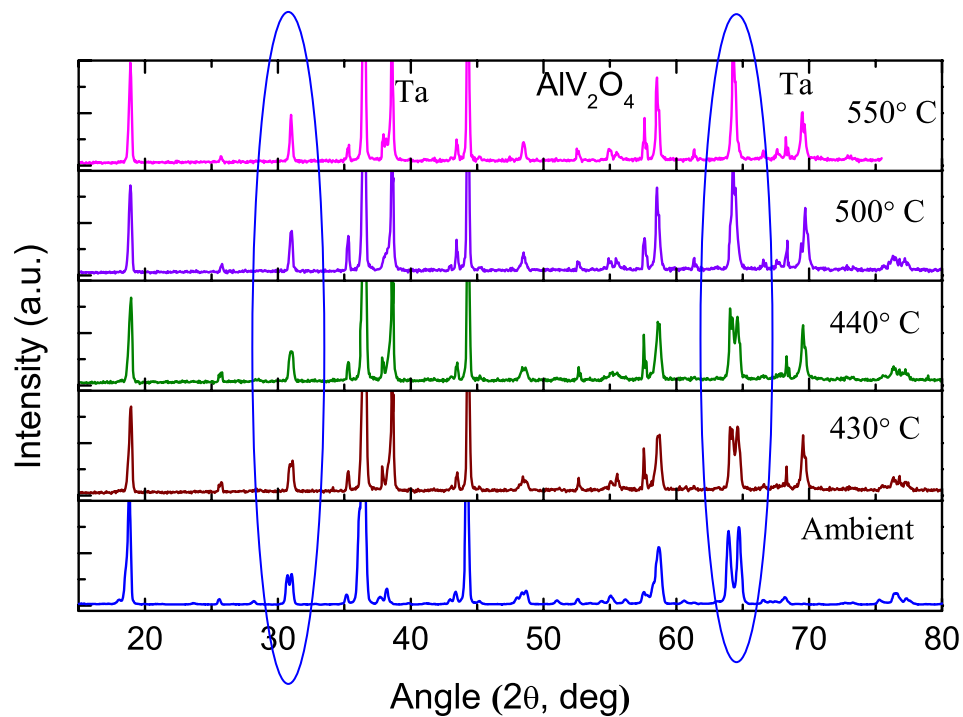


Figure 2.14: High temperature powder diffraction of AlV_2O_4 . Beyond 440°C the $(0\ 1\ 8)_R$ and the $(1\ 1\ 0)_R$ reflections (around 30° two theta) merge to $(2\ 2\ 0)_C$ and also the $(0\ 2\ 16)_R$ and the $(2\ 2\ 0)_R$ peaks (around 64° two theta) merge to $(4\ 4\ 0)_C$ - explained in the text.

At other temperatures like 410, 420, 470, 480 and 490 °C, the data collection is restricted to $2\theta = 62^\circ$ to 67° . The rhombohedral system is characterized by reflections which appear like split pairs of peaks. They are the reflections corresponding to (018), (110) planes (indicated with R in figure) and those corresponding to (0216) and (220) (indicated with R in figure) planes.

The first pair occurs around $2\theta = 30^\circ$ and the second pair at $2\theta = 64^\circ$. These reflections are absent in the high temperature cubic phase. The corresponding reflections from the cubic phase pertaining to this angular region is from the (2 2 0) and (4 2 0) planes. It can be observed that at 500°C, both the pairs disappear signaling the transformation to cubic charge frustrated phase. Analysis of all the observed patterns around $2\theta = 64^\circ$, indicates that the transition occurs between 490 °C (763 K) and 500° C (773K) (not shown). The d- spacing values corresponding to the (0216) and (220) reflections are plotted as the function of temperature. Figure 2.15 shows the observed variation. Surprisingly, while the (220) plane spacing increases as a function of temperature, it is clearly seen that, as the temperature increases from 400 to 500 °C, close to the phase transition, the d-spacing corresponding to the (0 2 16) plane decreases on heating.

Interestingly, the (0 2 16) plane contains two of the vanadium atoms forming V3 trimers that belong to the kagome' planes. They are supposed to form a bond with the V2 vanadium ions at the center of the heptamer through orbital interaction. Thus, the observation made in the present thesis clearly brings out the fact that the process of heating disturbs the V3 trimers which play a key role in the formation of heptamers. Though the data obtained from laboratory source XRD with reduced counts at higher

temperatures should not be stretched too far, it appears that the trend is correct. High temperature experiments using synchrotron source can yield better quantitative details of the nature of the structural transformation.

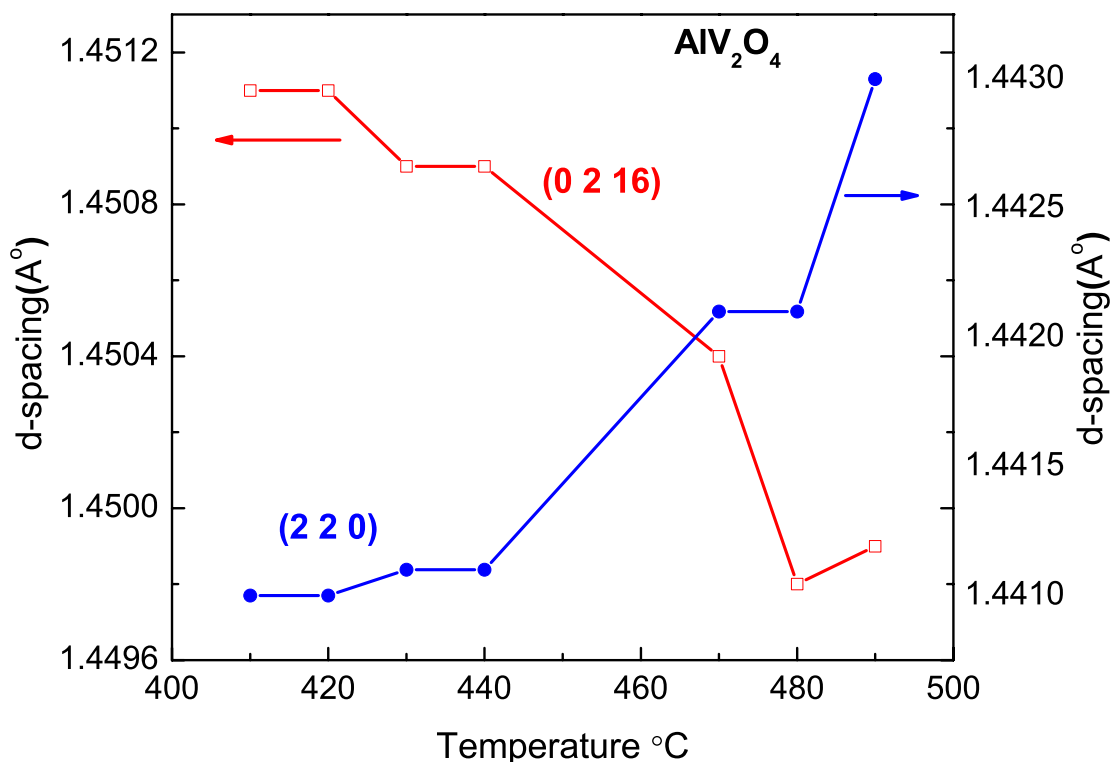


Figure 2.15: Variation of the d-spacing corresponding to the (0 2 16) plane and (220) plane as a function of temperature.

Summary of results and conclusions:

- AlV_2O_4 is synthesized using the solid state reaction route. The ambient temperature powder XRD data is indexed to the heptamer structural model.
- Rietveld refinement of the ambient temperature, slow scan powder data shows the room temperature structure of AlV_2O_4 to be R-3m. The lattice parameters

obtained are: $a=b= 5.7613 (2) \text{ \AA}$ and $c = 28.6876(10) \text{ \AA}$ and the cell volume is $824.65(4) \text{ \AA}^3$.

- High temperature powder diffraction measurements show transition from rhombohedral to cubic (Fd3m) phase, between 763 to 773 K.
- The d-spacing corresponding to the (0 2 16) plane shrinks on heating before transforming to the cubic phase. This clearly brings out the role of vanadium orbitals enabling the formation of V₃ trimers resulting in the charge ordered heptamer molecular units in the low temperature rhombohedral phase.

References

- [1] M. B. Kruger, J. H. Nguyen, W. Caldwell and R. Jeanloz, Phys. Rev. B, **56** (1997)1
- [2] Sata, Bull. Tokyo Inst. Technology **66** (1965) 85
- [3] K. Matsuno, T. Katsufuji, S. Mori, Y. Moritomoto, A. Machida, E. Nishibori, M. Takata, M. Sakata, N. Yamamoto and H. Takagi, J.Phys. Soc. Japan **70** (2001) 1456
- [4] P. W. Anderson, Phys. Rev, **102** (1956) 1008.
- [5] *Fundamentals of Powder Diffraction and Structural Characterization of Materials*, Vitalij K. Pecharsky, Peter Y. Zavalij, Springer (2003)
- [6] *Elements of X-ray Diffraction*, B. D. Cullity, 3rd Ed. Prentice Hall (2001)
- [7] Y. Horibe, M. Shingu, K. Kurushima, H. Ishibashi, N. Ikeda, K. Kato, Y. Motome, N. Furukawa, S. Mori and T. Katsufuji, Phys. Rev. Lett. **96**, (2006) 086406
- [8] Rasband, W.S., ImageJ, U. S. National Institutes of Health, Bethesda, Maryland, USA, <http://imagej.nih.gov/ij/>, 1997-2012
- [9] H.M. Rietveld, Acta Cryst. **22**, (1967) 151; H.M. Rietveld, J. Appl. Cryst. **2** (1969) 65.
- [10] R.A. Young, *Introduction to the Rietveld method*, in: R.A. Young, Ed., *The Rietveld method*, Oxford University Press, Oxford, New York (1993).
- [11] A.C. Larson and R.B. Von Dreele, "General Structure Analysis System (GSAS)", Los Alamos National Laboratory Report LAUR 86-748 (1994).
- [12] B. H. Toby, EXPGUI, a graphical user interface for GSAS, J. Appl. Cryst. **34** (2001) 210

CHAPTER 3

Pressure induced frustration in charge ordered spinel AlV_2O_4

AlV_2O_4 provides a unique opportunity to probe the charge ordered state at ambient temperature. Exploiting this unique feature high pressure measurements are carried out at ambient temperature on AlV_2O_4 in this thesis work. Such an effort is the first of its kind on AlV_2O_4 . The present chapter elaborates this effort. Section 1 begins with an introduction to the role of high pressure experiments in condensed matter physics. A brief review of the high pressure measurements available in the literature, on the five known spinel compounds exhibiting charge ordering, is presented in section 2. This is expected to motivate the relevance of the present high pressure powder diffraction efforts on AlV_2O_4 . The details of the high pressure powder diffraction experiments carried out on AlV_2O_4 under non-hydrostatic and hydrostatic conditions using diamond anvil cell are presented in section 3 and 4 respectively. The results of the analysis of the high pressure powder XRD measurements and the possible origin of pressure induced frustration in AlV_2O_4 are discussed in section 5. The summary of the results and the conclusions drawn are placed at the end.

3.1 Introduction

Condensed matter is characterized by the complex many body interactions. It is indeed formidable to fully solve the many body quantum mechanical Hamiltonian and obtain the ground state and the quasi particles of the system. Instead, experimental tools have served to probe condensed matter and bring out a multitude of interesting results. In that context, subjecting condensed matter specimens to very high pressures have brought

forward many interesting results [1] which have provided insight into the physics of the complex correlated electronic systems. To cite a few examples, application of very high pressures of the order of 150 GPa have shown that an ionic solid and an inert gas assume similar hexagonal close packed structure with metallic conductivity. Pressure induced insulator to metal transition has been observed in many materials. In fact a few insulators and semiconductors have become superconductors under pressure. Apart from driving many elements to superconducting state, pressure affects the observed superconducting transition temperature [2]. In the case of colossal magneto resistance (CMR) materials, typically some of the half doped compounds like $\text{Pr}_{0.5}\text{Sr}_{0.5}\text{MnO}_3$, $\text{Nd}_{0.5}\text{Sr}_{0.5}\text{MnO}_3$ and LaMnO_3 exhibit pressure-induced metallization through the collapsing of the charge ordered state. But other compounds like $\text{La}_{0.5}\text{Ca}_{0.5}\text{MnO}_3$ shows pressure induced charge localization attributed to be caused by development of monoclinic distortion due to charge and orbital ordering [3]. A wealth of literature exist enlisting pressure induced amorphization [4]. To summarise, pressure alters the condensed matter properties by modifying the band width or band gap of the materials in some instances and in certain other cases, application of pressure results in kinetically driven structural modifications. Various experiments like resistivity, powder diffraction, specific heat and magnetization can be performed under high pressure. The addition of Diamond anvil cell (DAC) reaching up to multi-mega bar pressures and the availability of intense synchrotron X-ray sources with micron size beam have widened especially the scope of studying structural transitions. It is of interest to figure out how far these tools have been used to study the ordering of charges in the spinel system. Hence the following section carries a brief review of high pressure experiments on these charge frustrated spinels.

3.2 A brief review of the effect of pressure on the charge frustrated spinel compounds

Fe₃O₄

The earliest and most contested charge ordered spinel compound Fe₃O₄ has been studied extensively using powder diffraction, resistivity and magnetization techniques under pressure in DAC. High pressure powder XRD on Fe₃O₄ up to 20 GPa at 300 K has not shown any structural transformation [5]. Results of resistivity and magnetization measurements under pressure at close to zero Kelvin seem to indicate quantum critical behaviour of Fe₃O₄ [6]. The Verwey transition temperature decreases as a function of pressure. At 8 GPa there is no more Verwey transition, and Fe₃O₄ remains metallic. Recent Fe K-edge magnetic circular dichroism measurements using synchrotron radiation under variable temperature and pressure has brought out a new magnetic transition (spin state) between 12-16 GPa and between 40-300 K temperatures [7]. To the best of the literature survey carried out for the present thesis, no X-ray diffraction measurements bringing out structural details below the Verwey transition as a function of pressure can be located.

LiMn₂O₄

LiMn₂O₄ is known to transform from an ambient temperature frustrated cubic (Fd3m) structure to a partially columnar charge ordered orthorhombic (Fddd) structure around 290 K. Most of the studies carried out on this system focus on the structural transitions pertaining to stability of the system as a battery material. In that context many HP-HT studies seem to have been performed on this material showing cubic to tetragonal or orthorhombic structures [8 - 9]. Very recently commercially obtained LiMn₂O₄ has

been studied under both hydrostatic and non-hydrostatic conditions in a DAC up to 15 GPa at ambient temperature [10]. The cubic $Fd\bar{3}m$ structure transforms to a tetragonal structure under pressure. Pronounced differences exist between the observations at non-hydrostatic and hydrostatic conditions. In non-hydrostatic conditions, the sample transforms to a tetragonal structure at 0.4 GPa and remains tetragonal till 5.3 GPa. Interestingly, even after decompression the tetragonal structure remains. Whereas the sample subjected to hydrostatic pressure transforms to a mixture of tetragonal phases ($F4_1/ddm$ and $I4_1/amd$) at 12.2 GPa. These are actually high pressure measurements on the charge frustrated cubic phase. There are no high pressure measurements on the charge ordered phase that exists below 290 K.

CuIr₂S₄

The chalcogenide spinel $CuIr_2S_4$, yet another charge frustrated cubic spinel system, undergoes a structural transition accompanied by a resistivity increase of a few orders of magnitudes to a triclinic structure (P-1) at 230 K. Once again, only ambient temperature HPXRD and high pressure resistivity measurements are available in the literature [11-12]. $CuIr_2S_4$ shows a large increase in resistivity up to 12 GPa and beyond this pressure the resistivity starts falling till 30 GPa where saturation is observed. The HT-HPXRD shows transformation from cubic to tetragonal structure. Even in this material, the HPXRD in the charge ordered state is not available.

AlV₂O₄ and LiRh₂O₄

These two systems are relatively recently identified to show charge ordering transition. So far the role of high pressure on the charge ordered state has not been explored. Since AlV_2O_4 transforms to the frustrated cubic spinel phase only above 700

K, it is convenient to experiment on the charge ordered state under pressure at ambient temperature itself. Hence in the present thesis HPXRD measurements have been carried out in both the non-hydrostatic and hydrostatic pressure conditions at ambient temperature.

3.3 High pressure powder diffraction studies on AlV_2O_4 Under non-hydrostatic condition

3.3.1 Diamond anvil cell assembly and experimental details



Figure 3.1: *Diamond Anvil Cell assembly. Arrow mark indicates the location of the diamond. The culet size is 300 micron.*

The diamond anvil cell (DAC) used for high pressure measurements is shown in figure 3.1. A pair of brilliant cut gem quality diamonds with culet size $300\ \mu\text{m}$ forms the heart of the DAC. Rhenium foil of $200\ \mu\text{m}$ thickness and indented to $50\ \mu\text{m}$ thickness is used as the gasket material. An $80\ \mu\text{m}$ diameter hole drilled at the center of the indented area of the rhenium gasket serves as the sample space. A portion of the sample (AlV_2O_4)

has been finely ground and loaded along with a few grains of platinum in the cell. No pressure-transmitting medium is used. Hence the sample has been studied under non-hydrostatic pressure conditions. The Pt grains that have been loaded along with the sample serve as the pressure marker. Applied pressure is calculated using the Vinet equation of state for Pt. According to the Vinet equation of state [13]

$$P = 3B_o \left[\frac{1-x}{x^2} \right] \exp[1.5(B_o' - 1)(1-x)]$$

where, P is the applied pressure, B_o (262 Gpa) and B_o' (3.96) are the bulk modulus and its first derivative and x is given by a/a_o where a_o is the lattice parameter of Pt at ambient pressure and a is its lattice parameter at the measurement pressure.

The high pressure powder diffraction experiments have been carried out at the beam line 12.2.2 [14] of the Advanced Light Source (ALS), Lawrence Berkeley National Laboratory (LBNL), USA. A beam size on the sample is 10 μm x10 μm . A MAR 345 image plate detector is employed for data collection. Calibration of the X-ray wavelength and sample to detector distance is carried out using the standard LaB₆ powder. The image plate data are integrated using the FIT-2D software [15]. From the integration, the sample-to-detector distance of 394.504 mm and the x-ray wave length of 0.4959Å have been obtained. High pressure powder XRD measurements are carried out up to 30 GPa with many intermediate pressure steps. The intensity vs. two theta data collected at every pressure value has been analyzed to obtain cell refinement and estimation of lattice parameters.

3.3.2 Transformation of AlV₂O₄ from rhombohedral to cubic structure

Figure 3.2 shows the results of the high pressure powder diffraction measurements, indicating clearly the transformation of the charge ordered rhombohedral phase back to the frustrated cubic spinel phase beyond 22 GPa, as seen from the

disappearance of the $(3\ 0\ 6)_r$, $(0\ 3\ 6)_r$, $(2\ 1\ 10)_r$, $(0\ 2\ 16)_r$ and $(2\ 2\ 0)_r$ peaks and the appearance of the $(3\ 3\ 3)_c$ and $(4\ 4\ 0)_c$ peaks of the cubic phase. The transition is relatively abrupt in pressure (figure 3.2), demonstrating that the coalescence in these lines cannot be attributed to the effect of simple non-hydrostaticity-induced peak broadening.

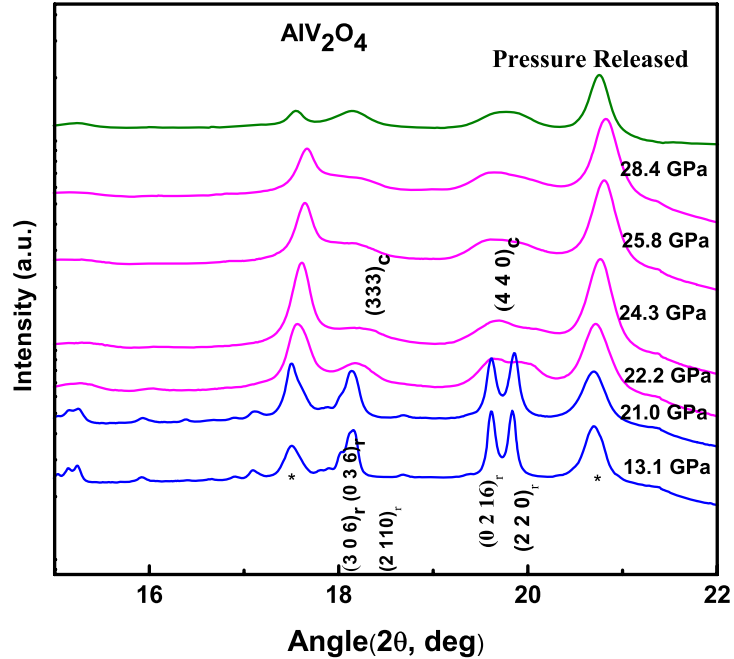


Figure 3.2: A portion of the powder diffraction data as a function of pressure for AlV_2O_4 . For pressures beyond 22 GPa, AlV_2O_4 shows the charge frustrated cubic phase. Note that the charge disordered phase is retained even after pressure release. Al_2O_3 is denoted by asterisks.

Furthermore, the powder diffraction data for the sample after decompression continues to show the peaks corresponding to reflections from the planes of frustrated cubic lattice ($a = 8.1546 \text{ \AA}$) and did not completely revert back to the rhombohedral phase. Indeed the discrete diffraction peaks observed in the rhombohedral phase that coalesce at the transition are not recovered on decompression, although we cannot exclude the possibility that small degrees of diffuse scattering from the rhombohedral

phase may be present in the quenched sample. Moreover, a considerable amount of peak broadening is also retained on decompression (as seen in figure), implying that there may be irreversible effects of strain within these samples.

3.3.3 Rietveld Refinement of powder diffraction data under non-hydrostatic pressure

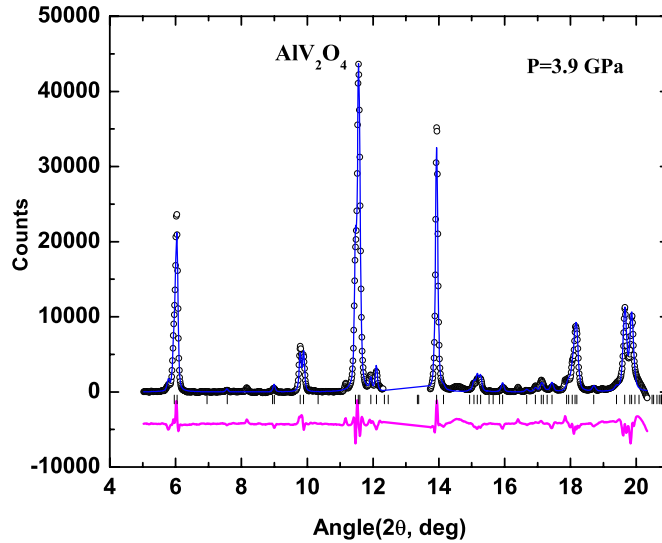


Figure 3.3: Rietveld refinement of the ambient temperature x-ray diffraction data for AlV_2O_4 at 3.9 GPa. Points represent the experimental data, the continuous line (blue) represents the fitted data and the curve shown at the bottom (pink) is the difference plot.

Refinement of the powder diffraction data is carried out for the data corresponding to lower pressures. After refining the background, the diffraction profile is fitted with Pseudo-Voight function. This is followed by refining the lattice constants, atom co-ordinates and thermal parameters. Convergence has been monitored by following the values of the residuals and also by simultaneously plotting the fitted and the observed data to have a visual feel for the goodness of fit. The angular region

corresponding to Pt reflection is excluded from refining. Structural parameters from Rietveld refinement are presented in table 3.1.

Table 3.1 Structural parameters of AlV_2O_4 at room temperature and 3.9 GPa showing fractional co-ordinates and the isotropic atomic displacement (U_i/U_e*100) \AA^2 from Rietveld refinement of powder diffraction data collected with $\lambda=0.4959\text{\AA}$.

| Name | site | x | y | z | U_i/U_e*100 |
|------|------|-----------|-----------|------------|---------------|
| Al1 | 6c | 0 | 0 | 0.1804(6) | 2.5 |
| Al2 | 6c | 0 | 0 | 0.6916(7) | 2.75 |
| V1 | 3a | 0 | 0 | 0 | 1.4 |
| V2 | 3b | 0 | 0 | 0.5 | 2.84 |
| V3 | 18h | 0.4856(5) | 0.5143(5) | 0.2506(1) | 2.9 |
| O1 | 6c | 0 | 0 | 0.8874(5) | 1.63 |
| O2 | 6c | 0 | 0 | 0.6388(5) | 3.4 |
| O3 | 18h | 0.4987(8) | 0.5012(1) | 0.1223(5) | 1.56 |
| O4 | 18h | 0.5047(5) | 0.4952(4) | 0.3738 (1) | 3.0 |

For the applied pressure corresponding to 3.9 GPa, the lattice parameters obtained from the refinement are, $a = b = 5.7527 (3) \text{\AA}$, $c = 28.6187(25) \text{\AA}$, the cell volume is $820.21(9) \text{\AA}^3$ and the R values that qualify the fitting are $R_{wp}=1.41$; $R_p=1.0$; $Ddw= 1.25$ and $\chi^2=3.96$. Table 3.2 shows the V-V distances obtained in the literature [18], from Rietveld refinement carried out as a part of this work at ambient pressure and temperature (Chapter 2). Bond lengths obtained at a few non-hydrostatic pressures are also shown in table 3.2. It is to be observed that the V3-V3 distances do not show two different values under pressure. For higher pressures where broadening is pronounced and counting statistics is not favorable, conventional peak finding and lattice parameter refinement using AIDS 83 routine has been performed. Individual reflections from the data sets are carefully fitted using a peak-fit routine with a Gaussian profile. The extracted peak

positions are indexed. The refined lattice parameters and unit cell volumes are obtained using the AIDS 83 routine.

Table 3.2. Variation of V - V distances in the kagome plane ($V3$ - $V3$) and across the kagome` and triangular planes ($V1$ - $V3$ and $V2$ - $V3$) obtained from refining of the non-hydrostatic pressure data.

| | V1-V3 (Å) | V2-V3 (Å) | V3-V3 (Å) |
|------------------------------------------|-----------|-----------|------------------------|
| Horibe et al [18] Ambient Pressure | 3.0394 | 2.8087 | 2.6101 3.1413 |
| Present work Ambient Pressure | 3.0001(2) | 2.8238(2) | 2.6740(1) 3.0850(2) |
| 3.4 GPa | 3.0242(1) | 2.7926(2) | 2.6105(1) |
| 3.5 GPa | 3.0225(1) | 2.7911(3) | 2.6092(1) |
| 3.9 GPa | 3.0225(1) | 2.7910(1) | 2.6089(2) |
| 16.0 GPa | 3.0193(1) | 2.7883(1) | 2.6050(6) |

3.3.4 Variation of lattice parameter under non-hydrostatic pressure

The refined lattice parameters of the rhombohedral and the cubic phase are shown in figure 3.4. The ‘ a ’ lattice parameter of the rhombohedral phase are denoted as a_R (filled red squares). The c lattice parameter are folded and presented as $c_R/3$ (filled red triangles) for viewing convenience. These are seen to merge beyond 22 GPa. The estimated lattice parameters of the cubic cell are shown as a_c (filled blue circles). Thus it has been clearly observed from the high pressure powder XRD measurement that a transition from the ambient pressure rhombohedral phase (charge ordered state) to the high pressure cubic phase (charge frustrated state) occurs in AlV_2O_4 .

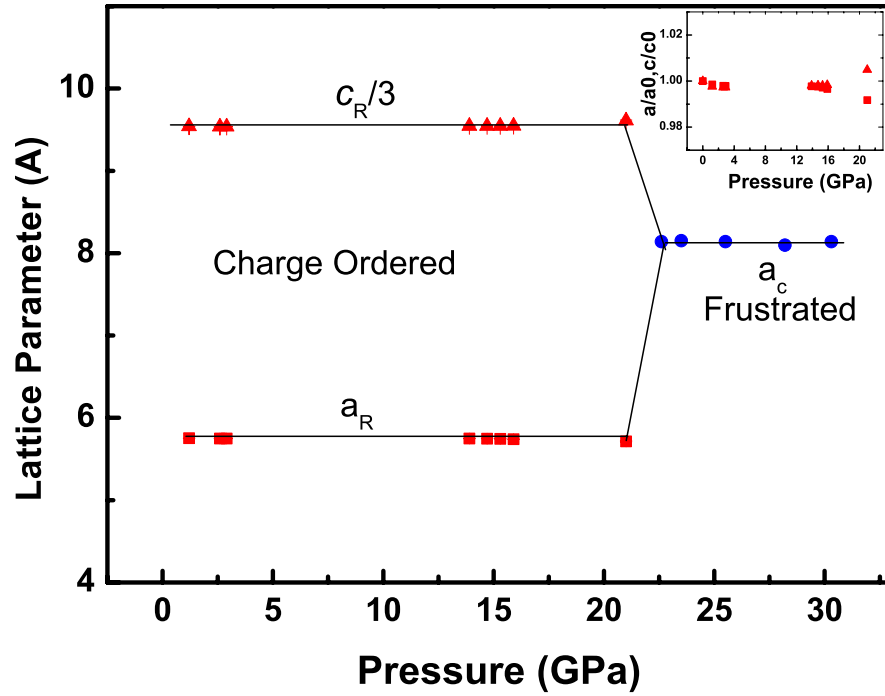


Figure 3.4: Variation of lattice parameters of the rhombohedral phase (a_R and $c_R/3$) and cubic phase (a_c). Inset shows the relative variation of the rhombohedral lattice parameters as a function of pressure for AlV_2O_4 .

Inset to figure 3.4 shows the relative variation of both the lattice parameters of the rhombohedral phase. The calculated values indicate that the lattice parameter a shows a decrease of 0.7% and the lattice parameter c shows an overall increase of 1% before the system undergoes the transformation. It is estimated that within the rhombohedral phase, the linear compressibility is -3.2×10^{-4} along the a -axis and $+0.4 \times 10^{-4} \text{ GPa}^{-1}$ along the c -axis. The calculated linear compressibility values are small compared to those observed in many cubic spinel compounds [19]. The reason for this is attributed to the non-hydrostaticity of the applied pressure.

3.4 Hydrostatic pressure studies on AlV_2O_4

3.4.1 Details of the experiment

The hydrostatic pressure experiments on AlV_2O_4 powder have been carried out at the West - B1 beam line at CHESS, USA. A pair of brilliant cut gem quality diamonds with culet size 300 μm has been used in a symmetric-type diamond cell. A Steel gasket with a hole size of 100 μm and thickness of 60 μm is used to contain the sample. Measurements have been performed on a portion of the sample which is finely ground and loaded with a few grains of ruby as the pressure marker. The beam size is 10 μ x 10 μ . A mixture of methanol and ethanol in the ratio 4:1 is used as pressure transmitting medium. Powder diffraction data at every pressure value is collected using a MAR 345 image plate detector. Angle and sample to image plate distance calibration are carried out with CeO_2 .

Integrating the calibration data using Fit-2d routine, the X-ray wavelength and the sample to detector distance d are obtained to be 0.485846 \AA and 416.4625 mm respectively. Owing to the lower flux the data collection at every pressure is carried out for 600 sec. The quality of the obtained data is just enough to see the splitting of the diffraction peaks and estimate the lattice parameters. But to perform Rietveld analysis, better quality data is required and hence refinement is deferred for a future experiment.

3.4.2 Structural transformation confirmed under hydrostatic pressure

The powder diffraction pattern obtained is presented in the figure 3.5. All the observed peaks are indexed. The indices of charge ordered rhombohedral phase are shown at the bottom of the figure. The indices of the charge frustrated cubic phase are indicated at the top of the figure. Reflections from the Al_2O_3 impurity are represented by asterisks. The gasket reflections are indicated by the letter G. The pattern corresponding

to the lowest pressure of 1.6 GPa shows the signature reflections of the rhombohedral system, namely the reflections corresponding to the (006) and (012) planes, (018) and (110) planes and (0216) and (220) planes. The intensity of all the reflections reduces and broadens as the pressure increases. From 21.3 GPa onwards, the above mentioned characteristic reflections disappear and the pattern could be indexed to the cubic structure. After data collection at 33.7 GPa, the decompression is initiated. Once the cell is completely decompressed, the last of the diffraction pattern is collected.

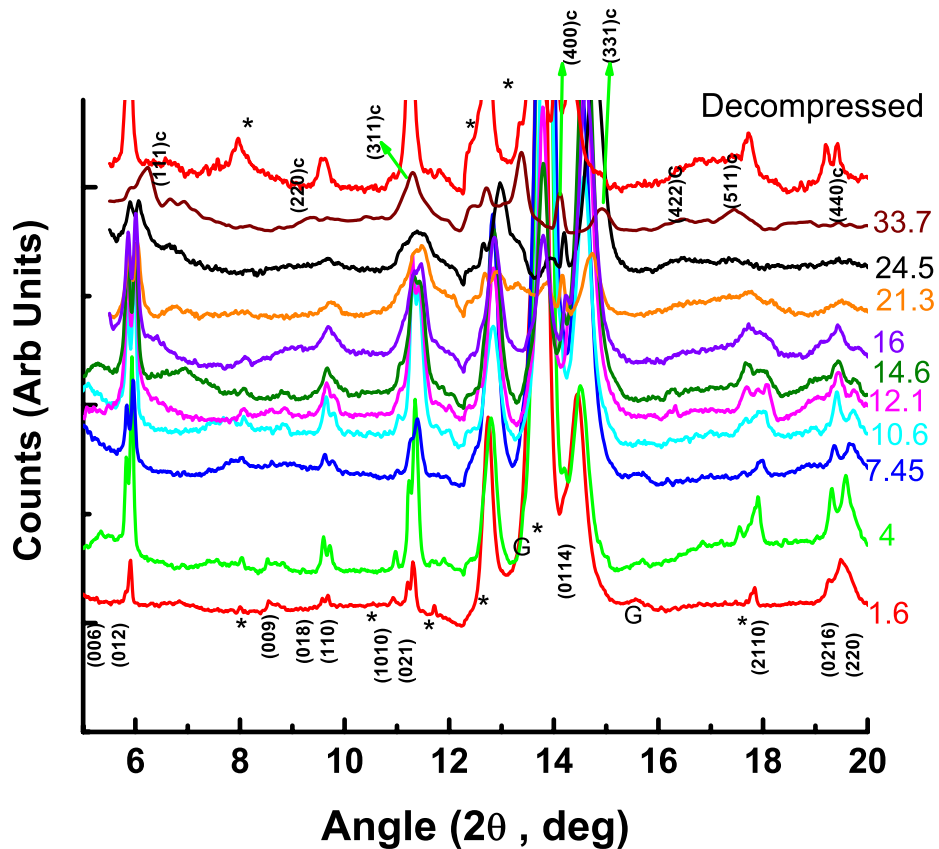


Figure 3.5: Powder diffraction patterns of AlV_2O_4 obtained under hydrostatic pressure. The applied pressure in GPa is mentioned on each pattern.

In figure 3.5 it can be seen that the pattern corresponding to complete decompression shows the characteristic reflections from (0 2 16) and (2 2 0) planes of the rhombohedral

phase. Unlike the non-hydrostatic pressure condition, where the cubic phase is retained irreversibly on decompression, AlV_2O_4 is observed to revert back to the charge ordered phase on decompression from hydrostatic pressure. Though beyond 10 GPa, the hydrostaticity actually modifies to quasi-hydrostaticity, it brings out the reversible nature of the transition.

3.4.3 Variation of volume/formula unit under hydrostatic pressure

From the intensity Vs two theta data corresponding to each pressure, a Gaussian peak fit approach is used to identify the peak positions. The AIDS 83 routine is used to estimate the lattice parameters. At high pressures due to the quality of the data identifying precise peak position turns out to be difficult. Therefore lattice parameters also carry higher error bars. With the obtained lattice parameters, the volume per formula unit is calculated for both the rhombohedral and cubic phases for each of the pressure applied. A similar peak identification, lattice parameter estimation and calculation of the volume per formula unit are performed for the data obtained after complete decompression. The obtained volume per formula unit is plotted as a function of pressure. The volume corresponding to decompression is indicated by the arrow. Figure 3.6 shows that the volume per formula unit decreases as the pressure is increased. This reduction continues till about 21 GPa, beyond which there is a transition to the cubic phase. After transformation to the cubic phase the volume per formula unit within the cubic phase also decreases. On inspection, this decrease appears to be more than that of the rhombohedral phase implying that the cubic phase may not be as stiff as the rhombohedral phase. This observation made in the present study that pressure induces frustration on a charge ordered system is significant. To examine the role of pressure within the charge ordered

rhombohedral phase, the relative variation of the lattice parameters are calculated and presented in figure 3.7.

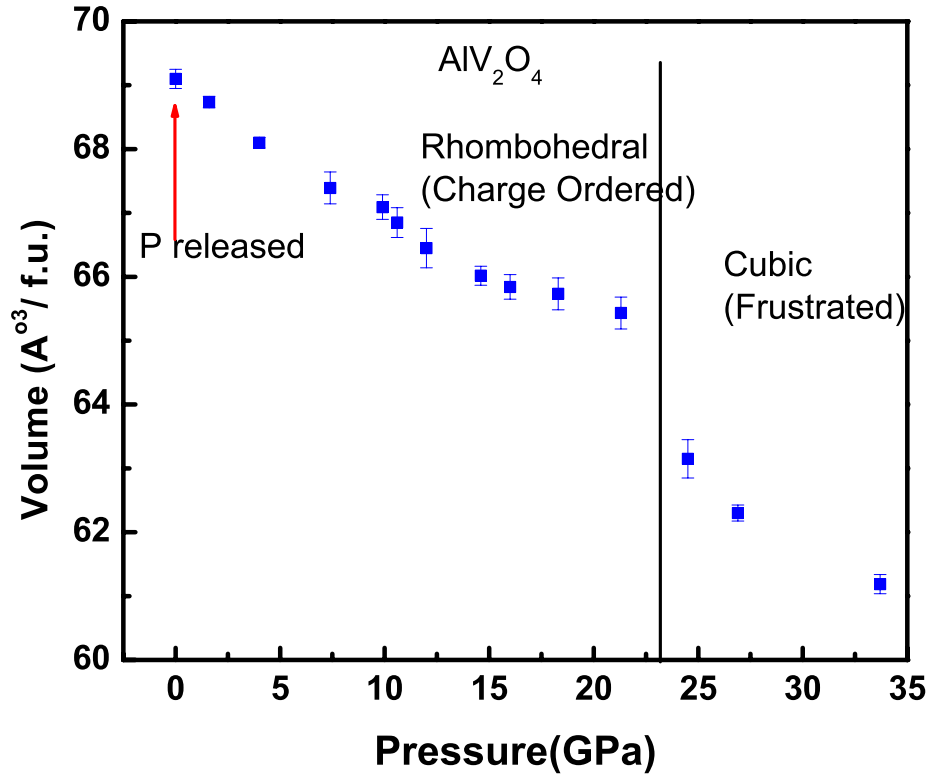


Figure 3.6: Observed variation of volume/formula unit as a function of pressure in the charge ordered rhombohedra and frustrated cubic phases

From this figure it can be observed that, both a and c lattice parameters show more compression in comparison with the non-hydrostatic situation (inset to figure 3.4).

The estimated linear compressibility is -1.05×10^{-3} along the a -axis and $-3.8 \times 10^{-4} \text{ GPa}^{-1}$ along the c -axis in the rhombohedral phase. The cubic phase shows a relatively higher compressibility of $-2 \times 10^{-3} \text{ GPa}^{-1}$. All these observations may have implications in the

retention of heptamer clusters proposed to be essential in the charge ordering transition in this system.

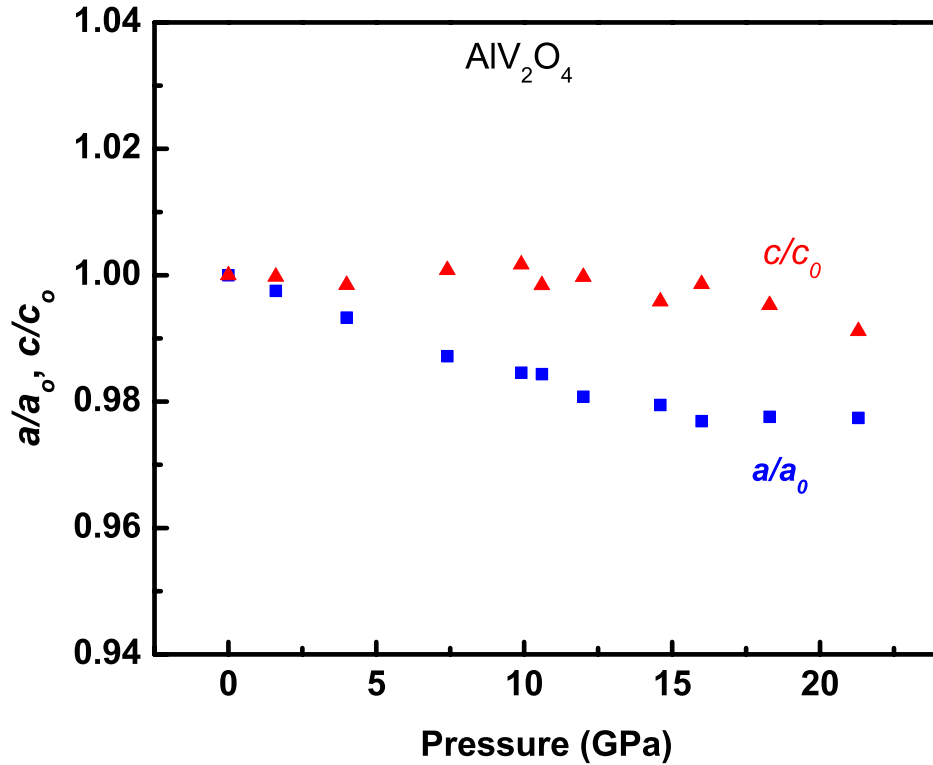


Figure 3.7: Relative variation of rhombohedral lattice parameter as a function of hydrostatic pressure for AlV_2O_4 .

3.4.4 Equation of state (EOS) of the charge ordered rhombohedral phase

An estimate of bulk modulus of AlV_2O_4 is carried out by fitting the available quality P-V data obtained from the experiments under hydrostatic pressure conditions, to the third order Birch-Murnaghan equation of state. Figure 3.8 shows the result of the fitting. The bulk modulus (B_0) corresponding to the rhombohedral phase is estimated to be 240.5 ± 5 GPa and the value of the first derivative (B_0') is 6.49. The obtained B_0

value compares with the value estimated from the total energy calculation (shown in chapter 4). This value is considered as a ball park estimate and precision can be obtained with an excellent quality powder diffraction data under hydrostatic pressure. The increased value of B_0' estimated from the fitting is expected to become better, if good quality image plate data can be obtained from diffraction and also if the pressure is estimated from fitting the equation of state of a calibrant like Pt

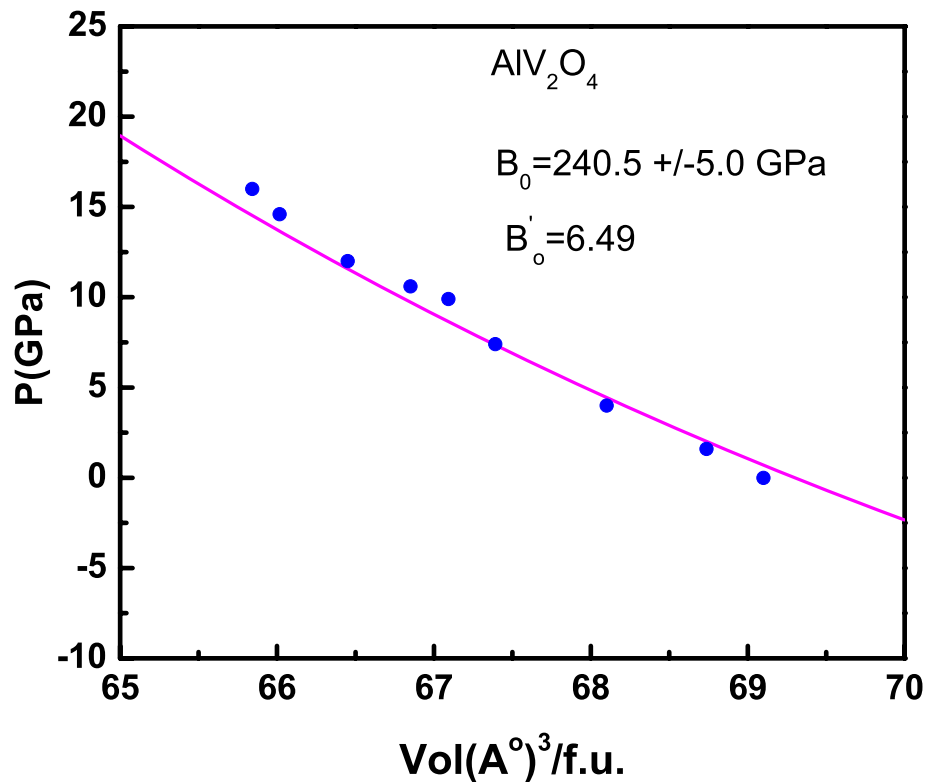


Figure 3.8 : Equation of state of AlV_2O_4 obtained by fitting the P - V data to third order Birch-Murnaghan equation

3.5 Discussion of the results of the high pressure experiments on AlV_2O_4

The transition to the cubic structure (frustrated) under pressure in AlV_2O_4 observed in this study raises interesting questions about the charge ordered state in this

system. It can be recalled that in the case of high temperature powder diffraction studies on AlV_2O_4 described in chapter 2, the (0 2 16) and (2 2 0) planes have been found to respond to the variation in temperature leading to the phase transition again from rhombohedral(charge ordered) to cubic (frustrated) structure. These are the planes containing V3 vanadium trimer. According to the ‘heptamer’ model proposed [18], charge transfer from V3 trimers of the kagome’ lattice to V2 vanadium in the triangular lattice stabilizes the heptamer and V1 remains alone in a non-bonding state. The charge transfer itself is supposed to be brought about between the V cations in the heptamer through the t_{2g} orbital. Ordering of 1-d orbital chains in AlV_2O_4 is also proposed in the literature, as the precursor to charge ordering [20]. It is also known that substituting a few of the V atoms in AlV_2O_4 with Cr (which acts as a quenched charge impurity) destabilizes the charge order [21-22] through the formation of micro domains of charge frustrated regions. Evidence for the disruption of long range charge order has been provided using the high resolution imaging. Thus it can be inferred from the powder XRD studies at high pressure and at high temperature carried out as a part of this thesis and also from the Cr substitution studies in the literature that the charge ordered state in AlV_2O_4 is indeed very delicately balanced and gets disrupted by the application of pressure, temperature or an ‘impurity doping’. In the case of structural transitions in spinels involving multivalent B-cations, a 1:1 ordering of the charges is anticipated from Anderson’s rule. Specifically in the case of AlV_2O_4 , neither 1:1 or 3:1 ordering could be observed. This may imply a stronger role for the partially filled d-orbitals of vanadium in aiding the transition. In this context it would be interesting to learn that the rhombohedral and the cubic phases are very much related and can transform from one to the other with minimal change in position. Figure 3.9 shows the structure of AlV_2O_4 drawn using

VESTA (A Three-Dimensional Visualization System for Electronic and Structural Analysis) [23].

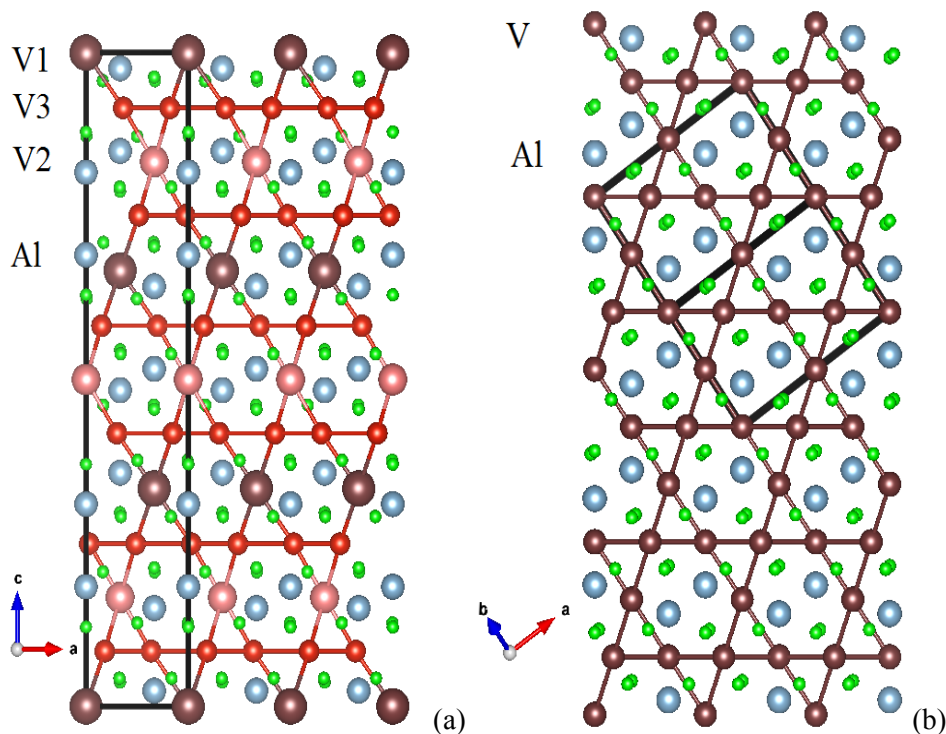


Figure 3.9 Structure of AlV_2O_4 in the relevant directions; (a) Rhombohedral phase in the (0-10) projection with three different vanadium ions; (b) Cubic phase in (0-11) projection.

The (0-10) projection of the rhombohedral phase is presented in the in figure 3.9 (a) and the (0-11) projection of the cubic phase is shown in figure 3.9 (b). Figure 3.9 (a) clearly brings out the rearrangement of vanadium as V1, V2 and V3 with V3 and V2 forming the heptamer. It is also pointed out in the literature that in the case of AlV_2O_4 , there may be an orbital ordering of vanadium t_{2g} (d_{xy}) orbitals. Such a picture of 1-D orbital ordering of the d_{xy} orbitals [20] to explain the heptamer formation appears to require alternating bonding ($V3-V3= 2.61\text{\AA}$) and anti-bonding ($V3-V3= 3.14\text{\AA}$) trimers

on the kagome plane populated by V3 atoms ($V^{2.5}$; $d^{2.5}$) as proposed in the heptamer structural model.

It is assumed in this picture that the vanadium atoms form the V3-V3 trimers by contributing two electrons to the strong dimer bonds and $\frac{1}{2}$ electron to the inter trimer bonding at the triangular planes formed by V2 (V^{2+} ; d^3) vanadium atoms. Since there are no electrons at the anti-bonding triangles of V3 atoms, the V1 atoms are supposed to be left with two unbound d-electrons. The existence of two different V3-V3 distances seems to be a necessary condition for the 1D orbital wave. Application of non-hydrostatic pressure appears to remove these two different V3-V3 bond lengths in the kagome lattice as shown in Table 3.2. Still the rhombohedral structure is maintained up to 23 GPa, where the onset of the cubic (frustrated) phase starts. It is also to be borne in mind that the bond distance estimations are from non-hydrostatic condition. To make a conclusive statement about bond distances better quality hydrostatic pressure data must be considered for refinement. Further, it can probably be conjectured that there may be a critical range of lattice strain below (high pressure) and above (high temperature) which the delicately balanced orbital overlap must be getting inhibited, destroying the heptamer cluster assembly and driving the system back to frustration. While increase of temperature may weaken the orbital interaction, high pressure may switch on some effective repulsion there by preventing the charge transfer from V3 atoms to the V2 atoms. Structure refinement with better quality data both at high temperature and high pressure on AlV_2O_4 is essential to obtain the bond length, bond angle and atom coordinates that would reveal the mechanism behind the delicate balance between order and frustration in this system.

Summary and conclusions

Powder diffraction experiments under high pressure using diamond anvil cell has been carried out under Non-hydrostatic and hydrostatic conditions.

- AlV_2O_4 transforms from the charge ordered rhombohedral phase at ambient pressure to the charge frustrated cubic spinel phase around (21-23 GPa) on application of pressure.
- AlV_2O_4 is observed to be locked irreversibly in the frustrated cubic phase after decompression from non-hydrostatic pressures. But decompression from hydrostatic pressure reversibly takes the system back to the ordered phase.
- The heptamer model proposed in the literature invokes overlap of vanadium orbitals for the formation of charge ordered clusters. This clusters form with a slight readjustment of the position of vanadium in the parent cubic phase. Such a readjustment is reversed on application of pressure, resulting in the modification of orbital overlap and retention of frustration.
- Further, it may be conjectured that there exists a critical range of strain for the planes involving the kagome` lattice of vanadium (V3), beyond which the delicately balanced orbital overlap must be getting inhibited, destroying the heptamer clusters and driving the system back to frustration.

References

- [1] Russel J Hemley and Neil W Ashcroft, *Physics Today* (1998) 26
- [2] arxiv.org/pdf/cond-mat/0410367
- [3] D. P. Kozlenko, L. S. Dubrovinsky, I. N. Goncharenko, B. N. Savenko, V. I. Voronin, E. A. Kiselev, and N. V. Proskurnina, *Phys. Rev.B* **75** (2007)104408
- [4] O. Mishima, L. D. Calvert, E. Whalley, *Nature*, **310** (1984) 393–395

- [5] Akira Kuriki, Yutaka Moritomo, Yasuo Ohishi, Kenichi Kato, Eiji Nishibori, Masaki Takata, Makoto Sakata, Noriaki Hamada, Sakae Todo, Nobuo Mori, Osamu Shimomura and Arao Nakamura, *J. Phys. Soc. of Japan*, **71** (2002) 3092
- [6] J. Spalek, A. Kozłowski, Z. Tarnawski, Z. Kałol, Y. Fukami, F. Ono, R. Zach, L. J. Spalek, and J. M. Honig, *Phys. Rev. B*, **78** (2008) 100401R
- [7] Yang Ding, Daniel Haskel, Sergei G. Ovchinnikov, Yuan-Chieh Tseng, Yuri S. Orlov, Jonathan C. Lang and Ho-kwang Mao, *Phys. Rev. Lett.* **100** (2008) 045508
- [8] A. Paolone, A. Sacchetti, P. Postorino, R. Cantelli, A. Congeduti, G. Rousse, C. Masquelier, *Solid State Ionics* **176** (2005) 635
- [9] J. Darul, W. Nowicki, C. Lathe, P. Piszora, *Radiation Physics and Chemistry* **80** (2011) 1014
- [10] Yu Lin, Yuan Yang, Hongwei Ma, Yi Cui and Wendy L. Mao, *The J. Phys. Chem.*, **115** (2011) 9844
- [11] G. Oomi, T. Khgayama, I. Yoshida, T. Hagino, S. Nagata, *Journal of Magnetism and Magnetic Materials* **140-144** (1995) 157
- [12] Alka B. Garg, V. Vijayakumar, B.K. Godwal, A. Choudhury, Hans D. Hochheimer, *Solid State Communications* **142** (2007) 369
- [13] P. Vinet, J. Ferrante, J. H. Rose, J. R. Smith, *Journal of Geophysical Research: Solid Earth* **92**, **B9** (1987) 9319
- [14] J. Yan, J. Knight, M. Kunz, S.V. Raju, B. Chen, A. E. Gleason, B. K. Godwal, Z. Geballe, R. Jeanloz and S. M. Clark, *J. Phys. Chem. Solids* **71** (2010) 1179
- [15] A. P. Hammersley, S. O. Svensson, M. Hanfland, A. N. Fitch, and D. Häusermann, *High Press. Res.* **14** (1996) 235
- [16] A.C. Larson and R.B. Von Dreele, "General Structure Analysis System (GSAS)", Los Alamos National Laboratory Report LAUR 86-748 (1994)
- [17] B. H. Toby, EXPGUI, a graphical user interface for GSAS, *J. Appl. Cryst.* **34** (2001) 210
- [18] Y. Horibe, M. Shingu, K. Kurushima, H. Ishibashi, N. Ikeda, K. Kato, Y. Motome, N. Furukawa, S. Mori and T. Katsufuji, *Phys. Rev. Lett.*, **96** (2006) 086406 D.
- [19] Errandonea, S. Ravhi Kumar, F. J. Manjon, V. V. Ursaki and E.V. Rusu, *Phys. Rev. B* **79** (2009) 024103
- [20] Croft M, Kiryukhin V, Horibe Y and Cheong S-W, *New J. Physics* **9** (2007) 86
- [21] K. Matsuno, T. Katsufuji, S. Mori, M. Nohara, A. Machida, Y. Moritomo, Kato, E. Nishibori, M. Takata, M. Sakata, K. Kitazawa and H. Takagi, *Phys. Rev. Lett.*, **90** (2003) 096404
- [22] Y. Horibe, K. Kurushima, S. Mori, T. Asada, Y. Koyama, M. Shingu T. Katsufuji, *Phys. Rev. B* **71**(2005) 052411
- [23] Momma K and Izumi F, VESTA 3 for three-dimensional visualization of crystal, Volumetric and morphology data *J. Appl. Crystallogr.* **44** (2011) 1272

CHAPTER 4

Valence state, hybridization and electronic band structure in the charge ordered AlV_2O_4

In this chapter, the analysis and the results of the Electron Energy Loss spectroscopic (EELS) studies and band structure calculations using WIEN2K code are presented. These studies probe the valence state, hybridization and the electronic band structure of AlV_2O_4 . The chapter is organized into the following sections: Section 1 starts with an introduction to the details of charge ordering in AlV_2O_4 , Section 2 describes hybridization in the octahedrally co-ordinated vanadium, the details of the EELS measurements and the results obtained. Section 3 deals with the aspects of the band structure calculations carried out on the parent, charge frustrated cubic phase and the charge ordered rhombohedral phase of AlV_2O_4 and compares the results obtained. The chapter ends with the summary of results and conclusions.

4.1 Details of the charge ordered structure of AlV_2O_4

AlV_2O_4 is a unique material among the frustrated spinel systems. For temperatures above 700 K, AlV_2O_4 remains in the cubic spinel structure ($Fd-3m$). In this structure, the aluminum ions occupy the tetrahedrally coordinated A-lattice and vanadium ions occupy the octahedrally coordinated B-lattice. Under an ionic bonding scenario, charge neutrality requires vanadium ions to have an average valency of 2.5. Thus vanadium ions with valency 2^+ and 3^+ are distributed on the pyrochlore lattice, resulting in charge frustration. Below 700 K, the charge frustration is relieved through a transition

to the rhombohedral structure ($R\bar{3}m$). The vanadium ions reorganize and form a heptamer cluster along with a lone vanadium.

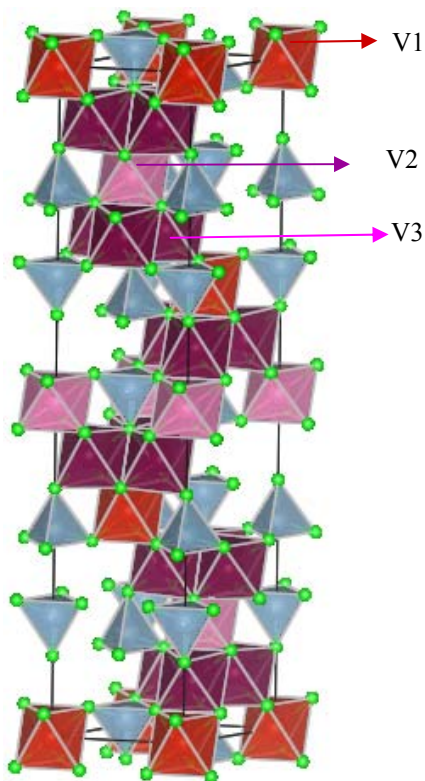


Figure 4.1. Structure of rhombohedral AlV_2O_4 in the hexagonal setting. *V1* atoms are represented by red, *V2* atoms by pink and *V3* by dark brown octahedra, aluminum atoms are surrounded by light blue tetrahedral and oxygen atoms are shown in green. Notice the presence of vanadium heptamers.

In this structural model [1], two types of vanadium ions (*V2* and *V3*) form the heptamer and the third vanadium denoted as *V1* forms the loner. *V1* ions in their octahedral oxygen cage are not bonded with the *V2* and *V3* ions which are arranged in the alternating layers of the triangular and kagomé planes. Figure 4.1 shows the structural model of AlV_2O_4 clearly showing the three different vanadium sites. The stacking of vanadium layers is found to follow the pattern of $V1-V2-V3-V2-V1\dots$ It is argued [1] that the charge state of *V1* is 3^+ based on the *V1*-O distance (2.0439 Å) (close to $V^{3+} - O^{2-}$

in V_2O_3). V2 and V3 are assigned a charge state of 2^+ and 2.5^+ . But first principle DFT calculations [2] have indicated an oxidation state of $2.5-\delta_1$, $2.5+\delta_2$ and $2.5+ (\delta_1-\delta_2)/6$ ($\delta_1 > \delta_2 > 0$) on V1, V2 and V3 respectively. The charge on Al remains the same in the cubic and in the rhombohedral phases. Very recently, EELS on AlV_2O_4 [3] has estimated the average value of charge on vanadium to be 2.5^+ , but no further detailed analysis of the EELS spectrum is available. Thus presently, there appears to be convergence about the heptamer structural model, but consensus is yet to emerge on the assignment of charges on vanadium.

4.2 Vanadium Orbitals and Electron Energy Loss Spectroscopy

4.2.1 Hybridization of vanadium–oxygen orbitals in AlV_2O_4

In general in any correlated electron system with transition metal, the basic property of the system is decided by the transition metal d-electrons. The electronic configuration of vanadium is: $[Ar] 3d^3 4s^2$. When it assumes a charge state of 2^+ , there are 3 electrons (d^3) in the 3d orbital and when its charge state is 3^+ , it has 2 d electrons (d^2) in the 3d orbital. When the transition metal, namely vanadium in the present case, is situated in the octahedral cage of oxygen, the 3d orbitals of vanadium split into $3t_{2g}$ (d_{xy} , d_{yz} and d_{zx}) and $2e_g$ ($d_{x^2-y^2}$ and d_z^2) orbitals (crystal field splitting). In the octahedral environment of oxygen, there is bound to be hybridization of vanadium and oxygen orbitals. The t_{2g} states indeed hybridize to form the π^* anti bonding states and the e_g states hybridize to form the σ^* anti-bonding states. In the specific case of AlV_2O_4 , where all the three vanadium (V1, V2, V3) ions are situated in the octahedral cage of oxygen, the overlap of the oxygen $2p$ and vanadium $3d$ orbitals result in a set of bonding and anti bonding orbitals. Looking at the oxidation state of vanadium, it varies between 2 and 3.

The anti bonding unoccupied states are the π^* - t_{2g} and σ^* - e_g states with the e_g triplet states higher in energy as compared to the t_{2g} doublet. Similarly the 4s a_{1g} state and 4p t_{1u} orbitals hybridize, to form σ^* anti bonding states. All these aspects become apparent from the energy level schematic presented in figure 4.2.

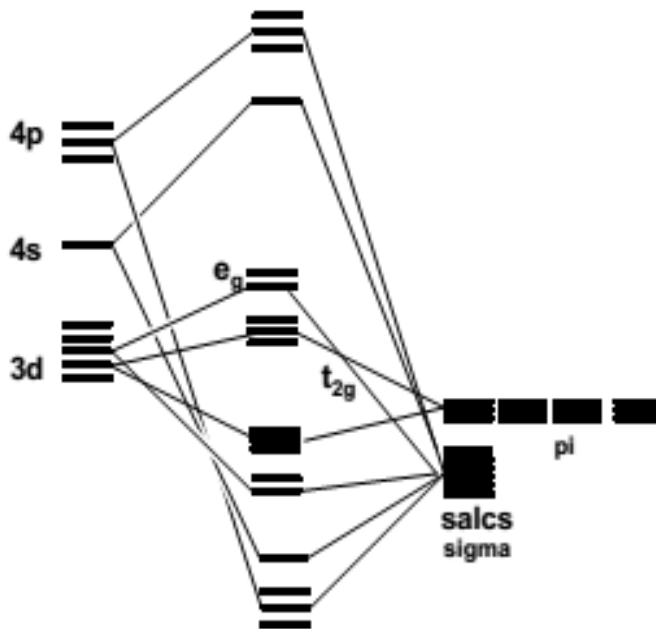


Figure 4.2. Schematic of energy level structure of transition metal in the octahedral coordination of oxygen

Core electron spectroscopy is one of the ways to probe the occupancy or the vacancy of these hybridized states. Either X-ray Absorption Fine structure (EXAFS) techniques or X-ray photo electron spectroscopic (XPS) techniques can be used to probe the un-occupied or the occupied states, respectively. Of late, EELS that is available as an option in high resolution transmission electron microscopes (HR-TEM) is increasingly replacing EXAFS in probing the unoccupied states. EELS is a technique, in which the change in kinetic energy of the incident electrons is measured after they have interacted

with the specimen. It is widely used to analyze the occupancy of the hybridized transition metal-3*d* and ligand-2*p* states.

4.2.2 Electron energy loss spectroscopy - Technique

The EELS as a technique, basically measures the energy loss suffered by an initially mono energetic beam of electrons, after the beam has interacted with a specimen. While reflection energy loss spectroscopy requires incident energies of ~ 30 eV, transmission electron energy loss spectroscopy requires energies more than 100 eV or greater. In the latter mode, if the specimen thickness is below 100 nm, practically all the electrons are transmitted and as they move in the specimen they interact with it. This necessitates focusing of the electrons over a very small area.

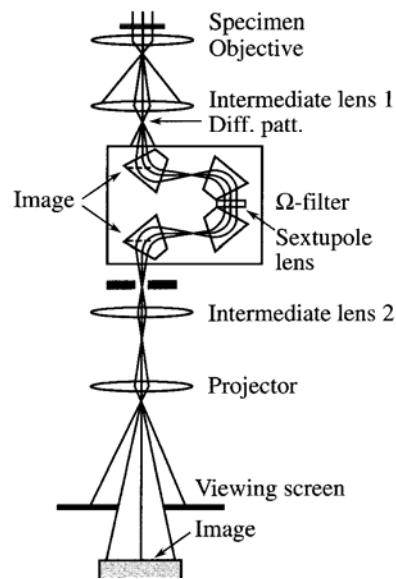


Figure 4.3 Schematic of the EELS attachment in TEM [4]

EELS spectra for the present work are collected using LIBRA 200 FE HRTEM, a high resolution transmission electron microscope (HRTEM) operated at 200 kV, equipped with an in-column energy filter. The schematic of the method used in the LIBRA-200 FE is shown in

figure 4.3. In this scheme the image stability is retained by preserving the vertical column of the microscope. This is achieved by introducing four magnets arranged in the form of Ω and hence it is also called an ‘omega filter’. The beam coming out of the omega filter is highly monochromatic and also maintains the original spot size without loss of brightness. The energy resolution is about 0.7 eV and spatial resolution is better than 0.14 nm.

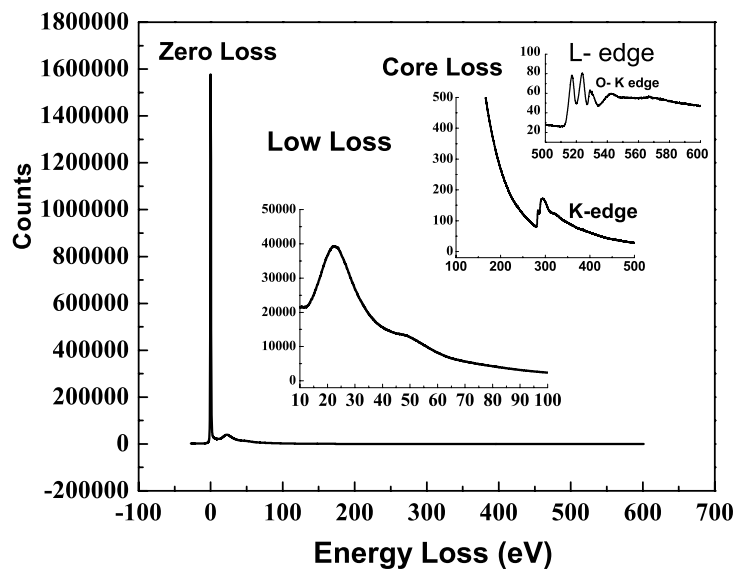


Figure 4.4 Typical EELS spectrum of commercial V_2O_5 . The layers represent different energy loss regions depicting different processes as explained in the text.

In fact, the fast incident electrons interact with the core or valence electrons and they undergo an inelastic scattering resulting in the production of ‘core hole’ or interband transitions or plasmon excitation. In each of these processes the incoming electron loses energy. Thus, a typical EELS spectrum, as shown in figure 4.4 obtained from any specimen is a store house of information about the processes taking place in the specimen.

For the sake of analysis, the complete spectrum can be divided into four different regions. The first one being the highest intensity zero loss peak. The other regions are buried underneath and in fact ride over the back ground of the zero loss peak, causing the background fitting, a difficult process during data analysis.

Closely following the direct, loss less or ‘Zero loss’ peak, is the low loss region, basically accounting for the loss suffered by the incident electron beam in displacing the valence electrons due to coulomb interaction. This process is restricted to less than 100 eV. Analysis of the spectrum within this region yields rich information about the optical properties of the material, plasmon oscillations and interband transition depending on the nature of the material. Plasmons are collective excitations of valence electrons with lifetime of 10^{-15} s and are localized to within <10 nm. The region above 100 eV, loss is very typically characteristic of the atom in question as it explains the dislodging of ‘core electrons’. So the energy loss region beyond 100 eV is called ‘core loss’ region. The electron energy loss intensity in this region is given by ‘Fermi Golden rule’ as,

$$J_c(E) \propto d\sigma/dE \propto M(E)^2 N(E) \propto (df/dE)N(E)$$

where, $d\sigma/dE$ is the differential scattering cross section, $M(E)$ is the atomic matrix element, (df/dE) is the generalized oscillator strength, $N(E)$ is the density of final states in the transition. $N(E)$ here represents the localized density of states, symmetry projected and governed by the selection rule. Thus the excitation of K-shells give information about the density of empty p states and the excitation of L shell give information about density of 3d states. Thus with appropriate handling of the background a wealth of information can be obtained from a typical EELS spectrum.

4.2.3. Electron energy Loss spectroscopy studies on AlV_2O_4 and other vanadium oxides

4.2.3.1 EELS spectrum of the charge ordered AlV_2O_4

In the present work, detailed EELS measurements have been carried out to probe the unoccupied, hybridized V-3d and O-2p states in AlV_2O_4 . Vanadium forms a variety of oxides. Typically V_2O_5 , VO_2 , V_2O_3 are the commonly known oxides in which the oxidation state of vanadium is 5^+ , 4^+ and 3^+ , respectively .

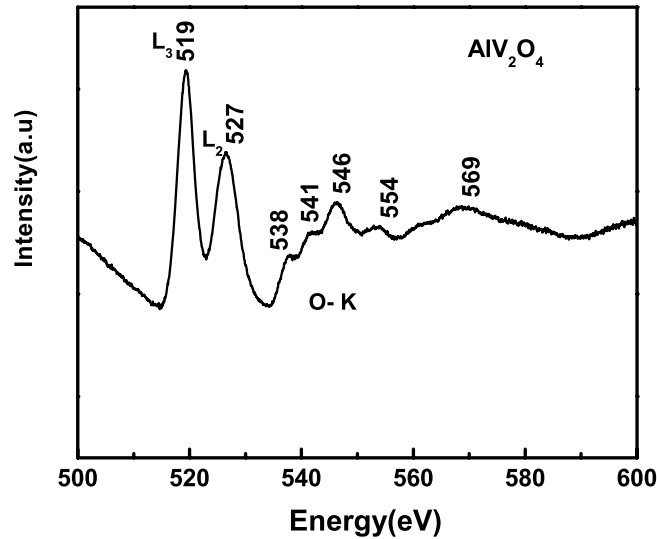


Figure 4.5. Electron Energy Loss spectrum of AlV_2O_4 Note: Oxygen K-edge starts at 538 eV immediately after the L_2 -edge of Vanadium at 527 eV

In each of them the vanadium ion is situated in the octahedral cage of oxygen atoms. Therefore, the EELS spectra of AlV_2O_4 (synthesized) and the other oxides of vanadium (commercially procured; Alfa Aesar; High purity; > 99.9%) are obtained. The full range of EELS spectrum has been obtained with zero correction. As the present interest is on the L-edge of vanadium and K-edge of oxygen, the data from 500 to 600 eV is considered for analysis. Basically, the L-edge corresponds to transitions from

vanadium $2p_{3/2} \rightarrow 3d$ (L_3) and $2p_{1/2} \rightarrow 3d$ (L_2). Taking this into consideration, the L_3 and L_2 peak would correspond to transitions to e_g and t_{2g} states. The oxygen K edges correspond to transitions from, O-1s to hybridized $^2t_{2g}$, 3e_g , $^3a_{1g}$ and $^4t_{1g}$. Figure 4.5 shows the EELS spectrum obtained for the charge ordered AlV_2O_4 in the energy range 500-600 eV. As mentioned above, this energy range includes the vanadium L- edges (white lines) and the O-K edges. The background is fitted to a power law [5-6]. Peak positions are estimated by fitting the white lines to a Gaussian profile. The vanadium L_3 and L_2 peaks appear at 519 eV and 526 eV. The oxygen K-edges show a characteristic three peak structure with peaks at 538, 541 and 546 eV. These edge values compare well with the earlier observation in [3], where the reported values for the V- L_3 and V- L_2 peaks are at 519 and 527 eV and the O-K edge energies are at 535, 540 and 545 eV. The O-1s to hybridized $^2t_{2g}$ differs by 3 eV. Considering the energy resolution, the difference is significant. Still it is considered acceptable since, arriving at the precise value of the O- K edge is considered difficult for vanadium systems due to the overlap of the vanadium L and oxygen K edges [9]. Further interesting details of the oxygen K-edges are taken up for discussion in the later part of the analysis. In this context, it is very relevant to carefully observe the oxygen K-edges in the case of the other vanadium oxides too. Such a comparative analysis is carried out as a part of this work and presented in the subsequent sections.

4.2.3.2 EELS spectrum of the other vanadium oxides

EELS spectra in the energy range of 500-600 eV for V_2O_5 (a), VO_2 (b), V_2O_3 (c) and AlV_2O_4 (d) are shown in figure 4.6. It can be seen that the L_2 intensity reduces as the oxidation state of vanadium decreases from 5^+ (V_2O_5) to $< 3^+$ in AlV_2O_4 . The oxygen K

edges namely, O-1s to hybridized $2t_{2g}$ (P), O-1s to hybridized $3e_g$ (Q), O-1s to hybridized $3a_{1g}$ (R) and O-1s to hybridized $4t_{1g}$ (S) are also indicated in the figure. A comparative analysis of all these spectra have been carried out by considering three aspects namely, the white line ratio, shift in the onset of L-edge and details of O-K edge.

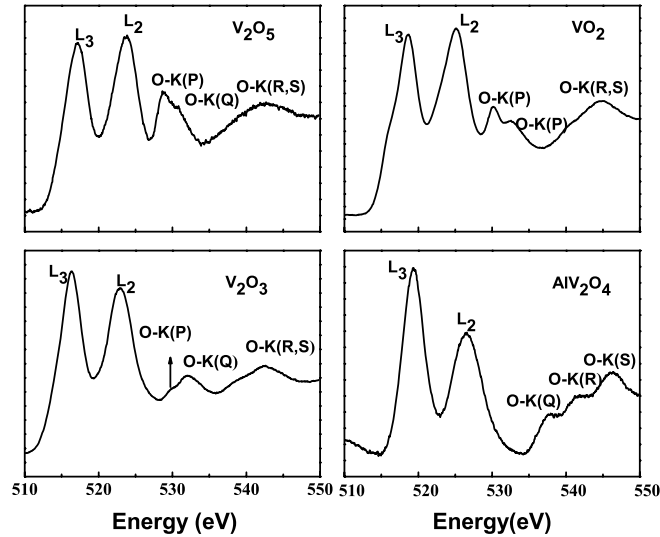


Figure 4.6 EELS spectra for V_2O_5 , VO_2 , V_2O_3 and AlV_2O_4 in the energy range corresponding to the $L_{2,3}$ edge and O-K edges

4.2.3.3. The white line ratio

Since the e_g states are unoccupied in the case of vanadium, the intensity of the L_2 peak remains unchanged, but depending on the oxidation state of the vanadium in the various oxides, the occupancy of the t_{2g} states change. This is reflected in the ‘White Line’ ratio defined as the intensity ratio L_2/L_3 . A lot of work exists in the literature, which compare the ratio of the L_3 and L_2 lines and the oxidation state of transition metal oxides [5-9]. It is also seen in the literature that the reduction in L_2/L_3 ratio in the case of

vanadium oxides of lower valency is attributed to the reduction in the number of unoccupied t_{2g} states [5].

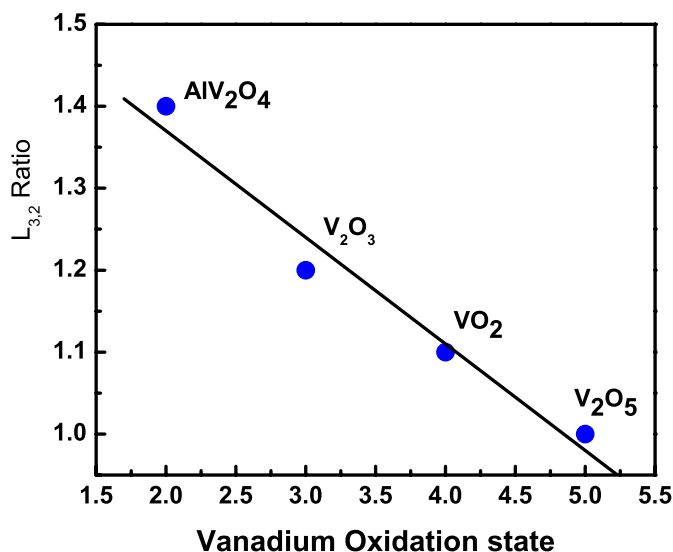


Figure 4.7 $L_{3,2}$ ratio versus vanadium oxidation state

In order to compare the ratios across the various oxides of vanadium, the following procedure as suggested in the literature is followed: For all the spectra the background is fitted to a power law [4-5]. The L_3 and L_2 intensity ratios (white line ratio) are obtained after fitting the peaks to a Gaussian profile. Figure 4.7 shows the variation of L_3/L_2 ratio as a function of the oxidation state of vanadium. The L_3/L_2 ratio seems to follow a linear relation for the three oxides of vanadium. As seen from the spectrum itself, the reduction in intensity appears to be much more in the case of AlV_2O_4 . The data points could be fitted better to a linear relation if an oxidation state of 2^+ is assumed for V rather than 2.5^+ . A similar linear relationship between oxidation state and L_3/L_2 ratio has been seen in Mn [7] and across the transition metal series [6]. While determining L_3/L_2 ratio from

the EELS spectra of transition metal oxides, Fourier ratio deconvolution of the data is stressed [8], to remove the multiple scattering due to the sample thickness effect. This requires about 40 eV tail beyond L_2 . But in the case of vanadium oxides, since vanadium $L_{2,3}$ edges are immediately followed by the O-K edges, such rigorous fitting procedure to cull out the white line ratio, generally employed for other transition metal oxides, becomes inapplicable. So in the present study, the white line ratio analysis can only qualitatively indicate that the occupancy of t_{2g} states of vanadium progressively increases as one goes from V_2O_5 to AlV_2O_4 .

4.2.3.4. The shift in excitation edge

It has been observed in the case of transition metals that the K or L excitation edge shifts to a lower energy if the oxidation state is lower. This fact is used to determine the oxidation state of the system under consideration. In the present case, the L excitation energy of all the four compounds have been obtained by considering the edge at 10% fall of the maximum. This convention is followed to account for weak pre-peaks if any and also the noise [10]. The obtained edge onset (E) for the three known oxides are fitted to an empirical linear relation $E=a_1.V_{ox}+a_2$ as shown in figure 4.8 ,where V_{ox} is the oxidation state and a_1 and a_2 are obtained to be 2.5 and 510 eV respectively. Using these constants and the measured chemical shift, one can estimate an average oxidation state of 2.4 for V in AlV_2O_4 . This value is closer to the average charge on the V ions.

Such an extracted value has to be taken cautiously when dealing with charge ordered compounds like AlV_2O_4 . In a charge ordered compound there is continuous variation of charges in the space rather than an average charge of say 2.5 on each of the vanadium ions. Apart from the vanadium edges, the oxygen K-edge also can be studied to get the

charge state information. The following section presents the information obtained from such an analysis.

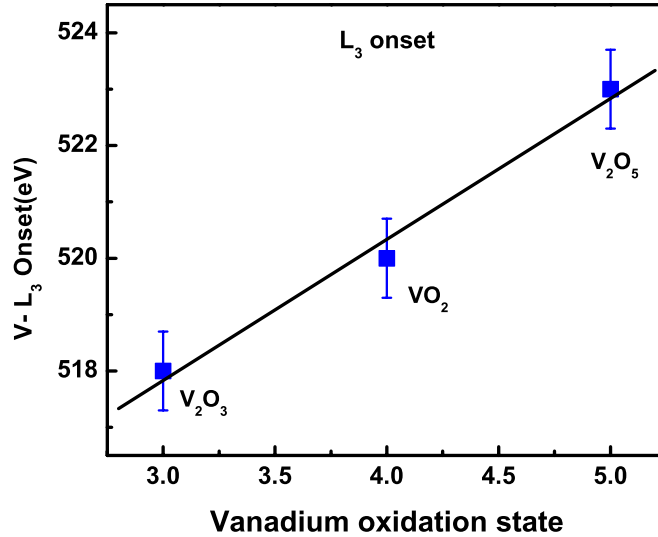


Figure 4.8 Vanadium L_3 edge onset versus oxidation state. Squares represent the experimentally measured chemical shift. Solid line shows the fit to $E = a_1 V_{ox} + a_2$.

4.2.3.5. Comparison of oxygen K- edge

Closely following the white lines of vanadium, the O-K edge features are seen in the EELS spectrum up to about 15 eV. Four such transitions, namely, O-1s to hybridized $2t_{2g}$ (P), O-1s to hybridized $3e_g$ (Q), O-1s to hybridized $3a_{1g}$ (R) and O-1s to hybridized $4t_{1g}$ (S) can be anticipated [11]. In the present case of V₂O₅, VO₂, V₂O₃ and AlV₂O₄, the energy loss features within the 5 eV range are assigned to $2t_{2g}$ and $3e_g$ transitions and those beyond are assigned to $3a_{1g}$ and $4t_{1g}$ transitions. Table 4.1 summarizes the observed positions of the four O-K edges. Focusing on the oxygen K-edge features in figure 4.6, and the oxygen K-edge energies listed in the table 4.1, it can be observed that as one goes

from V_2O_5 to V_2O_3 , the intensity of the peak P decreases, which brings out the reduction in unoccupied hybridization states.

Table 4.1 O-K edge for V_2O_5 , VO_2 , V_2O_3 and AlV_2O_4 from this work and also from [3]

| Compound | Valency | d-count | O-1s to $2t_{2g}$ (eV) | O-1s to $3e_g$ (eV) | O-1s to $3a_{1g}$ (eV) | O-1s to $4t_{1g}$ (eV) |
|---------------------------|---------|---------|------------------------|---------------------|------------------------|------------------------|
| V_2O_5 | 5+ | 0 | 529 | 531 | 543 | |
| VO_2 | 4+ | 1 | 530 | 533 | 540 | 545 |
| V_2O_3 | 3+ | 2 | 530 | 532 | 538 | 542 |
| AlV_2O_4 (this work) | | | | 537 | 540 | 546 |
| AlV_2O_4 Ref. [3] | | | | 535 | 540 | 546 |

Since the hybridized e_g states remain unoccupied across these oxides, these transitions are unhindered. In the case of AlV_2O_4 , surprisingly, the O-K edge corresponding to the transition from 1s to $2t_{2g}$ is totally absent. The absence of the first pre-peak (P) clearly indicates that, V-3d $2t_{2g}$ state is occupied either partially or fully and not available for transition. The absence of this transition is also evident from the EELS spectrum of an earlier measurement [3]. The authors have not gone into the details of this observation. But placing AlV_2O_4 amidst the other oxides of vanadium and observing the systematic reduction of intensity, clearly leads to the interpretation that the oxidation state of all vanadium ions, whether on the triangular or on the kagomè lattice, probably is less than 3^+ . This aspect is further discussed at the end of this chapter.

4.3 Band structure calculation

It is well known that accurate theoretical description of the electronic structure is a formidable task when it comes to describing electronic structure of correlated electron

systems. In general, two approaches are followed to reach to a meaningful calculation. One method is to extend the density functional formalism using local density approximation (DFT-LDA) and the other way is to use a highly simplified model. The dynamical mean field theory (DMFT) belongs to the latter and has been successful in describing simple Mott insulators. The difficulty with complex systems in the model based approach is that it is not *ab-initio*, but requires initial inputs to be adjusted. For the calculation of total energy and bulk properties of the system, the DFT-LDA still gives good estimates and hence has been used in the present thesis. In the DFT-LDA as used in the WIEN 2K package, initially a guess value of the electron density $\rho(\mathbf{r})$ is considered and the effective potential is calculated. With this effective potential and the initial density, the Kohn-Sham equations are solved to obtain the orbitals. This is used to evaluate the electron density and calculate the total energy of the system. With the inclusion of a convergence criterion, the process is repeated iteratively to ultimately obtain a convergence in the electron density distribution and total energy of the system.

4.3.1 Parameterization of the electronic structure calculation on AlV_2O_4

ab-initio electronic structure calculation within the density functional formalism is carried out for the charge ordered rhombohedral phase and the charge frustrated cubic spinel phase of AlV_2O_4 . Such a calculation enables further information about the density of states, energy dispersion and also to estimate relevant bulk properties from the total energy. For calculating the properties of AlV_2O_4 in both the rhombohedral ($R\bar{3}m$, 166) and cubic spinel ($Fd\bar{3}m$, 227, 2nd setting) structure, the full potential linearized augmented plane wave (FP-LAPW) method has been used, as implemented in the all-electron WIEN2k [12] code. Wu-Cohen [13] flavor of generalized gradient

approximation (GGA) is used for estimating the exchange and correlation functional. This code assumes a Muffin-Tin (MT) model for the crystal potential. The electrons are divided into two groups: electrons whose charge densities are confined within the muffin-tin spheres and outside it, respectively. In these two regions, different basis sets are used to expand the wave function, charge density and the potential function. Inside the non-overlapping spheres of radius R_{MT} (1.49 a.u. for Al, 1.95 a.u. for V and 1.77 a.u. for O in rhombohedral structure, and 1.54 a.u. for Al, 2.07 a.u. for V and 1.87 a.u. for O in cubic spinel structure) around each atom, a linear combination of the product of the radial solutions of the Schrödinger equation and the spherical harmonics are used, while the plane wave basis set is used for the valence electrons. The maximum value of angular momentum $\ell_{max} = 10$ is taken for the wave function expansion inside the atomic spheres. For plane wave expansion of the electronic wave function in the valence region, a plane wave cut-off value of $R_{MT} * K_{max} = 10$ is used for all the calculations and $g_{max} = 12$ is maintained. A mesh of $12 \times 12 \times 12$ k-points is considered for the Brillouin zone integration for the rhombohedral structure, while a $19 \times 19 \times 19$ k-point mesh is used for the cubic spinel structure. Total energy convergence is checked with respect to the plane wave cut-off as well as the number of k-points. Convergences in the self-consistent field cycle are better than 10^{-7} Rydberg for total energy and 10^{-7} a.u. for core charge displacement and 1 mRyd/a.u. for the inter-atomic forces. In WIEN2k, considering the rhombohedral structure of AlV_2O_4 , the lattice parameters are specified in the hexagonal setting ($\mathbf{a}_H = \mathbf{a}_R - \mathbf{b}_R$, $\mathbf{b}_H = \mathbf{b}_R - \mathbf{c}_R$ and $\mathbf{c}_H = \mathbf{a}_R + \mathbf{b}_R + \mathbf{c}_R$, so that $a_H = b_H = 2a_R \sin \alpha / 2$ and $c_H = a_R \sqrt{3 + 6 \cos \alpha}$), while the atom positions are given in the rhombohedral setting.

Figure 4.9 shows the structure model considered for computation. The relationship with the hexagonal unit cell which is three times the rhombohedral volume is also shown.

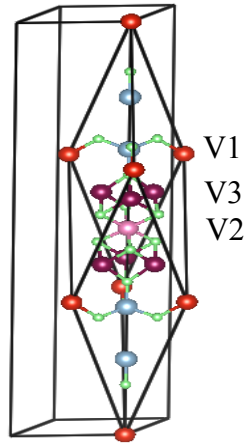


Figure 4.9 Rhombohedral structural model of AlV_2O_4 showing the heptamer formed by V_2 sandwiched between two V_3 trimers and the lone V_1 . Green spheres denote oxygen and light blue denotes aluminum.

For obtaining the minimum energy structural configuration, optimization of the a_H and c_H/a_H ratio is carried out and then the atomic positions are relaxed so that the inter-atomic forces between the atoms are less than 5 mRyd./a.u. Imposing moments on vanadium appears to be essential for convergence of lattice parameters. Upon convergence the lattice parameter in the charge ordered state is found to be: $a = 10.089 \text{ \AA}$ and $\alpha = 32.83^\circ$ and cell volume = 268.585 \AA^3 . This agrees well with the lattice parameter obtained from Rietveld refinement carried out as part of this thesis work (Chapter 3) of the powder diffraction data and also with the data from the literature[1,2]. In the cubic spinel structure, optimization of a_{cubic} followed by the atomic position relaxation is carried out. It is observed that the spin-polarized calculations are necessary to obtain lattice parameters that are near to the experimentally observed values. Once the ground state

configurations are obtained, other properties such as the band structure, density of states and the electronic density distribution are calculated.

4.3.2 Band structure of the rhombohedral and cubic phase of AlV_2O_4

The spin polarized band structures for the charge ordered rhombohedral phase (a) and the charge disordered cubic phase (b) are shown in figure 4.10. It is seen that the cubic phase shows half-metallic behavior, as there are bands crossing the Fermi energy in the spin up channel. This compensates the large gap observed in the spin down channel. There is no such band crossing observed in the rhombohedral phase and it shows a band gap of ~ 0.25 eV. This estimate is in agreement with the calculated value of 0.2 eV by Cai *et al* [2]. Presently there exists only one published work in the literature on the resistivity measurement [14] of AlV_2O_4 . From the data presented in ref. [14] for temperatures between 400 K to 800 K, the gap parameters for the charge ordered rhombohedral phase and the charge frustrated cubic phase are estimated to be 0.388 eV (4500 K) and 0.258 eV (3000 K). This estimate is in agreement with the calculated value of 0.2 eV by Cai *et al*[2]. Presently there exists only one published work in the literature on the resistivity measurement [14] of AlV_2O_4 . From the data presented ref.[14] for temperatures from 400 K to 800 K, the gap parameter is estimated for the charge ordered rhombohedral phase and the charge frustrated cubic phase to be 0.388 eV (4500 K) and 0.258 eV (3000 K).

The resistivity studies [14] and the band structure calculation have shown a semi-conducting behaviour for the charge ordered phase. The discrepancy between the estimated and observed gap values may be attributed to the presence of the Al_2O_3 (gap value of 5 eV) impurity claimed to be present in their sample. Even though low resistivity

path is provided by the majority small gap phase, quantitative estimation of gap has to be taken with caution.

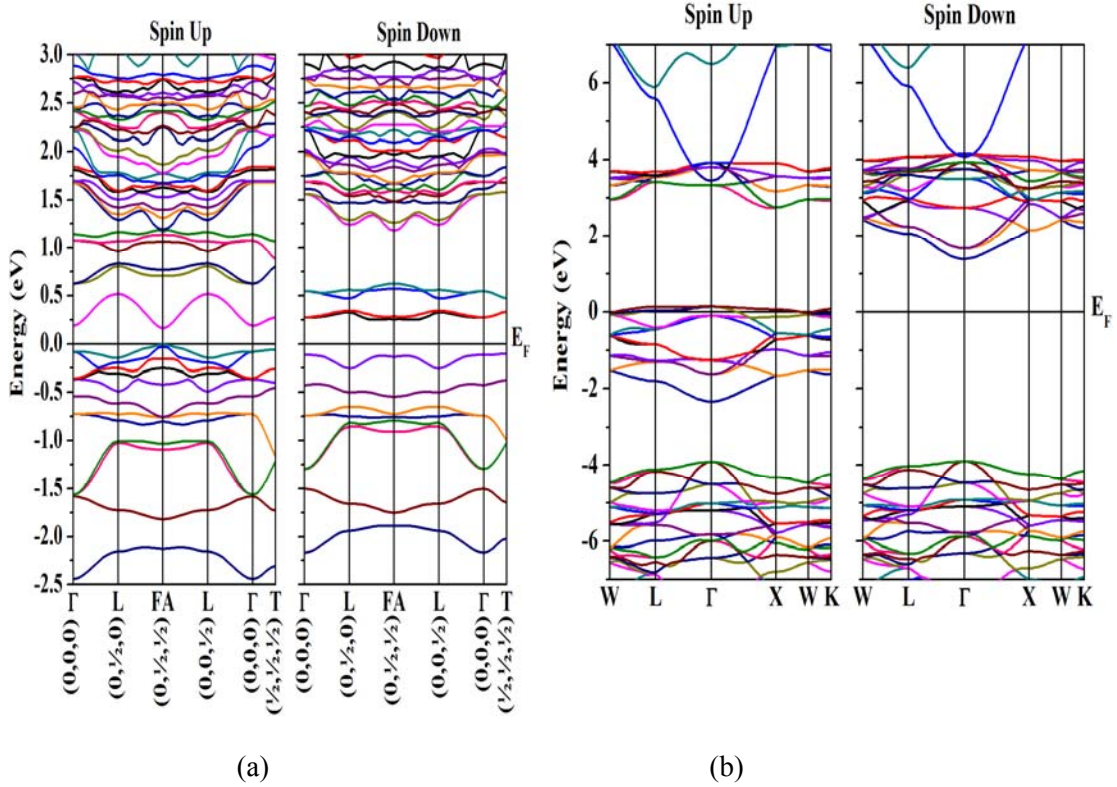


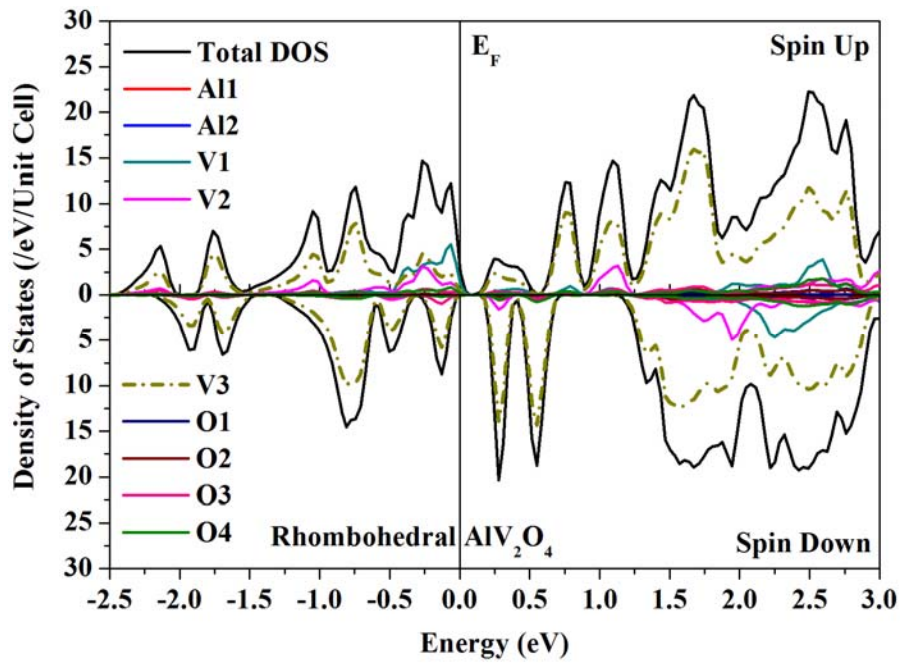
Figure 4.10 Spin polarized band structure of: (a) rhombohedral and (b) cubic AlV_2O_4 . The high symmetry coordinates are also marked in the rhombohedral case in order to conform to the labeling scheme of Cai et al [2].

Experiment has shown a semi conducting behaviour as against the semi metallic behaviour suggested by the DFT calculation for the frustrated cubic phase. Since the parameters of the computation has rightly predicted the existence of insulating phase in the charge ordered situation, it is expected to predict the behavior correctly in the cubic phase, with due concern to the fact that the system under consideration is a strongly correlated system. In the light of availability of only very few experimental studies,

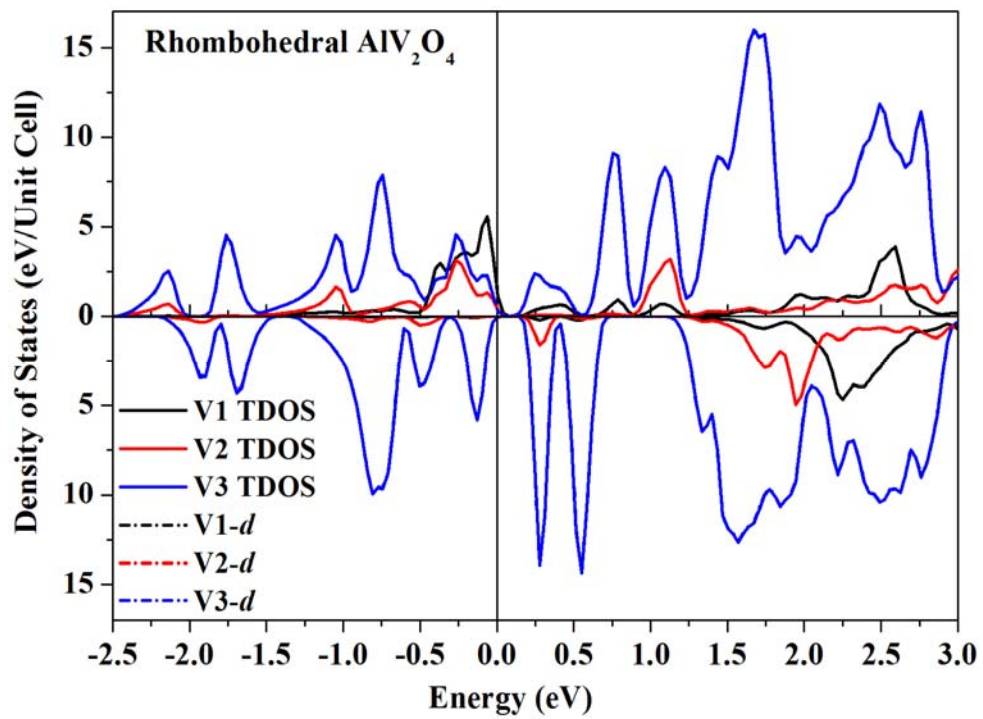
synthesizing single phase AlV_2O_4 is the most important prerequisite before carrying out resistivity measurements.

4.3.3 Density of states of the rhombohedral and cubic phase of AlV_2O_4

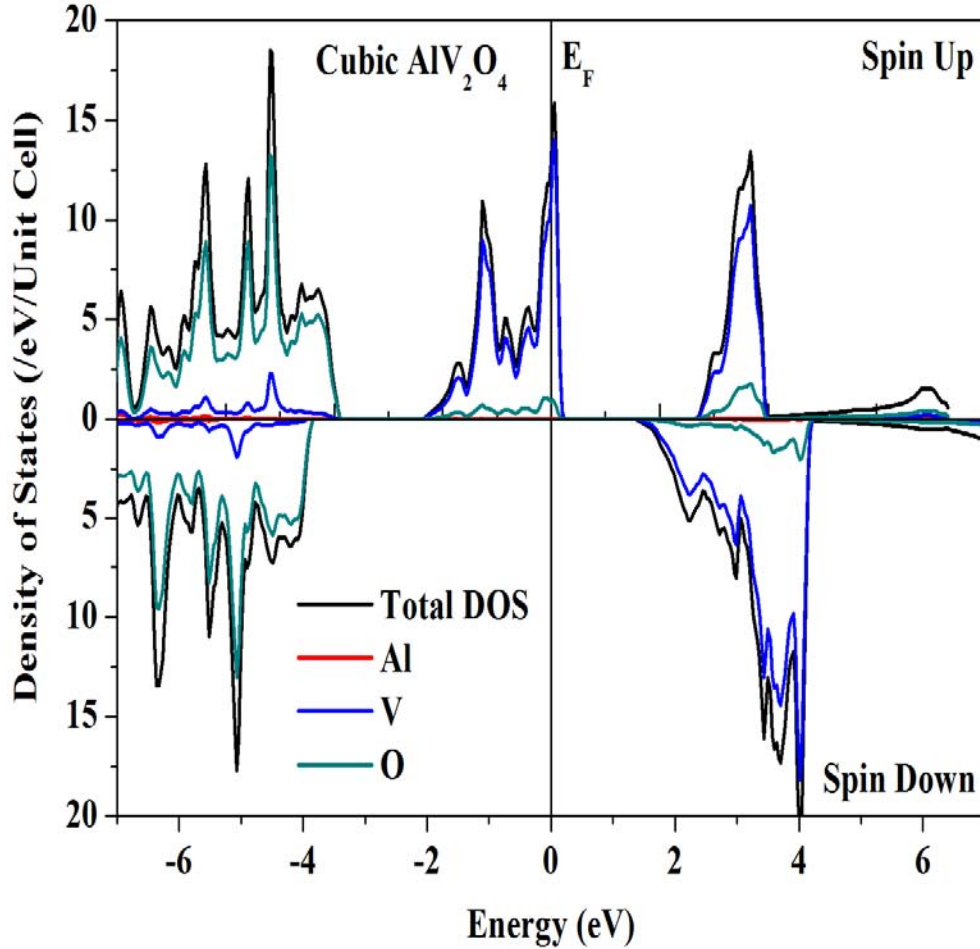
A plot of density of states as a function of energy gives information about the states that contribute at the Fermi energy. From the density of states at the Fermi level, it can be found out that which are the components of the system that contribute towards determining the various properties of the system. The total and $3d$ density of states (DOS) of AlV_2O_4 in the rhombohedral phases is plotted in figure 4.11 (a) and (b). Figure 4.11 (a) shows the contribution from all the atoms namely, Al, V and O at the Fermi level. It is seen that the major contribution comes from vanadium atoms and a small contribution from oxygen can also be observed. Contribution from Al is almost absent. In the case of DOS corresponding to the cubic phase too the major contribution is from vanadium atoms and only a small contribution from O $2p$ levels is seen at the Fermi energy as shown in figure 4.11(c). This clearly indicates that the aluminum and vanadium $4s$ electrons are transferred completely to oxygen such that Al exists as Al^{3+} and O as O^{2-} . From the density of states shown for vanadium (figure 4.11(b)), it is seen that all the vanadium (V1, V2 and V3) contribute to the DOS. This may suggest that V1 is not a non participating loner in the charge ordering process of AlV_2O_4 . This has a consequence with respect to the charge states apportioned on vanadium in the heptamer model as explained in the following section.



4.11 (a)



4.11 (b)



4.11 (c)

Figure 4.11 Calculated total and partial density of states for rhombohedral and cubic AlV_2O_4 . (a) Shows the total and atom decomposed DOS for rhombohedral phase. (b) All the DOS for V atoms is contributed by the V 3d orbitals, as no difference between the total and d orbital contribution can be seen. (c) Total and atom decomposed DOS for the cubic phase. It shows a half-metallic behavior as the spin-up channel is metallic, while the spin-down channel is insulating.

4.3.4 Charge disproportionation in AlV_2O_4

Amongst the known charge ordered spinel compounds, AlV_2O_4 seems to be unique since the charge ordered phase is still not made up of integral charge states. The heptamer model [1], apportions charges as V1 (3^+), V2(2^+) and V3(2.5^+). The reason for the choice of 3^+ charge state seems to have stemmed from the V3-O bond length which is

closer to the one observed in V_2O_3 . To quote from the publication, “It should be noted that the V1-O bond length is 2.043, close to the theoretical value for the $V^{3+}-O^{2-}$ bond, and thus it is reasonable to interpret the ‘left-alone’ V1 ion as trivalent ($3d^2$)”. But surprisingly V2-O bond length is shorter. To examine this point, the bond lengths obtained from Rietveld refinement of the results of the powder XRD data (lab source) from this thesis work, the DFT calculations from this work, refinement of powder XRD [1] and DFT calculations from the literature[2] are presented in table 4.2. From the table, common trends well beyond standard deviations (not shown) can be inferred. Existence of two different V3-V3 bond lengths, a shorter and a longer one on the kagomè plane formed by V3 ions is observed to emerge at the end of refinement of powder data and convergence from the band structure calculations. This seems to be essential for the formation of heptamer and non bonded loner. The oxygen octahedra around V1 and V2 are regular but that around V3 are highly distorted, probably to sustain the heptamer clustering. V2-O bond is shorter than V1-O and also V2-V3 distance is shorter than V1-V3 bond distance. These imply that charge on V2 may not be lesser than that on V1 from purely bond distance considerations.

It is also observed from the bond valence sum estimation from the band structure calculation carried out in the present thesis work, that a charge state of 2.51 for V1, 3.04 for V2 and 2.79 for V3 can be attributed across the relevant V-O bonds. Without stressing too much on the actual numbers, the trend of charge state can be obtained with certainty within the restraints of the band structure calculation. From the calculations, the charge state of vanadium in the rhombohedral phase varies as $V2 > V3 > V1$.

Table 4.2 Summary of structural information on AlV_2O_4 obtained from Rietveld refinement of powder data and DFT computations from the present work and data drawn from references [1] and [2]

| | This work (Expt.) | This work (DFT calc.) | Ref [1] (Expt.) | Ref [2] (Calc.) | |
|-----------------------|-------------------|-----------------------|-----------------|-----------------|-------|
| A (Å) | 10.124 | 10.089 | 10.175 | 10.008 | |
| Alpha(°) | 33.06 | 32.83 | 32.83 | 33.18 | |
| Vol (Å ³) | 274.885 | 268.585 | 267.151 | 275.534 | |
| Bond length(Å) | V1-V3 | 3.004 | 3.01 | 3.039 | 3.021 |
| | V2-V3 | 2.823 | 2.785 | 2.809 | 2.751 |
| | V3-V3 (l) | 3.084 | 3.14 | 3.141 | 3.225 |
| | V3-V3 (s) | 2.677 | 2.588 | 2.610 | 2.489 |
| | V1-O4 | 2.042 | 2.026 | 2.044 | 2.047 |
| | V2-O3 | 2.041 | 2.01 | 2.024 | 2.009 |
| | V3-O1 (V3-O4) | 2.094 | 2.084 | 2.064 | 2.043 |
| | V3-O2 | 2.074 | 2.018 | | |
| | V3-O3 | 2.006 | 2.006 | | |

In addition to that, the observation that O-K edge transitions from O-1s to hybridized $^2t_{2g}$ are totally blocked, one can see that all the vanadium orbitals are probably partially occupied in the charge ordered state. Thus it appears that charge disproportionation is non

trivial in this system and the ordering may be associated with deviation from integral charge state. It remains to be examined as to the detailed nature of orbital organization [15] in the light of the non integral charges on vanadium. It is to be examined what is the effect of this charge state reassessment on the other properties of AlV_2O_4 . Magnetic susceptibility has been measured [1] as a function of temperature down to 4 K. Presently, a $S=1$ state on V1 and a spin singlet on heptamer are invoked, to interpret the observed magnetic susceptibility that follows a Curie-Weiss behavior at T less than 100 K and a combination of Curie-Weiss and a triplet excitation from a singlet state above 100 K. Assumption of charge state of $3+$ (d^2) on V1 aids this interpretation. But with non-integral charge on all vanadium atoms, a different approach may be required to explain the observed magnetic susceptibility. Further detailed measurements, probing the global and local magnetic moments are essential to reach an interpretation involving the partially occupied orbitals. Magnetic resonance inelastic scattering [16-18] experiments on very good quality single phase specimens may enable better understanding of the nature of orbital ordering and occupancy in systems like AlV_2O_4 which are exotic and complex.

4.3.5 Corroboration from band structure calculation for pressure and temperature driven frustration in AlV_2O_4

As pointed out from the experiments carried out on AlV_2O_4 as a function of temperature (Chapter 2) and pressure (Chapter 3), this spinel system is delicately balanced between the charge ordered and frustrated states. Temperatures above 770 K and pressure above 20 GPa drive the system from charge ordered rhombohedral phase to a frustrated cubic phase. To examine this from the first principle approach, total energy

calculations have been carried out with appropriate convergence criterion, for both the charge ordered rhombohedral phase (R-3m) and the charge frustrated cubic phase (Fd-3m) of AlV_2O_4 by varying the volume/formula unit. Figure 4.12 shows the results of the calculation. The experimental initial volumes are shown by filled circles (rhombohedral phase) and filled triangles (cubic phase).

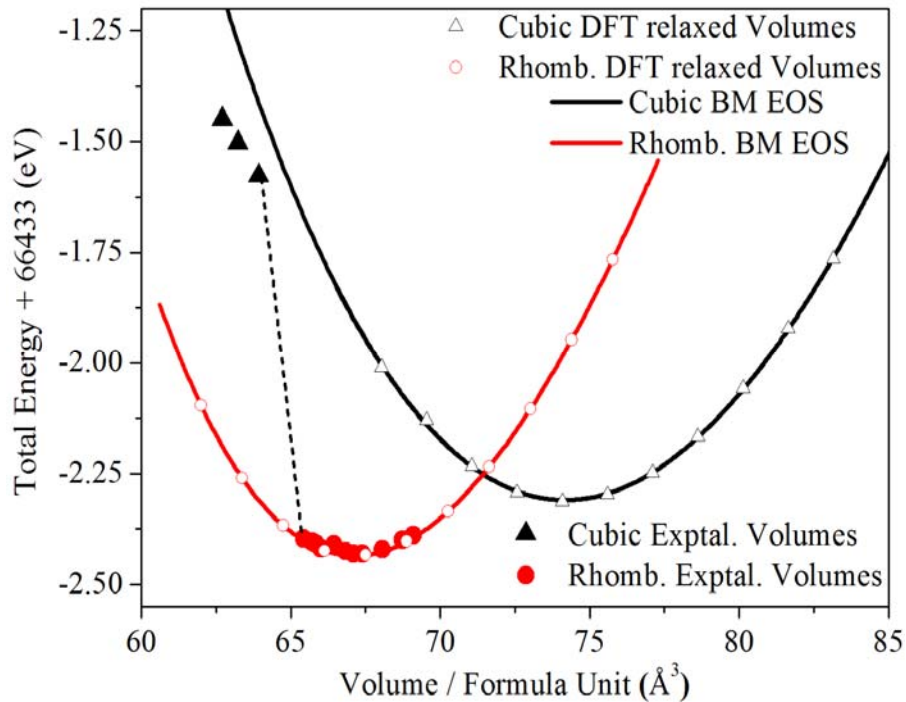


Figure 4.12 Total energy as a function of Volume / Formula unit for AlV_2O_4 . Filled triangles and filled circles represent the experimentally observed volume/FU; open triangle and circles represent relaxed volumes/FU for the cubic and rhombohedral phase. Solid line indicates fit to Birch-Murnaghan equation of state.

Results of the computation are compared with the experimental observations. These values are relaxed to obtain the converged total energy. The relaxed values are shown as open circles (rhombohedral phase) and open triangles (cubic phase). A very good agreement is observed between the experimental and relaxed volumes in the case of

the charge ordered rhombohedral phase. Whereas in the case of the charge frustrated cubic phase, such a good agreement is not observed, between the experimental and relaxed volumes. This is attributed to the uncertainties in the lattice parameter estimation from the broadened diffraction peaks at pressures above 20 GPa. Within this limitation it is seen that the structure is driven to a frustrated state on application of pressure. However, rhombohedral to cubic structural transition is a diffusion less phase transition which involves only a small reorganization of atoms as shown in fig 4.13.

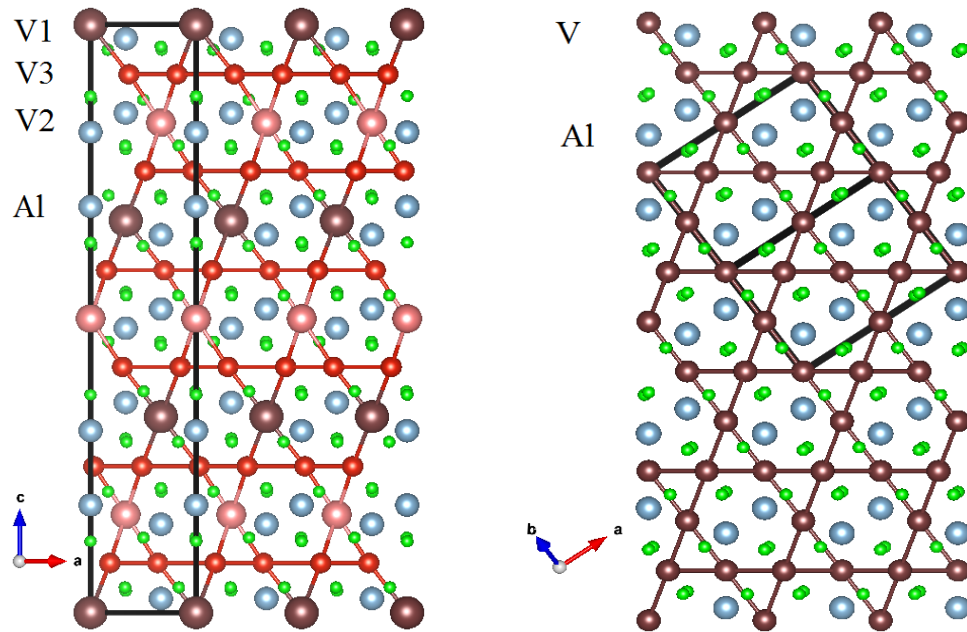


Figure 4.13 Structure of AlV_2O_4 in the relevant directions; (a) Rhombohedral phase in the 0-10 projection with three different vanadium ions; (b) Cubic phase in 0-11 projection

It appears that such reorganization is easily possible when the sample is either heated or it is subjected to high pressure. In fact these two structures are closely related and it is inferred that the (111) distances in the cubic structure and the (001)/2 distances in the rhombohedral structure are the same. From the calculated bond angles and bond

distances for every relaxed volume that represent a unique experimental pressure, this condition is observed to be satisfied. The rhombohedral to cubic transition is seen to occur in high pressure experiments between 21.3 to 24.5 GPa, where $c/2$ in the rhombohedral structure at 21.3 GPa is only 2.6% larger than the (111) body diagonal distance in the cubic phase at 24.5 GPa.

Thus in the case of AlV_2O_4 the geometric frustration inherent to the pyrochlore B sub-lattice is relieved through a gentle orbital ordering leading to a different kind of charge disproportionation which aids the structural transition without involving any major modification in the system.

Summary of results and conclusions

- White line ratio and O-K edges of V_2O_5 , VO_2 , V_2O_3 and AlV_2O_4 obtained using electron energy loss spectroscopy (EELS) are analyzed specifically to probe systematically the VO_6 octahedra in all of them.
- The systematic decrease of the L_2 intensity and the O-K edge intensity from V^{5+} in V_2O_5 to AlV_2O_4 indicates a progressive increase in the occupancy of the hybridized states.
- The absence of transition from O-1s to hybridized $2t_{2g}$ indicates partial filling of all the vanadium orbitals. This would mean vanadium in the charge ordered rhombohedral phase can have charge states lower than 3 only.
- Band structure calculations carried out on the frustrated cubic and the charge ordered rhombohedral phase clearly bring out opening of a gap in the charge ordered phase and a semi metallic state in the cubic phase.

- Density of states of V3 ions forming the kagomé plane seems to have a prominent contribution at the Fermi energy. However, contributions from all the V1, V2 and V3 are present.
- From the structural information available from literature and also obtained from this work, and from the absence of O-K edge from (1s to $\pi^* 2t_{2g}$) EELS, it appears that the charge state on all vanadium may be deviating from integral values indicating probably a partial orbital occupancy and non trivial ordering.
- The bond valence sum estimation from the band structure calculation and the charge state of V in the rhombohedral phase must be $V2 > V3 > V1$. This is different from the values mentioned in the earlier work. Hence, though the charge ordered rhombohedral phase may be formed by the clustering of vanadium largely due to direct vanadium-vanadium as heptamer unit, charge state on vanadium atoms needs detailed reassessment.
- Total energy calculations under the *ab-initio* band structure calculation, by relaxing the experimentally observed volume/formula-unit under pressure confirms that the delicate balance between charge order and frustration in this exotic spinel system.

References

- [1] Y. Horibe, M. Shingu, K. Kurushima, H. Ishibashi, N. Ikeda, K. Kato, Y. Motome, N. Furukawa, Mori S and Katsufuji T, Phys. Rev. Lett. **96** (2006) 086406
- [2] Y. Cai, Z-F. Huang, X. Ming, C. Wang, G. Chen, J. Alloys and Compounds **505** (2010) L23
- [3] Ø. Prytz, E. Flage-Larsen, L. Gu, W. Sgale, P. A. van Aken and J. Taftø, Phys. Rev. **B85** (2012) 195112
- [4] [http:// www. ims.vanderbilt.edu/tem/Lecture](http://www.ims.vanderbilt.edu/tem/Lecture)

- [5] R. F. Egerton, *Electron Energy Loss spectroscopy in the Electron Microscope*, (2011) 3rd Edition, Springer Science+Business Media, New York
- [6] X. W. Lin, Y. Y. Wang, V. Dravid, P. M. Michalakos, M. C. Kung, Phys Rev. **B47** (1993) 3477
- [7] D. H. Pearson, C. C. Ahn and B. Fultz, Phys Rev. **B47** (1993) 8471
- [8] H. K. Schmid and W. Mader, Micron **37** (2006) 426
- [9] H. Tan, J. Verbeeck, A. Abakumov, G. V. Tendeloo, Ultramicroscopy **116** (2012) 24
- [10] G. van der Laan, L. W. Kirkman, J. Phys.: Cond. Matter. **4** (1992) 4189
- [11] F. M. F. de Groot, M. Gnom, J. C. Fuggle, J. Ghijsen, G. A. Sawatzky and H. Petersen, Phys. Rev. **B40** (1989) 5715
- [12] P. Blaha, K. Schwarz, G. K. H. Madsen, D. Kvasnicka and J. Luitz: WIEN2k An Augmented Plane Wave +Local Orbitals Program for Calculating Crystal Properties, Univ. Prof. Dr. Karlheinz Schwarz, Techn. Universität Wien, Institut für Physikalische und Theoretische Chemie, Getreidemarkt 9/156 A-1060 Wien/Austria, ISBN 3-9501031-1-2
- [13] Z. Wu and R. Cohen, Phys. Rev. **B73** (2006) 235116
- [14] K. Matsuno, T. Katsufuji, S. Mori, Y. Moritomoto, A. Machida, E. Nishibori, M. Takata, M. Sakata, N. Yamamoto and H. Takagi, J. Phys. Soc. Japan, **70** (2001) 1456
- [15] M. Croft, V. Kiryukhin, Y. Horibe and S-W. Cheong, New J. Phys. **9** (2007) 86
- [16] P. Marra, K. Wohlfeld, and J. van den Brink, Phys. Rev. Lett. **109** (2012) 117401
- [17] T. Warwick, P. Heimann, D. Mossessian, W. McKinney and H. Padmore, Rev. Sci. Instrum. **66** (1995) 2037
- [18] J. Nordgren, G. Bray, S. Cramm, R. Nyholm, J. E. Rubensson and N. Wassdahl, Rev. Sci. Instrum. **601** (1989) 690

CHAPTER 5

Suppression of charge ordering by Ru substitution in LiMn_2O_4

The known spinel materials with multivalent cations in the B-sub lattice undergo structural transition to relieve the charge frustration. The way each of them relieve the frustration is intriguing. The d-orbitals of the transition metal, present in the B-sub lattice, play a substantial role in aiding the charge ordering and the subsequent structural transition. Transition metal orbitals are conjectured to order and there by aid the formation of multimer ‘molecular’ like units within the B-sublattice. As the system relieves the frustration the tangible experimental evidence appears via a lowering of symmetry (super lattice reflections), increase in electrical resistance and a decrease in magnetic susceptibility at the transition temperature. Amongst the spinels that relieve their charge frustration through structural transition, LiMn_2O_4 , is very different from the rest since it shows a partial charge ordering through a unique formation of octagonal columnar units. In LiMn_2O_4 charge neutrality demands existence of Mn^{3+} and Mn^{4+} . Presence of Jahn–Teller active Mn^{3+} suggests an *a priori* possibility for structural transition. Pristine LiMn_2O_4 , exhibits a cubic (Fd-3m) structure above around 290 K. It undergoes a structural transition to an orthorhombic (Fddd) structure below that temperature. It is interesting to study how a partial substitution for Mn affects the transformation from frustration to order. Hence, in the present thesis work, LiMn_2O_4 samples where Mn is partially substituted with Ruthenium (Ru) have been synthesised. The pristine and the Ru substituted samples are studied using four probe resistivity measurements and Low Temperature Powder X-ray Diffraction (LT-PXRD) experiments.

Analysis of the observed data has been carried out with the view to examine the role of Ru in the ordering of Mn in LiMn_2O_4 .

The chapter has been divided into the following sections: Section 1 brings forth the nature of charge ordering established presently in LiMn_2O_4 by tracing through the relevant literature. Section 2 describes the motivation towards the choice of Ru as a partial substituent to Mn to study charge ordering in LiMn_2O_4 . Section 3 describes the results of synthesis, characterization and the resistivity measurements on Ru substituted LiMn_2O_4 . The analysis of the LT-PXRD is presented in section 4 and finally the results and conclusions are summarized.

5.1 Nature of Charge ordering in LiMn_2O_4

The earliest publication that examined the structural transition in LiMn_2O_4 [1] describes the transition to be from cubic ($Fd-3m$) to tetragonal ($I41/amd$). This transition has been attributed to the co-operative Jahn-Teller effect owing to the presence of Mn^{3+} ($t_{2g}^3-e_g^1$) ions. It is also mentioned that the tetragonal volume fraction increases and saturates to about 65% at 260 K and from there, even down to 220 K, there was no complete transformation. The c/a ratio is observed to be close to 1 ($c/a = 1.011$). Subsequently an EXAFS analysis [2] of LiMn_2O_4 indicates existence of local disorders around Mn^{3+} , even in the cubic structure itself without any static or dynamic long range order. This has led to the assumption that there is charge disproportionation of the kind $\text{LiMn}^{3+}\text{Mn}^{4+}\text{O}_4$ in the system. Thus there are 50% of the Mn ions of the octahedra with identical Mn-O bond length and the rest of the Mn-O octahedra which are anisotropic have two different (a short and a long) bond lengths. “Jahn-Teller phenomena in solids” by Goodenough [3] brings out lucidly, the role played by electron transfer from Mn^{4+} ion

to Mn^{3+} ions in the structural transition of LiMn_2O_4 . This article points out that the Fermi energy is located at the d^4 states in LiMn_2O_4 . Such a location of d^4 states has a consequence, due to electron transfer between equivalent Mn^{4+} and Mn^{3+} sites. Two scenarios can occur based on the electron transfer time and the period for the lattice to relax. If the electron transfer time is faster than the lattice relaxation time, then the empty d^4 states of Mn^{4+} are raised compared to the filled d^4 states of Mn^{3+} . The charge carriers drag the local deformation resulting in small polaronic conduction. On the other hand, if the electron transfer time is slower than the lattice relaxation time, a metallic, itinerant transport appears to occur. Thus a partial structural transition to a tetragonal lattice brought about by the Jahn Teller Mn^{3+} ions that co-exists with the parent cubic lattice is suggested to describe the situation in LiMn_2O_4 . In the mean while, detailed electron diffraction and neutron diffraction experiments as a function of temperature, have shown superlattice spots and weak reflections implying ordering of $(3a \times 3a \times a)$ kind, conforming to orthorhombic (Fddd) structure [4]. The authors confirm existence of single phase down to 230 K. Rietveld refinement of their neutron powder diffraction data reveals existence of five different Mn sites. On the basis of the bond lengths of Mn-O they have interpreted that two of the Mn^{4+} , namely Mn (4) and Mn (5) (Wyckoff positions 32 h) are forbidden from electron transfer. The average Mn-O bond length for the above is 1.91 Å. The other three, namely Mn (1) (Wyckoff positions 16 d), Mn (2) and Mn(3) (Wyckoff positions 32 h) are not pure Mn^{3+} . This is inferred because their average bond distance (Mn-O) is 2 Å, which is smaller than that of the average bond distance of 2.02 Å in the case of pure Mn^{3+} -O indicating static Jahn-Teller distortion. This picture also brings to light that there are 64 localized holes [32 Mn (4) +32Mn (5)]

per cell and the remaining 8 holes are accommodated within the 80 [16 Mn (1) +32 Mn (2) + 32Mn (3)] positions. It is here that there is some probability for hopping. Thus there is partial charge ordering in LiMn_2O_4 . This seminal paper by Rodriguez- Carvajal invokes orbital ordering in LiMn_2O_4 that results from the Jahn-Teller polaronic mobile charges. Following this, LTXRD measurements [5] on LiMn_2O_4 , carried out using synchrotron source, have confirmed the orthorhombic (Fddd) structure down to 260 K. They also claim that both the two phases (cubic and orthorhombic) coexist. Moreover, this work indicates a rhombohedral to tetragonal ($F4_1/ddm$) transition below 100 K down to 40 K. With this back ground, in the present thesis work, it is planned to examine the cubic –orthorhombic transition through partial substitution for Mn in LiMn_2O_4 .

5.2 Motivation for the substitution of Ru for Mn in LiMn_2O_4

Substitutions in LiMn_2O_4 have been carried out to improve the battery performance by arresting the phase transition around 290 K. Substitution of Mg for Li has been carried out [6] to increase the concentration of Mn^{3+} . It is observed that even 4 at% ($\text{Li}_{0.96}\text{Mg}_{0.04}\text{Mn}_2\text{O}_4$) substitution suppresses the transition. If the structural transition is due to Jahn-Teller effect, it should not have been the case as substitution of Mg is expected to increase the concentration of Mn^{3+} . Thus it is concluded that the ordering of holes and electrons in a system results when there is simple charge disproportionation (3.5). Mg substitution disturbs and drives the system away to a complex disproportionation ultimately destroying the ordering. Fe has been substituted for Mn [7] in LiMn_2O_4 . Based on the isomer shift and quadruple splitting in Mossbauer experiments, and also based on the increase in lattice parameter as a function of Fe concentration, it is found that Fe must be partially substituting Mn^{4+} as Fe^{4+} and Mn^{3+} as

Fe^{3+} . Absence of endothermic peak in DSC for Fe 0.15 in $\text{Li}_{0.9}\text{Mn}_{2-x}\text{Fe}_x\text{O}_4$ samples indicates suppression of charge ordering transition. While an excess of Li has been observed [8] to shift the transition to 260 K, inclusion of Fe, to the Li excess sample seems to further bring down the structural transition to 250 K in $\text{Li}_{1.0125}\text{Mn}_{1.9625}\text{Fe}_{0.025}\text{O}_4$ [9] as studied using LTXRD measurement. Substitution of Mn by Ru has been carried out in the context of LiMn_2O_4 as an electrode. Substitutions with $x=0, 0.1$ and 0.25 for $\text{LiMn}_{2-x}\text{Ru}_x\text{O}_4$ have been synthesized and studied using RT-XRD and X-ray absorption spectroscopy of Mn ions and XANES of the Ru ions[10]. Though this study talks about the better electrode performance corresponding to $x= 0.25$, no analysis has been done in the context of charge ordering. From the X-ray absorption and XANES it has been inferred that Ru resides as Ru^{4+} on the Mn^{4+} sites. With this back ground Ru substitution has been taken up for detailed studies to examine its role in the charge ordering transition.

5.3 Synthesis, characterization and four-probe resistivity measurements of $\text{LiMn}_{2-x}\text{Ru}_x\text{O}_4$ ($x= 0.025, 0.05, 0.075, 0.1, 0.15, 0.2$)

5.3.1 Synthesis of pristine and Ru substituted LiMn_2O_4

It can be observed from the vast number of publications available in the literature that a variety of methods have been followed for the synthesis of LiMn_2O_4 . These include the solid state and solution routes. Similarly a variety of firing schedules and heat treatment schedules have also been reported. In the present work, samples of $\text{LiMn}_{2-x}\text{Ru}_x\text{O}_4$ with $x=0.025, 0.05, 0.075, 0.1, 0.15, 0.2$ have been synthesized using a solid state method [11]. Synthesis conditions have been set and tuned to obtain phase pure pellets of pristine and Ru substituted samples. Stoichiometric quantities of Li_2CO_3 (Alfa Aesar, 99.998%) and Mn_2O_3 (Alfa Aesar, 99.9%) have been thoroughly ground and

pelletised for the synthesis of pristine LiMn_2O_4 . The pellets have been pre-fired at $650\text{ }^\circ\text{C}$ for 12 hrs and fired at $800\text{ }^\circ\text{C}$ for 24 hrs. , then furnace cooled to room temperature. For the Ru substituted samples, stoichiometric quantities of RuO_2 powder (Alfa Aesar, 99.9 %) are used. After calcination, the products are re-ground, re-pelletised and heat treated at $800\text{ }^\circ\text{C}$ for 24 hrs. The same sequence of procedure has been adopted for the synthesis of $\text{LiMn}_{2-x}\text{Ru}_x\text{O}_4$, with $x=0.025$; For $x=0.04, 0.05$ and 0.06 samples after the first firing for the reaction following the same sequence a second heat treatment at $850\text{ }^\circ\text{C}$ has been carried out; For $x=0.075$ treatment at $900\text{ }^\circ\text{C}$ and for 0.1 and 0.15 a treatment at $1000\text{ }^\circ\text{C}$ seemed essential for single phase formation. Listed below in Table 5.1 are the ionic radii and the electron counts in d levels for Mn and Ru. The orbitals of 4d are extended compared to the 3d orbitals.

Table 5.1. Ionic Radii and electron count for Mn and Ru

| | Ionic radii | Electron count |
|------------------|-------------|----------------|
| | Å | |
| Mn^{3+} | LS | 0.72 |
| | HS | 0.785 |
| Mn^{4+} | 0.67 | d^3 |
| Ru^{3+} | 0.82 | d^5 |
| Ru^{4+} | 0.76 | d^4 |
| Ru^{5+} | 0.565 | d^3 |

5.3.2 Characterisation of pristine and Ru substituted LiMn_2O_4

a. Powder X-ray diffraction

Phase purity has been examined using powder X-ray diffraction in the STOE diffractometer with Cu K-alpha radiation in the Bragg Brentano para-focussing geometry. Figure 5.1 shows the powder diffraction pattern of pristine LiMn_2O_4 .

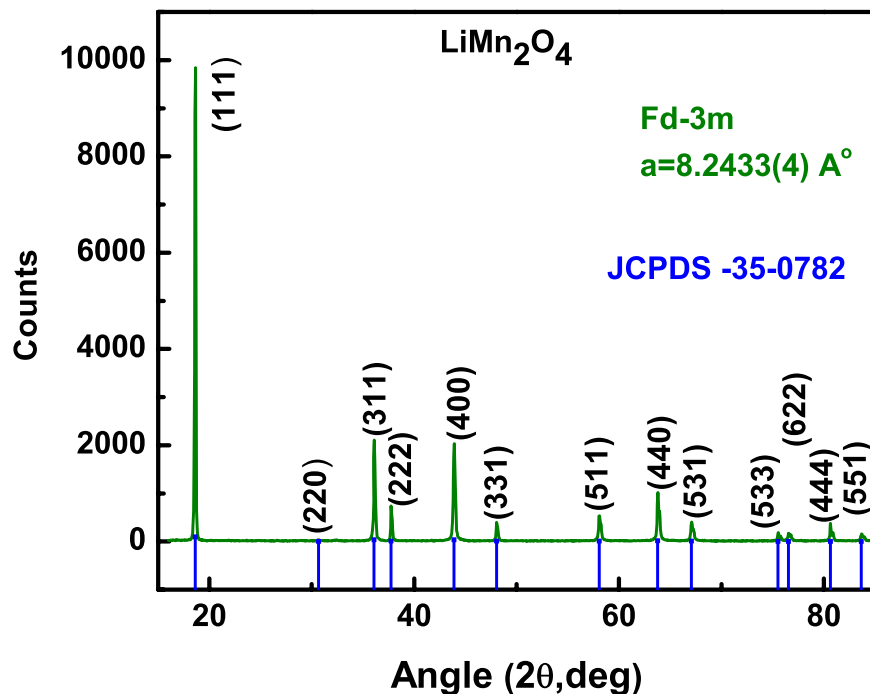


Figure 5.1 Powder diffraction pattern of pristine LiMn_2O_4 . Blue lines at the bottom correspond to the best quality reference data (ICDD card No. 35-0782)

Comparing with the ICDD data (card No. 35-0782) the phase purity is confirmed. The absence (in fact un observably low intensity) of reflection from (220) plane very clearly indicates that no cationic substitution is present at the 16d site and it is fully occupied by Li. Single phase Ru substituted compound could be obtained only up to $x=0.15$; Repeated attempts to synthesize phase pure $x=0.2$ compound by varying the temperature of synthesis and heat treatment step by step from 1000 to 1050 °C still left un-react ed RuO_2 . Hence the phase pure compounds from $x=0$ to $x=0.15$ are considered for further study. Within these compositions a repeat heat treatment at a slightly elevated temperature aided inclusion of un-reacted RuO_2 , if any, in to the system. Powder

diffraction patterns obtained for all the compositions are shown in figure 5.2. It can be observed from the figure that all the compositions up to $x=0.15$ are phase pure.

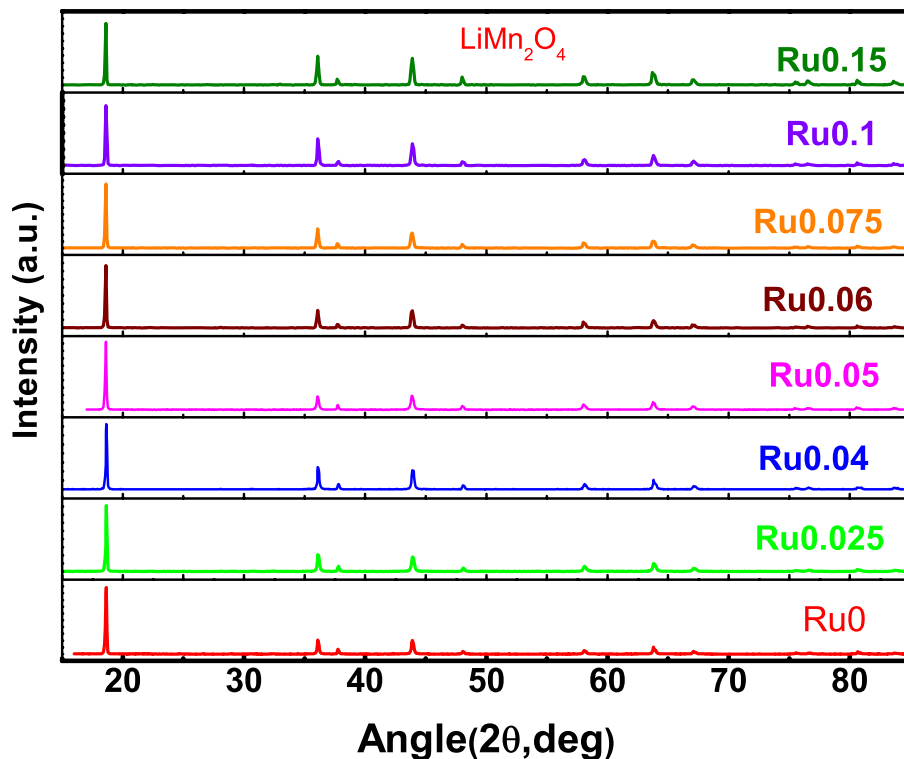


Figure 5.2 Powder diffraction pattern of pristine and Ru substituted LiMn_2O_4

Lattice parameters estimated for the pristine and the Ru substituted for $\text{LiMn}_{2-x}\text{Ru}_x\text{O}_4$ are presented in figure 5.3. For the pristine compound the observed value of $8.2433(4) \text{ \AA}$ compares well with the lattice parameter value of 8.247 \AA quoted in the ICDD data. Using the information available in the literature relating oxygen stoichiometry and lattice parameter [10] it can be estimated that the oxygen stoichiometry in the pristine sample is 4.02. On substitution with Ru it is observed that there is a small increase in the lattice parameter indicating a possible substitution of Ru^{3+} for Mn^{3+} or

Ru^{4+} for Mn^{4+} . The latter possibility is considered acceptable from the XAS and XANES measurements carried out on $\text{LiMn}_{2-x}\text{Ru}_x\text{O}_4$ in the literature [10].

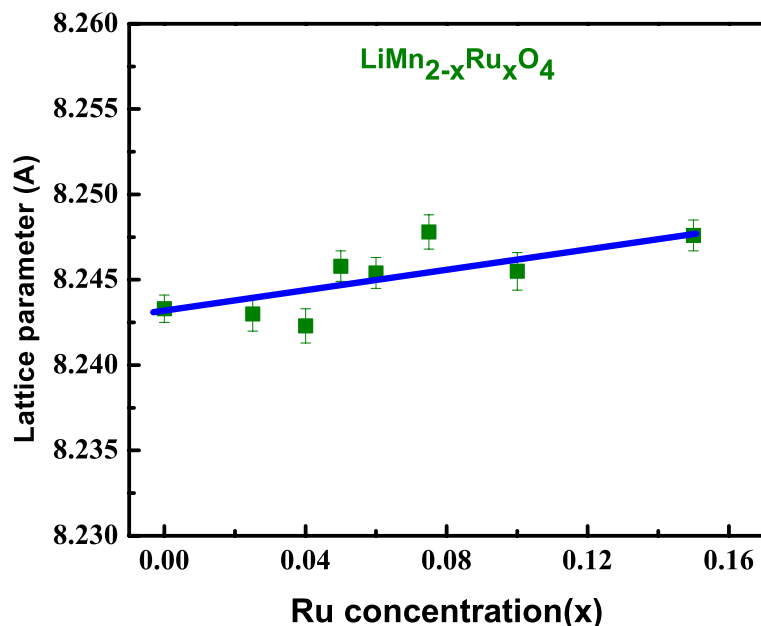
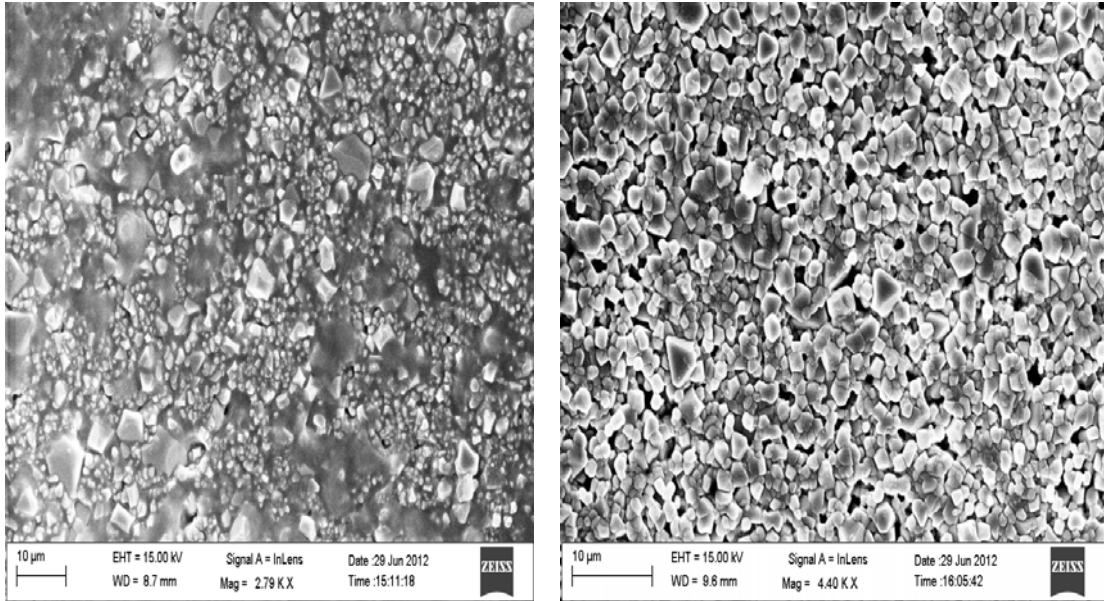


Figure 5.3 Variation of lattice parameter in $\text{LiMn}_{2-x}\text{Ru}_x\text{O}_4$ Vs Ru concentration

b. Scanning electron microscope

In order to get an idea of the morphology of the samples, typically two samples have been identified for obtaining the SEM, namely the pristine LiMn_2O_4 and the $x=0.075$ (a middle composition) of the Ru substituted LiMn_2O_4 . From the SEM pictures shown in figure 5.4, for the pristine (a) and $x=0.075$ (b) samples the triangular morphology characteristic of the spinel compounds can be observed. Large variation in grain size is observed in the case of pristine LiMn_2O_4 . In the case of $x=0.075$ samples it can be seen that most of the grains are of similar size. The grains are also more homogenous for the sample with composition $x=0.075$, as it is annealed at a higher temperature (900 °C). Though the role of grain connectivity in CMR manganites [12] and

superconductors [13] are well documented, especially in the context of electrical conductivity not much literature exists with respect to spinel materials.



(a)

(b)

Figure 5.4 Typical SEM picture of (a) pristine LiMn_2O_4 (b) $x=0.075$ sample showing triangular morphology characteristic of the cubic spinel system

5.3.3 Four probe Electrical resistance studies on pristine and Ru substituted LiMn_2O_4

5.3.3.1 Measurement of resistance at low temperatures using a dip-stick apparatus

DC electrical Resistivity is one of the valued tools in a condensed matter laboratory for polycrystalline and single crystalline samples, despite the fact that many times it is not much approved for poly crystalline pellets with a multitude of grain boundaries. At a given temperature the DC resistivity of the specimen without the inclusion of the lead wires can be obtained from a linear four probe method or a van der Pauw method. A derivation of the van der Pauw equation is found in the literature [14-

15]. In general, resistance as a function of temperature can be obtained either by holding the sample at a constant temperature in an exchange gas chamber or by gently moving a dip stick in a Helium Dewar. For the measurements pertaining to this thesis an already available, home-made dip stick apparatus is used where the latter approach is adopted.

As shown in figure 5.5 the sample holder, made up of OFHC (oxygen free high conductivity) copper block, is soft soldered to a thin walled SS tube through which electrical leads from the sample pellets and thermometer are brought out to an electrical terminator. Electrical contact to the sample is established by attaching fine Cu wires using a conducting silver paste. With due care to the temperature gradient, provision is made for studying multiple samples. A Wilson's seal on top of the dip-stick assembly enables closing of the liquid Helium Dewar after inserting the dip-stick in it. The temperature of the sample is varied by exploiting the temperature gradient present above the liquid level in the Helium Dewar. Data collection is carried out while warming and cooling the sample.

A Si diode sensor is used for the temperature measurement. A constant current source with very high stability and a nano voltmeter ensure accurate measurement of resistance. The data collection is automated so that the recorded data can be processed later. The resistivity can be obtained by appropriately incorporating the geometry of the sample pellet in the van der Pauw formula.

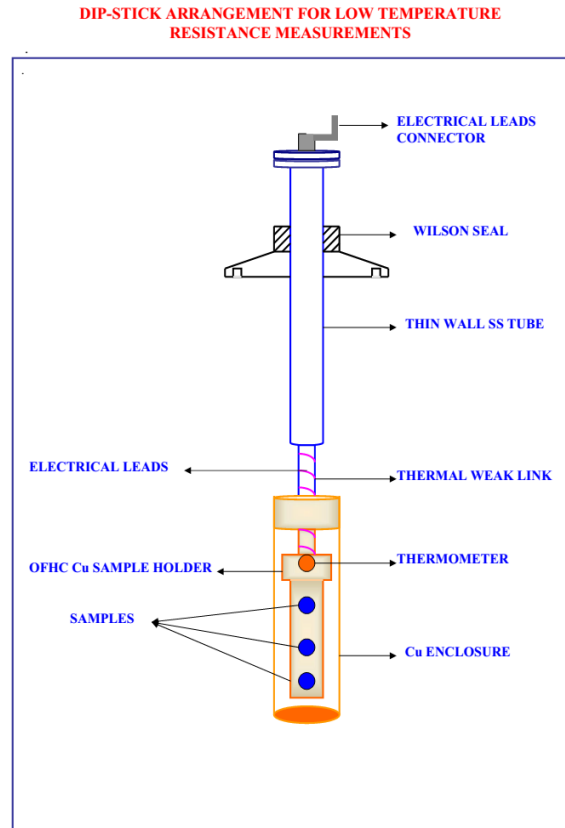


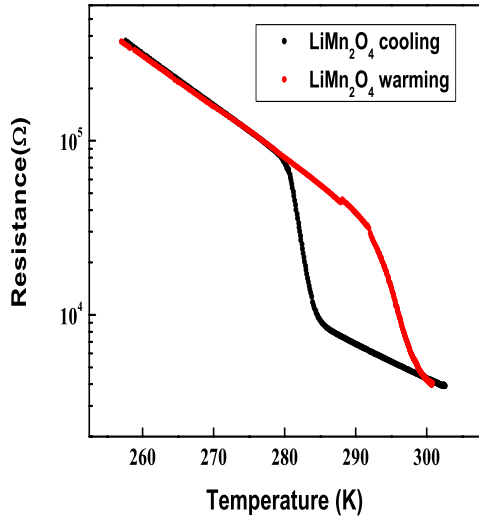
Figure 5.5 Schematic of the Low Temperature resistivity dip stick

5.3.3.2 Results of the resistance studies

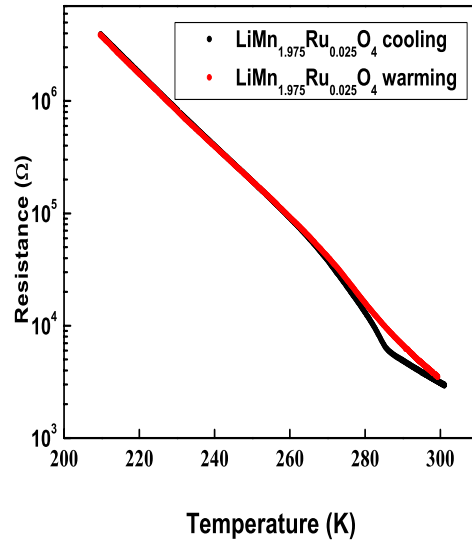
Four probe resistance measurement carried out on pristine and Ru substituted LiMn_2O_4 pellets during very slow cooling and warming of the sample are plotted in figure 5.5.

The following observations can be made from the R Vs T plots presented in the figure:

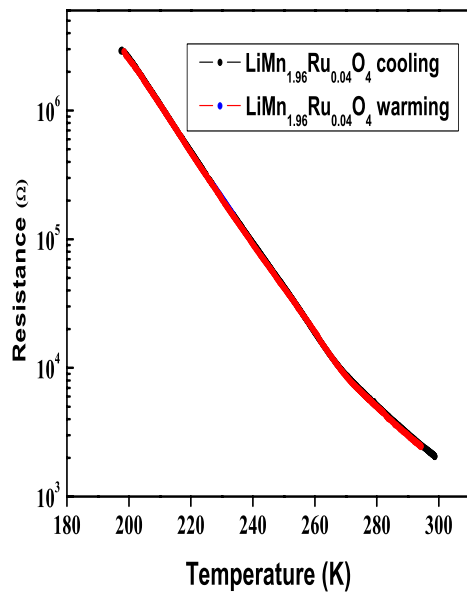
- The pristine sample (Figure 5.6(a)) shows a very pronounced hysteresis. On cooling there is a semiconductor like increase which jumps to one order of magnitude higher value at the transition at around 285 K. After the transition, once again the resistance shows a semi conductor like variation as a function of temperature.



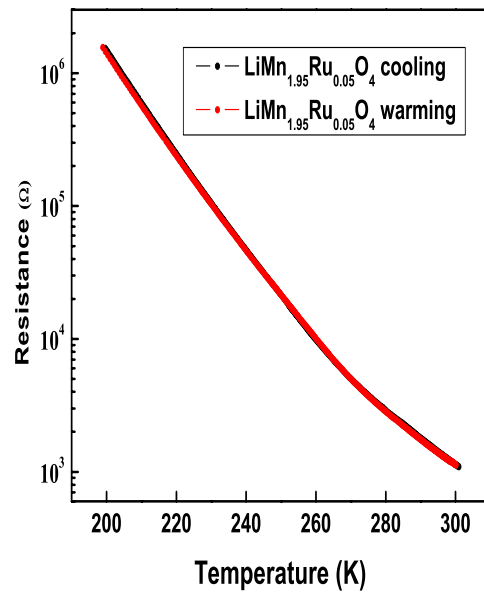
(a)



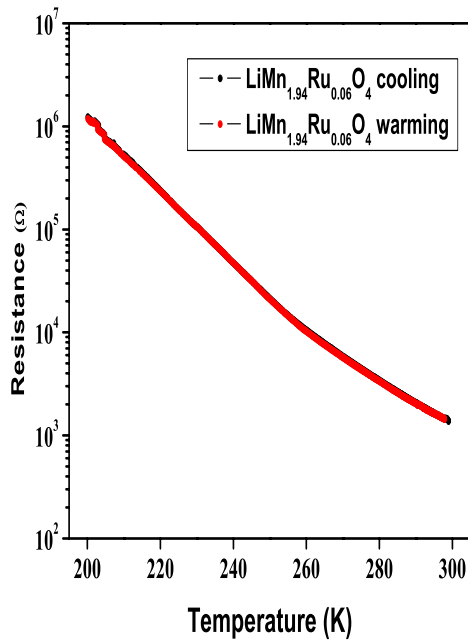
(b)



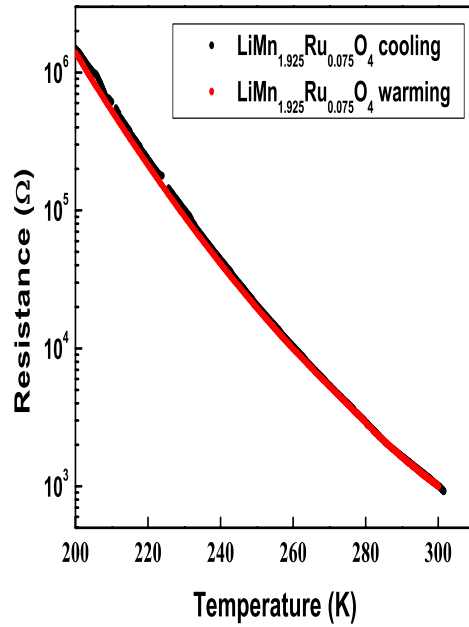
(c)



(d)



(e)



(f)

Figure 5.6 Variation of resistance with temperature. Ru concentration is mentioned in the legend

- With just about 1.25% ($x=0.025$) of Ru (Figure 5.6(b)) there is a remarkable reduction in the hysteresis. The increase in resistance accompanying the transition is much less than an order of magnitude.
- For 2%, 2.5% and 3% ($x= 0.04, 0.05$ and 0.06) of Ru in the Mn position shown in figure 5.6 (c), (d), and (e), the hysteresis further diminishes but a slope change is seen unmistakably.
- For 3.75% ($x=0.075$) shown in figure 5.6 (f) the slope change is barely visible.

Since it is known that in LiMn_2O_4 , the resistive transition is tied to the structural transition, from the disappearance of the observed resistance jump, it appears that the

transition is restrained for substitution of Ru beyond 3% in LiMn_2O_4 . In addition to the above observations, the room temperature resistivity estimated from the observed resistance values (four-probe, Van der Pauw geometry) and the thickness of the pellet is found to show a large variation on Ru substitution. Ambient temperature resistivity shows an exponential fall on substitution of Ru as the concentration of Ru increases as shown in figure 5.7. A lot of literature is available on substitution of Ru for Mn in a variety of condensed matter systems. For example in the case of perovskite manganites, presence of Ru weakens the ferromagnetism and metallicity in $\text{La}_{0.7}\text{Sr}_{0.3}\text{MnO}_3$ [16]. In another compound $\text{La}_{0.67}\text{Ca}_{0.33}\text{MnO}_3$ [17], Ru substitution shows a reduced rate of fall of insulator to metal transition temperature (dT_c/dx) compared to substitutions of other elements for Mn. In the present context, considering the substitution of Ru for Mn in LiMn_2O_4 , an increase in electronic conductivity is discussed and attributed to the electron hopping on substitution of Ru for Mn [17].

Two scenarios can be thought of. They are, Ru substitutes for Mn^{3+} as Ru^{3+} or the other possibility that Ru substitutes for Mn^{4+} as Ru^{4+} . In both the situations, the lattice parameter is expected to show an increase as observed. On Ru substitution, the electron count in the d-orbital is increased on both the situations. At a given temperature if Mn^{4+} is replaced with Ru^{4+} , since both Mn^{4+} and Ru^{4+} have empty e_g orbitals and Ru orbitals are extended d-orbitals, it is likely to enhance the electron mobility from Mn^{3+} . This may be the reason for the observed sharp decrease in the resistivity. On the contrary if Mn^{3+} is replaced with Ru^{3+} , this depletes the electron in the e_g orbital and hence the conductivity must have decreased.

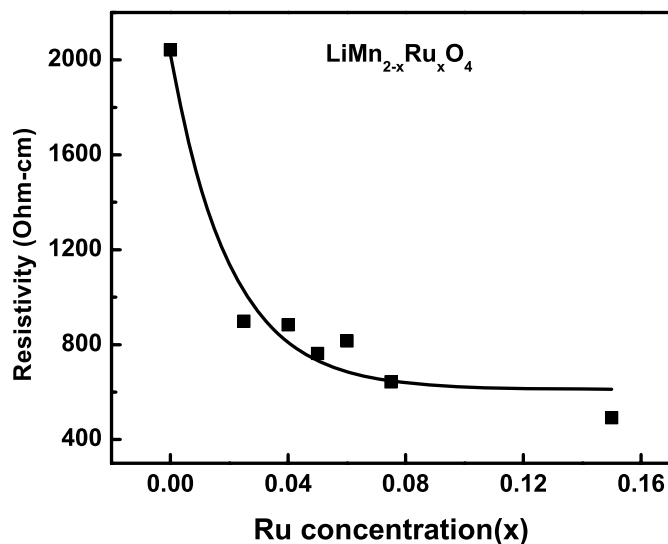


Figure 5.7 Variation of resistivity as a function of Ru concentration in $\text{LiMn}_{2-x}\text{Ru}_x\text{O}_4$

5.4 Low Temperature synchrotron powder XRD measurements on $\text{LiMn}_{2-x}\text{Ru}_x\text{O}_4$

While resistivity measurements indicate modifications of the electron organisation in the material, structural observations bring to light the details of such ordering. A clean synchrotron data with Rietveld refinement with care to the constraints and parameters of refinement can lend a lot of information about the structural transition through variation of bond angles and bond lengths. With this in mind the pristine and Ru substituted samples are subjected to synchrotron radiation at INDUS-2, at Indore, India. INDUS-2 is a 2.5 GeV Synchrotron source. Presently it offers 100 mA current. The powder XRD measurements have been carried out in the ADXRD beam line.

5.4.1 Details of the ADXRD Beam line BL-12 at INDUS-2 [18-19]

The ADXRD beam line of INDUS-2 is sourced by a bending magnet. The first optical element is a platinum coated pre mirror used for vertical focusing of the beam. A Double Crystal monochromator (DCM) with Si (111) acts as the second optical element and is used for realizing a monochromatic beam. A third optical element, a platinum coated mirror again helps in further vertical focusing. The beam line operates at a spectral range of 5-20keV with a spectral resolution of 1eV at 10keV. The flux at 10 keV is about 1000 photons/sec. The beam size is 1mm x 0.5mm. The powder diffraction experiments at ambient temperatures can be carried out with a point detector or an image plate detector. Calibration of the energy and the sample to detector distance is carried out using standard LaB₆ powder.

Fine powders of the standard LaB₆ are loaded between Kapton foil. The foil with the standard powder is placed in a Be supported sample holder. Data collection is carried out at ambient temperature. The 2d - Debye- Scherrer rings on the image plate are converted to 1-d two theta Vs intensity using an optimization algorithm called FIT 2D. The precise X-ray wave length and the distance 'd' between the sample and the detector are obtained. This procedure of calibration using LaB₆ powder is carried out at the beginning of the run for every sample before starting the flow of liquid Helium

5.4.2 LTXRD attachment at BL-12 beam line in INDUS-2

A continuous flow cryostat is available at the ADXRD beam line. With this attachment, powder diffraction measurements can be carried out down to 10 K. The cryostat has an evacuation port and two more ports for liquid inlet and outlet. The outlet port is connected to the Helium recovery line. A flow meter is connected to the inlet port

to control the liquid flow. Figure 5.8 shows the parts of the low temperature attachment available for users at the ADXRD beam line. A cold finger that ends in a ring is provided such that a circular Be foil of thickness about 200 μm is placed in the ring. The sample powder is pressed between two Kapton foils and fixed to circular ring with the Be foil. Two Be domes cover the sample. The annular region between the sample and the dome can be evacuated. Thus the domes serve as radiation shields. Two thermo couples one at the tip of the cold finger and the other at the shield are present for sensing and controlling the temperature. The sample chamber is cooled by flowing liquid He and held at any required temperature.

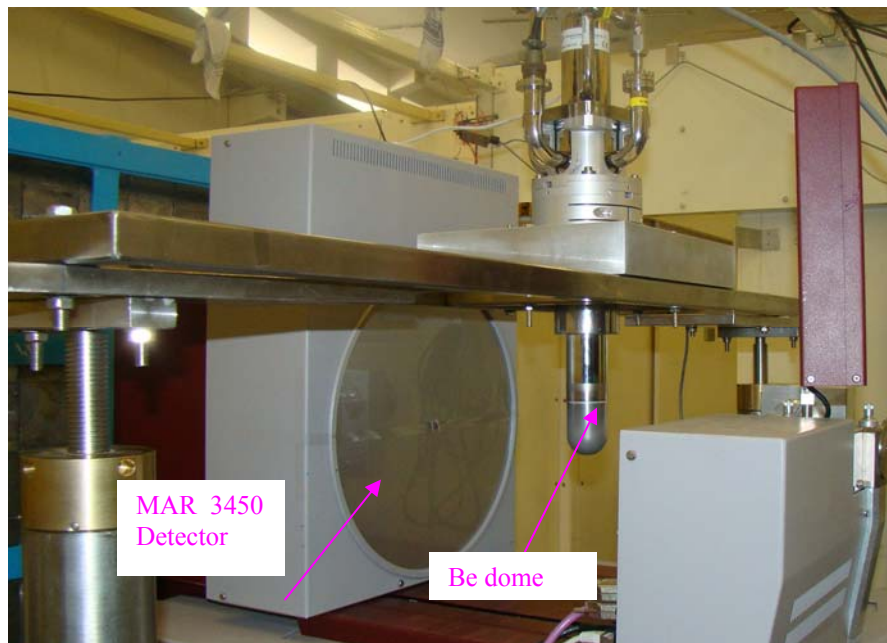


Figure 5.8 The LTXRD attachment at BL-12 in INDUS-2. The Be dome for holding the sample under vacuum at low temperature and the MAR detector are indicated by the arrows. The continuous flow cryostat resting on the frame is seen above the dome.

Once the sample reaches the set temperature and remains steady, the powder diffraction data is collected on the image plate. The precise X-ray wave length and the distance ‘d’ between the sample and the detector obtained during calibration are used to

estimate the Bragg angles for the sample. The temperature stability at 200 K is +/- 0.1 K. By appropriately controlling the liquid flow and the heater current small step sizes in temperature can be set up. With the synchrotron beam the data collection time is very small (about 1 or 2 minutes). The energy of the beam is adjusted around 11 keV to cover the q values corresponding to the (511) plane of the cubic LiMn_2O_4 . This is ensured since it is identified that the orthorhombic reflections appear clearly corresponding to this d – spacing.

5.4.3 Result of the ambient temperature powder XRD measurement

The powder XRD pattern obtained for the pristine LiMn_2O_4 sample at ambient temperature is shown in figure 5.9. It is seen from the figure that the reflections from the Be cups covering the sample holder clearly dominates the observed spectrum. If the cross section of the Be cups and sample in its Be holder are considered it can be realized that there are four points of the two Be holder that cut the X - ray beam. So this makes every Be reflection appear multiple times based on the sample to detector distance.

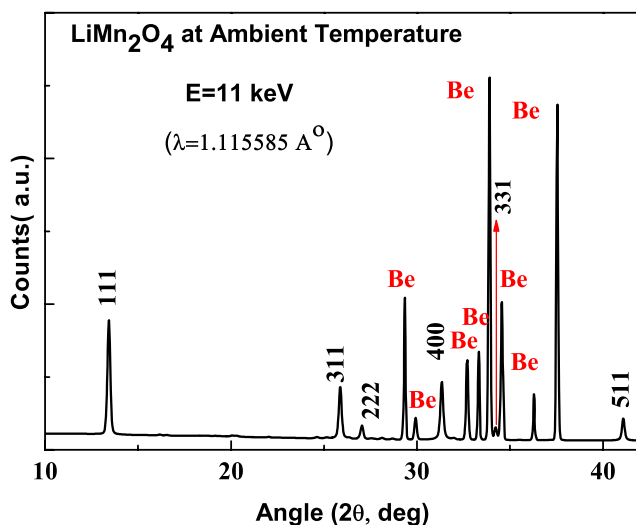


Figure 5.9 Powder diffraction pattern of the pristine LiMn_2O_4 at ambient temperature

Leaving aside the strong Be lines, the reflections from the frustrated cubic spinel (Fd-3m) phase of the pristine LiMn_2O_4 are indexed. The interference from beryllium reflections with high intensity and background has hampered meaningful Rietveld refinement of the data. However, the intense synchrotron beam and the availability of the low temperature attachment have enabled observing the structural transition with ease.

5.4.4 Results of the LTXRD measurements

A part of the LTXRD pattern obtained for the pristine LiMn_2O_4 while cooling the sample from room temperature has been shown in figure 5.10. Splitting of the $(5\ 1\ 1)_c$ reflection of the frustrated cubic spinel phase is the signature of the transformation to the charge ordered orthorhombic (Fddd) phase.

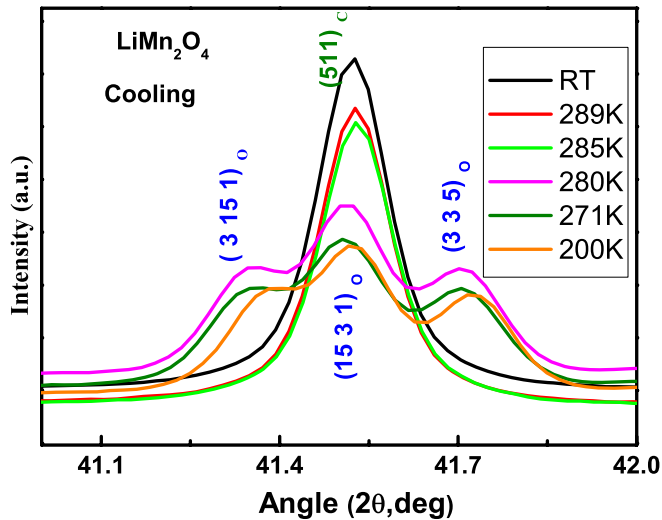


Figure 5.10 LTXRD pattern of LiMn_2O_4 showing the splitting of the Cubic (511) reflection

Such a splitting is also observed in the $(4\ 0\ 0)$ reflection of the cubic phase (not shown). The indices of the orthorhombic reflections are $(3\ 15\ 1)$, $(15\ 3\ 1)$ and $(3\ 3\ 5)$. The transition itself occurs between 280 and 285 K. Comparing this with the resistive

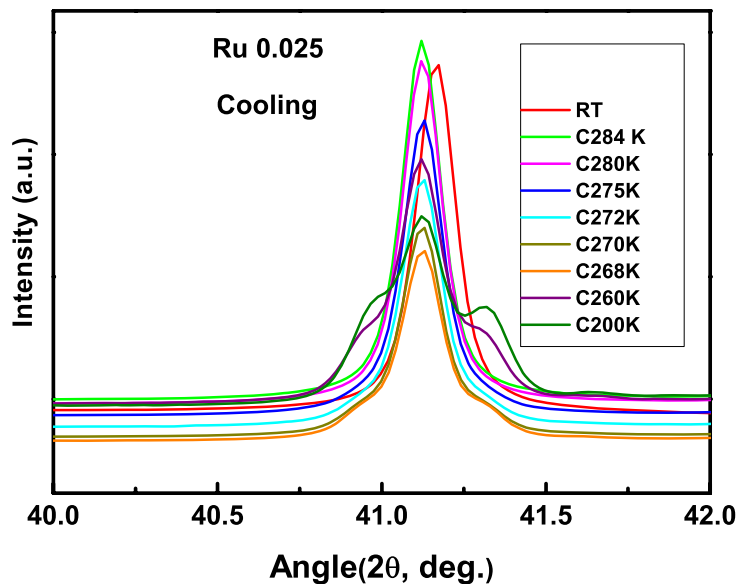


Figure 5.11 LTXRD pattern of $\text{LiMn}_{1.975}\text{Ru}_{0.025}\text{O}_4$ showing the splitting of the Cubic (511) reflection.; Data collection during cooling.

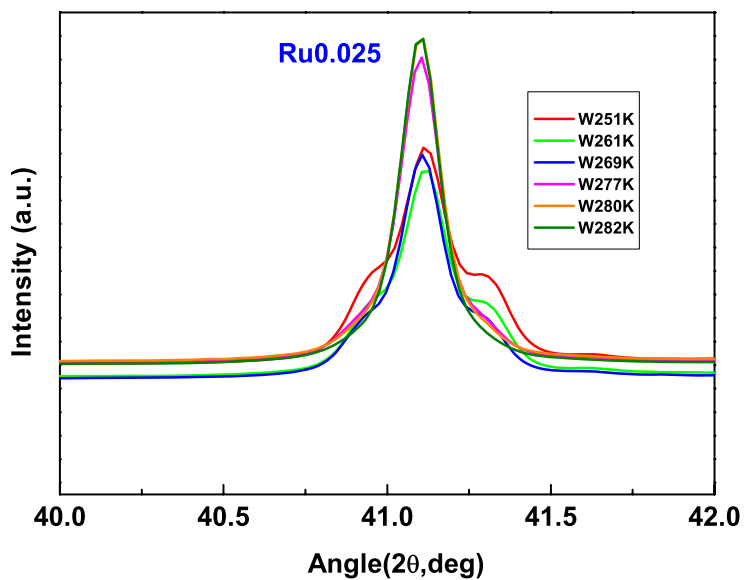


Figure 5.12 LTXRD pattern of $\text{LiMn}_{1.975}\text{Ru}_{0.025}\text{O}_4$ showing the splitting of the Cubic (511) reflection; Data collection during warming.

transition observed on cooling the sample (figure 5(a)), the agreement can be clearly seen. Thus the structural transition and the electronic transition are tied in LiMn_2O_4 as expected in a charge ordered material.

Figure 5.11 shows a part of the X-ray diffractogram in the case of $\text{LiMn}_{1.975}\text{Ru}_{0.025}\text{O}_4$ as observed on cooling the sample. The splitting of the cubic (5 1 1) reflection in to the orthorhombic reflection is located between 270 and 275 K. This information can be compared with the resistance data of figure 5.6 (b). The resistive transition starts at a temperature $T > 280\text{K}$. The resistivity and structural measurements have been carried out without deliberately maintaining a constant rate of cooling. Keeping this limitation in the mind, it can be interpreted that the lattice response is sluggish compared to the electronic response.

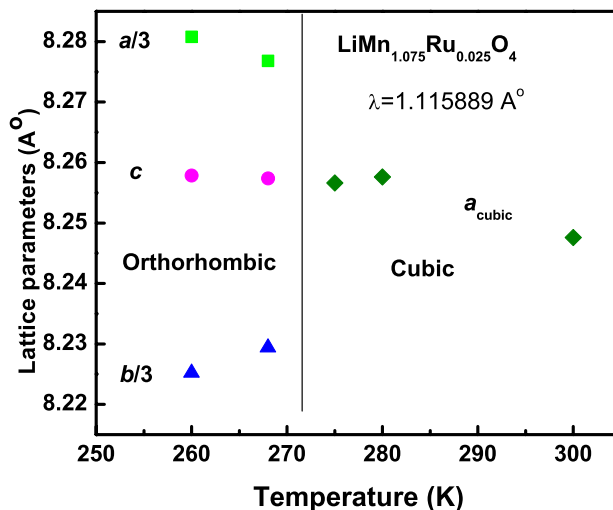


Figure 5.13 Variation of lattice parameter with temperature in $\text{LiMn}_{1.975}\text{Ru}_{0.025}\text{O}_4$. The cubic to the orthorhombic structural transition occurs between 270 and 275 K.

Once the sample reaches 200 K, the warming cycle of data collection is commenced.

Figure 5.12 shows the relevant angular region of the diffraction data bringing out the

transition from partially charge ordered orthorhombic to frustrated cubic structure. The transformation appears to occur between 277 and 280 K. This clearly brings out the hysteretic nature of the transition. Once again, comparing the resistance measurement it is seen that the change of slope is not so pronounced in the warming cycle (Figure 5.6(b)). From each diffraction data set corresponding to a particular temperature, the lattice parameter of the system at that temperature is calculated.

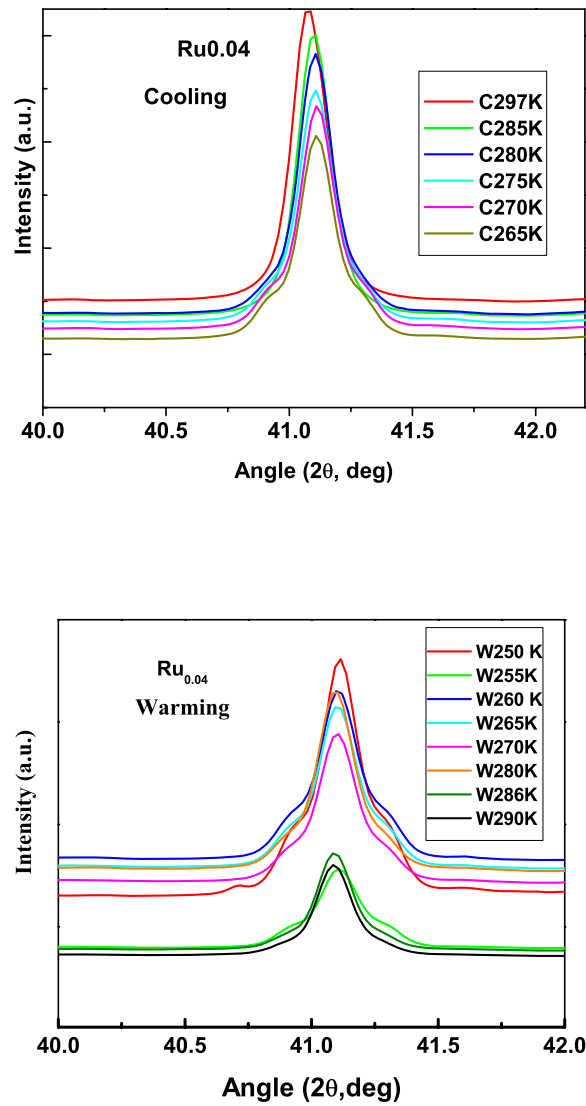


Figure 5.14 LTXRD pattern of $\text{LiMn}_{1.96}\text{Ru}_{0.04}\text{O}_4$ showing the splitting of the Cubic (511) reflection; Data collection during cooling and warming.

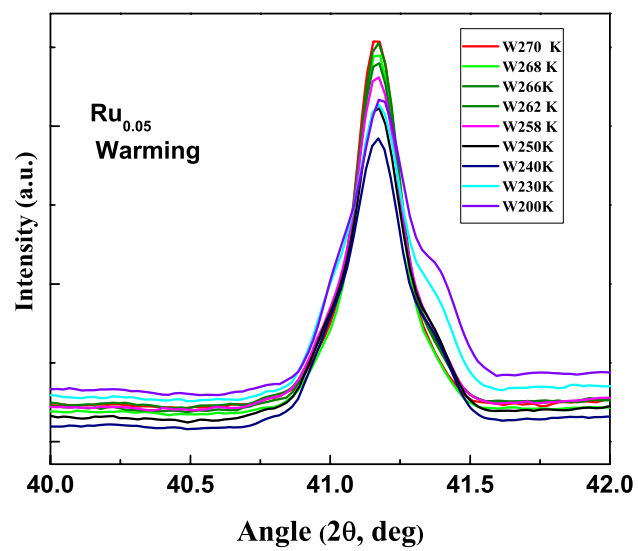
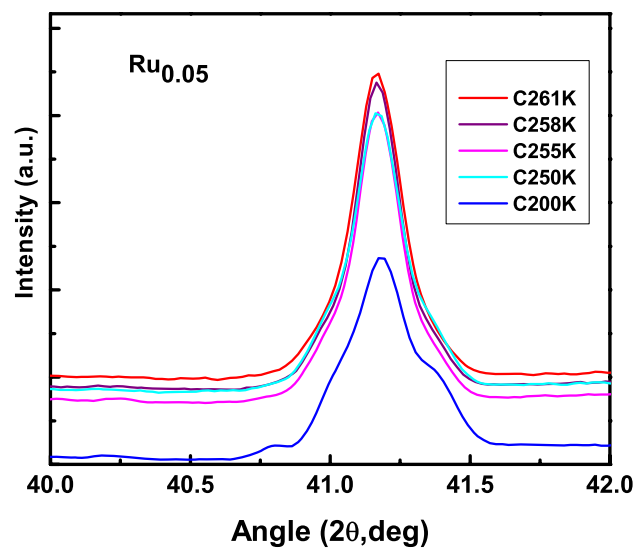


Figure 5.15 LTXRD pattern of $\text{LiMn}_{1.95}\text{Ru}_{0.05}\text{O}_4$ showing the splitting of the Cubic (511) reflection; Data collection during Cooling and warming

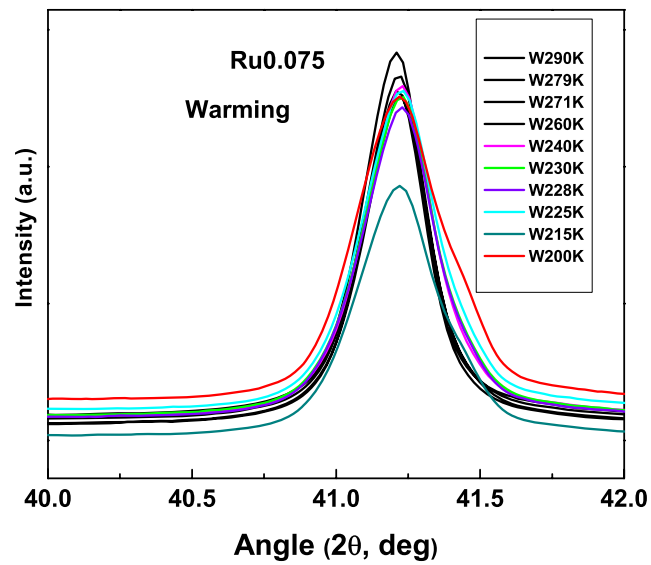
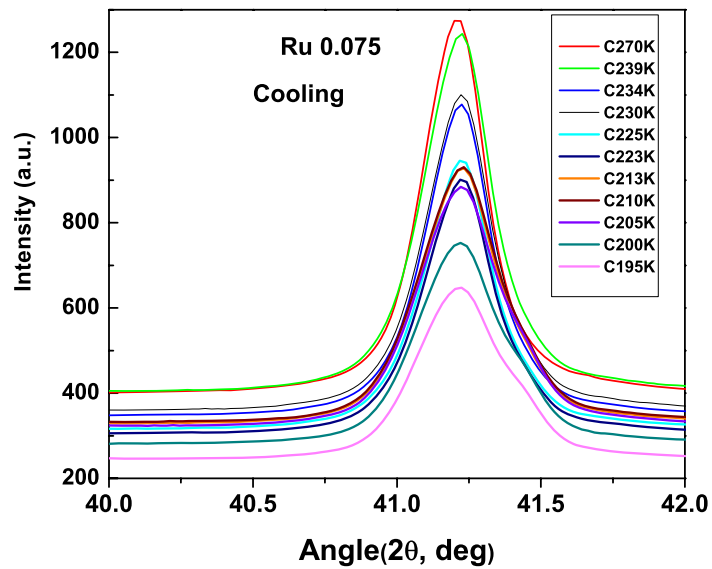


Figure 5.16 LTXRD pattern of $\text{LiMn}_{1.25}\text{Ru}_{0.075}\text{O}_4$ showing the splitting of the Cubic (511) reflection; Data collection during Cooling and warming

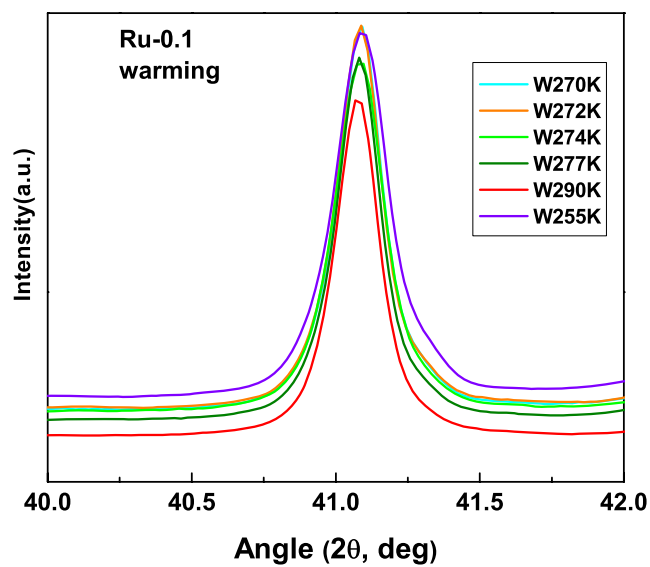
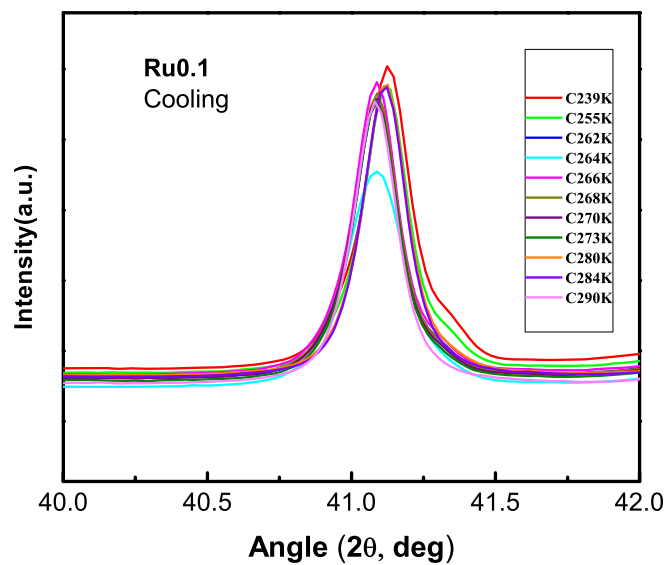


Figure 5.17 LTXRD pattern of $\text{LiMn}_{1.9}\text{Ru}_{0.1}\text{O}_4$ showing the splitting of the Cubic (511) reflection; Data collection during Cooling and warming

Typical lattice parameters are presented in figure 5.13 for $\text{LiMn}_{1.975}\text{Ru}_{0.025}\text{O}_4$. The transition from cubic to orthorhombic structure as the frustration is relieved in the system is clearly seen from figure 5.13.

The transition between frustrated cubic and charge ordered orthorhombic phases recorded during warming and cooling for $\text{Ru} = 0.04, 0.05, 0.075$ and 0.1 are plotted in Figure 5.14, 5.15, 5.16 and 5.17.

5.4.5 Phase diagram for $\text{LiMn}_{2-x}\text{Ru}_x\text{O}_4$

The transition temperature as a function of Ru concentration obtained (during cooling) has been presented in figure 5.18.

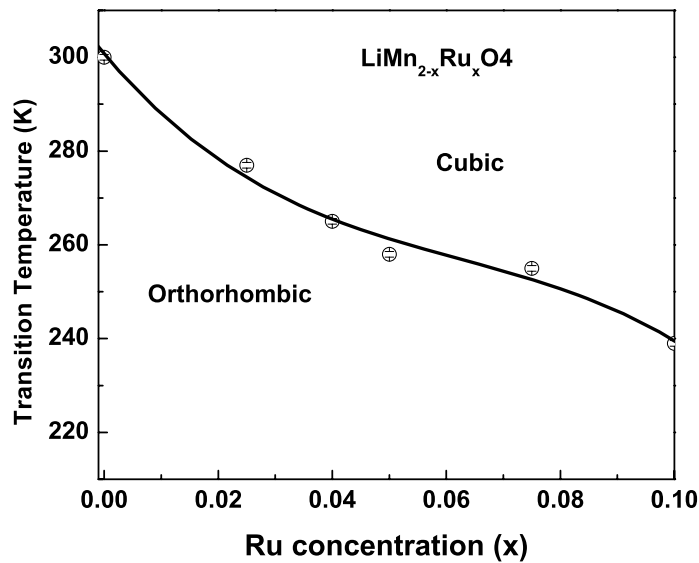


Figure 5.18 Phase diagram for $\text{LiMn}_{2-x}\text{Ru}_x\text{O}_4$ showing the cubic and orthorhombic phases

It is observed that up to Ru concentration of 0.1 the transition to orthorhombic structure survives, though it is suppressed in temperature. From the observed data a trend can be obtained regarding the nature of phase transition in $\text{LiMn}_{2-x}\text{Ru}_x\text{O}_4$. It is known

from the proposed structure [4] for the charge ordered state of LiMn_2O_4 that below the transition temperature the Mn^{4+} orders in an octagonal columnar network. Within this the Mn^{4+} ions do not change their valence state. Whereas there is hopping among the other Mn^{3+} and Mn^{4+} which are not ordered. When Ru is added to the system and if it substitutes the Mn^{4+} , then there can be hopping due to the extended d-orbitals of Ru. Thus along with the reduction in resistivity, there is probably sustained randomness rather than a freezing of orbitals. Thus with Ru substitution the frustration is sustained rather than the charge order.

Summary and conclusions

LiMn_2O_4 is, like AlV_2O_4 , is a charge frustrated cubic spinel system known in the literature. It is also known that it undergoes partial charge ordering when cooled below 290 K by a novel octagonal columnar formation of Mn^{4+} . The charge ordered orthorhombic (Fddd) system is characterized by five different Mn, two of which Mn(4) and Mn(5) are placed in undistorted Mn-O octahedra formed with Mn^{4+} ions ; the other three Mn(1), Mn(2) and Mn(3) are occupied with largely Mn^{3+} and some Mn^{4+} with distorted Mn-O octahedra. Thus the presently available literature unveils a picture of orbital ordering of Mn^{4+} , followed by a static Jahn-Teller distortion of the Mn^{3+} . The increase in resistance in the charge ordered state is attributed to the diminished hopping possibilities between the Mn^{4+} and Mn^{3+} . In this back ground, the present thesis work attempts to substitute Mn with Ru to learn how Ru substitution affects the occurrence of charge ordering and to find if Ru destroys the transition or shifts the transition to a lower temperature.

The following summarises the effort and the conclusions:

- Ru can be substituted up to 7.5 % for Mn in LiMn_2O_4 without any impurity phase.
- Samples with $x=0.025, 0.04, 0.05, 0.06, 0.075, 0.10$ and 0.15 in $\text{LiMn}_{2-x}\text{Ru}_x\text{O}_4$ showed a small increase in lattice parameter, indicating possible substitution of Ru^{4+} in the place of Mn^{4+} .
- Four probe resistivity measurements indicate a hopping conduction both in the frustrated cubic and charge ordered orthorhombic phase in the pristine sample.
- Ambient temperature resistivity of the samples shows a precipitous fall upon substitution of very small amount of Ru ($x=0.025$). The resistivity can be fitted to an exponential fall. It is inferred that the presence of Ru (4d element) with an extended d-orbital leading to an enhanced hopping probability for the e_g electrons from Mn^{3+} may be the reason for this.
- Apart from the decrease in resistivity, there is the diminished hysteresis as Ru is substituted. The decrease in loop area may represent a scenario where the charge re-organization and the lattice response follow each other aided by the extended orbitals of Ru.
- The LTXRD experiments have categorically brought out the fact that the transition from frustration to charge ordering is not destroyed but only suppressed to lower temperature upon Ru substitution. Upon substitution of 5% Ru for Mn in LiMn_2O_4 it is observed that the system has retained frustration down to about 240 K below which it starts undergoing charge order transition to the orthorhombic structure.
- The structural model that is presently available in the literature invokes octagonal columnar ordering of Mn^{4+} ions. Those which are not frozen in the columnar organization are a mixture of Mn^{4+} and Mn^{3+} . Though the extended d-orbitals have

- promoted hopping possibilities, temperature also has a role in curtailing the frustration in this system.
- Presence of Ru certainly plays a role in retaining the charge frustration in this system. But the nature of the role played by Ru can be established only if detailed LTXRD data analysis to extract the bond lengths and bond angle is carried out or a site specific analysis using EXAFS or XANES is carried out.
 - Further work to systematically substitute Fe for Mn is being taken up. Better conclusions can be arrived at if data collection is achieved in the diffractometer mode and without the beryllium interference.

References

- [1] Atsuo Yamada and Masahiro Tanaka, *Mater. Res. Bull.* **30** (1995) 715
- [2] Hirotaka Yamaguchi, Atsuo Yamada, Hiromoto Uwe, *Phys. Rev. B* **58** (1998) 8
- [3] J. B. Goodenough, *Annu. Rev. Mater. Sci.* **28** (1998)1
- [4] J. Rodri'guez-Carvajal, G. Rousse, C. Masquelier, and M. Hervieu, *Phys. Rev. Lett.* **81** (1998) 23
- [5] P. Piszora, J. Darul, W. Nowicki, E. Wolska, *Journal of Alloys and Compounds* **362** (2004) 231
- [6] Rajiv Basu and Ram Seshadri, *J. Mater. Chem.* **10**(2000) 507
- [7] Toshihide Tsuji, Masaki Nagao, Yasuhisa Yamamura, Nguyen Tien Tai, *Solid State Ionics* **154-155** (2002) 381
- [8] E. Wolska, P. Piszora, J. Darul, W. Nowicki, *J. Phys. Chem. Solids* **65** (2004) 223.
- [9] W. Nowicki, *Vol. Acta Phys. Polonica A* **114** (2008) 375
- [10] M. V. Reddy, S. Sundar Manoharan, Jimmy John, Brajendra Singh, G. V. Subba Rao, and B. V. R. Chowdari, *Journal of The Electrochemical Society*, **156** (2009) 652
- [11] A. S. Wills, N. P. Raju, and J. E. Greedan, *Chem. Mater.*, **11** (1999) 1510
- [12] A. de Andre's, M. Garcí'a-Herna'ndez, J. L. Martí'nez, and C. Prieto, *App. Phys. Lett.* **74** (1999) 3884
- [13] J. H. Durrell, C-B. Eom, A. Gurevich, E. E. Hellstrom, C. Tarantini, A. Yamamoto and D. C. Larbalestier *Rep. Prog. Phys.* **74** (2011)124511
- [14] L.J. van der Pauw, *Philips Res. Repts* **13** (1958)1

- [15] Jonathan D. Weiss, Robert J. Kaplar, Kenneth . E. Kambour, Solid State Electronics **52** (2008) 91
- [16]L. M. Wang, Jian-Hong Lai, Jyh-Iuan Wu, Y.-K. Kuo and C. L. Chang, J. Appl. Phys **102** (2007) 023915
- [17] L. Seethalakshmi, V. Sridharan, D.V. Natarajan, V. S. Sastry and T.S. Radhakrishnan, Pramana, Journal of Physics **58** (2002) 1019
- [18] S.R.Kane, C.K. Garg and A.K. Sinha, AIP Conference proceedings **1234** (2010) 683
- [19] <http://www.cat.ernet.in/technology/accel/srul/beamlines/adxrd.html>

CHAPTER 6

Summary of the results and scope for future work

In this thesis two spinel oxides namely AlV_2O_4 and LiMn_2O_4 have been identified as candidate materials for probing the charge ordering from geometrical frustration, largely using structural studies. The inherently geometrically frustrated spinel B sub-lattice relieves the frustration through a structural transition by lowering the cubic symmetry. This thesis focuses on the role of external pressure in retaining the charge order in AlV_2O_4 . In the case of LiMn_2O_4 , instead of external pressure, the role of partial substitution in the B sub-lattice in altering the structural transition is examined. The following sections summarise the results and indicate studies that must be taken up for deepening further understanding of the mechanism of charge ordering from frustration in this rare class of materials.

6.1 Structural transition under high temperature and high pressure in AlV_2O_4

6.1.1 *Rhombohedral (charge ordered) to cubic (charge frustrated) transition on application of temperature*

AlV_2O_4 is unique since it presents itself in the charge ordered state at ambient temperature. For the present thesis, AlV_2O_4 is synthesized using the solid state reaction route. The ambient temperature powder XRD data is indexed to the heptamer structural model. Rietveld refinement of the ambient temperature, slow scan powder data shows the room temperature structure of AlV_2O_4 to be R-3m. The lattice parameters obtained are: $a = b = 5.7613(2) \text{ \AA}$ and $c = 28.6876(10) \text{ \AA}$ and the cell volume is $824.65(4) \text{ \AA}^3$. It is also

observed from the present Rietveld refinement that there are two V3-V3 bond distances as suggested in the literature. This corresponds to the distortion of the kagome' lattice sustaining the charge ordered structure. High temperature powder diffraction measurements show transition from rhombohedral to cubic (Fd-3m) phase between 763 and 773 K. It is observed that the d-spacing corresponding to the (0 2 16) plane shrinks on heating before transforming to the cubic phase. This clearly brings out the role of vanadium orbitals in enabling the formation of V3 trimers resulting in the charge ordered heptamer molecular units in the low temperature rhombohedral phase.

6.1.2 Observation of pressure induced frustration on charge ordered state

Powder diffraction experiments under high pressure using diamond anvil cell have been carried out under non-hydrostatic and hydrostatic conditions. AlV_2O_4 transforms from the charge ordered rhombohedral phase at ambient pressure to the charge frustrated cubic spinel phase on application of pressure. Pressure, at which the transition is brought about, remains similar (21-23 GPa) in the case of non-hydrostatic as well as hydrostatic pressure situations. While application of non-hydrostatic pressures locks AlV_2O_4 irreversibly in the frustrated cubic phase even after decompression, decompression from hydrostatic pressure reversibly takes the system back to the rhombohedral (charge ordered) phase. The heptamer model proposed in the literature invokes overlap of vanadium orbitals for the formation of charge ordered clusters. These clusters form with a slight readjustment of the position of vanadium from the parent cubic phase. Application of pressure probably affects the orbital overlap and retains frustration. Further, since pressure and temperature prefer the system to be in the disordered/frustrated cubic phase, it may be conjectured that there exists a critical range

of strain for the planes involving the kagome` lattice of vanadium (V3), beyond which the delicately balanced orbital overlap must be getting inhibited, destroying the heptamer clusters and driving the system back to frustration.

6.2 Charge state of vanadium in the charge ordered rhombohedral AlV_2O_4

6.2.1 Charge state of vanadium in the charge ordered phase examined using electron energy loss spectroscopy

Heptamer clustering of vanadium in the charge ordered state is currently agreed upon. But, different values are suggested in the literature for the charges on the three different vanadium forming the heptamer and on the non-bonding loner. White line ratio and O-K edges of V_2O_5 , VO_2 , V_2O_3 and AlV_2O_4 obtained using electron energy loss spectroscopy (EELS) are analyzed specifically to probe the VO_6 octahedra in all of them. The systematic decrease of the L_2 intensity and the O-K edge intensity from V^{5+} in V_2O_5 to AlV_2O_4 indicates a progressive increase in the occupancy of the hybridized states. The absence of transition from $O-1s$ to hybridized $^2t_{2g}$ indicates partial filling of all the vanadium orbitals. This would mean that vanadium in the charge ordered rhombohedral phase has charge states lower than 3. Density functional calculations have been carried out to corroborate this.

6.2.2 ab-initio band structure calculation on the rhombohedral (charge ordered) and cubic (frustrated) AlV_2O_4

Band structure calculations carried out on the frustrated cubic and the charge ordered rhombohedral phase clearly bring out opening of a gap in the charge ordered phase and a semi metallic state in the cubic phase. Density of states of V3 ions forming the kagomé plane seems to have a prominent contribution at the Fermi energy. However,

contributions from all the V1, V2 and V3 are present. The bond valence sum estimation from the band structure calculation indicate that the charge state of V in the rhombohedral phase must be $V2 > V3 > V1$. This contradicts the $V1 > V3 > V2$ picture from the heptamer model

Structural information available from literature and from this work, the absence of O-K edge ($1s$ to $\pi^* 2t_{2g}$) EELS, it appears that the charge state on all vanadium may be deviating from integral values indicating probably a partial orbital occupancy and non trivial ordering. Hence, though the charge ordered rhombohedral phase may be formed by the clustering of vanadium largely due to direct vanadium-vanadium orbital interaction as heptamer unit, charge state on vanadium atoms needs detailed reassessment.

6.3 Structural transition on Ru substitution in LiMn_2O_4

Ru can be substituted up to 7.5 % for Mn in LiMn_2O_4 without any impurity phase. Samples with $x=0.025, 0.04, 0.05, 0.06, 0.075, 0.10$ and 0.15 in $\text{LiMn}_{2-x}\text{Ru}_x\text{O}_4$ showed a small increase in lattice parameter, indicating possible substitution of Ru^{4+} in the place of Mn^{4+} .

6.3.1 Tracing the charge order transition using four probe resistance

Four probe resistance measurements indicate a hopping conduction both in the frustrated cubic and charge ordered orthorhombic phase in the pristine sample. Ambient temperature resistivity of Ru substituted samples shows a precipitous fall upon substitution of very small amount of Ru ($x=0.025$). The resistivity can be fitted to an exponential fall. This may be because of the presence of Ru (4d element) with an extended d-orbital leading to an enhanced hopping probability of the e_g electrons from Mn^{3+} . Apart from the decrease in resistivity, there is the diminished hysteresis as Ru is

substituted. The decrease in loop area indicates that charge re-organization and lattice response follow each other aided by the extended orbitals of Ru.

6.3.2 The competing role of Ru and temperature in the charge ordering of LiMn_2O_4

The LTXRD experiments have categorically brought out the fact that the transition from frustration to charge ordering is not destroyed but only suppressed to lower temperature upon Ru substitution. Upon substitution of 5% Ru for Mn in LiMn_2O_4 it is observed that the system has retained frustration down to about 240 K below which it starts undergoing charge order transition to the orthorhombic structure. The structural model that is presently available in the literature invokes octagonal columnar ordering of Mn^{4+} ions. Those which are not frozen in the columnar organization are a mixture of Mn^{4+} and Mn^{3+} . Though the extended d-orbitals have promoted hopping possibilities, temperature also has a role in curtailing the frustration in this system. Presence of Ru certainly plays a role in retaining the charge frustration in this system. But the nature of the role played by Ru and the mechanism through which temperature takes control of resuming order from frustration can be established only if detailed LTXRD data analysis to extract the bond lengths and bond angle is carried out. This requirement is important since the charge ordered unit cell is highly complex and the nature of charge ordering is exotic.

6.4 Further studies on the charge ordering in spinel system

Charge ordering from frustration in spinels is in fact in its infancy. Very few systematic studies are available in the literature. The cubic structure itself has 56 atoms in its unit cell and the charge ordered structures in general contain even more number of

atoms making computation intensive. In all the charge frustrated spinels the ordering that relieves the frustration is supposed to be brought about by ordering of the orbitals. Of late, resonant X-ray diffraction is emerging as a technique to probe the charge and orbital ordering. Since polycrystalline pellets can be used for such experiments, carrying out the resonant diffraction experiment can enhance understanding of the role of orbitals.

It is proposed based on the studies under this thesis that vanadium is present with non-integral charge state in the charge ordered phase with partially occupied orbitals. This is bound to have implication in the magnetic state of AlV_2O_4 . Further detailed measurements, probing the global and local magnetic moments are essential to reach an interpretation involving the partially occupied orbitals. Magnetic resonance inelastic scattering experiments on very good quality single phase specimens will enable better clarity on the nature of orbital ordering and occupancy in systems like AlV_2O_4 which are exotic and complex.

In the case of AlV_2O_4 there is just one work on substitution of chromium for vanadium. It is not clear at the moment if any other ion will replace vanadium in the B sub-lattice. High pressure experiments are almost not available in the charge frustrated spinel compounds. It is considered high pressure experiments are cleaner than substitution experiments. While the present thesis has categorically shown that pressure induces frustration in AlV_2O_4 , to generalise the role of pressure, it is essential to carryout high pressure measurements on the charge ordered state of other spinel oxides. EXAFS under high pressure can provide more information about the local structural modification of the chosen B ion. Such high pressure experiments on clean samples will be able to indicate the nature of interaction that brings about clustering and formation of valence

bond solid state in these systems. It can also aid direct observation of the role of Ru orbitals in suppressing the transition in LiMn_2O_4 . The octagonal ordering suggested in the literature is still intriguing. Since synthesis of the sample is easy, with due care for oxygen stoichiometry, high pressure experiments in the charge ordering state can give a better detail about the nature of interaction. LiRh_2O_4 is the most recent compound to show charge ordering from frustration and still remains largely under explored. Since the synthesis is a bit involved requiring high pressure, first of all effort must be expended to prepare phase pure samples and then the nature of charge ordering must be explored using the conventional and non-conventional techniques. Though the field is growing slowly, recognition that the orbitals play a major role in ordering the charges has given fresh impetus and it is expected that the forth coming years will see a lot of synchrotron beam time apportioned for understanding these interesting systems.

LIST OF PUBLICATIONS

Publications in Peer reviewed Journals

1. *Pressure-induced frustration in charge ordered spinel AlV_2O_4*
S. Kalavathi, Selva Vennila Raju, Quentin Williams, P.Ch. Sahu, V. S. Sastry and H. K. Sahu
Fast Track Communication: J. Phys.: Condens. Matter **25** (2013) 292201
2. *Synthesis, Characterization and Observation of Structural Transformation in AlV_2O_4*
S. Kalavathi, B. Thamilarasi, H. K. Sahu and V.S. Sastry
AIP Conference Proceedings **1349** (2011) 1307
3. *Valence state, hybridization and electronic band structure in the charge ordered AlV_2O_4*
S. Kalavathi, S. Amirthapandian, Sharat Chandra, P. Ch. Sahu and H. K. Sahu
J. Phys.: Condens. Matter **26** (2014) 015601

Publications in Journals (not included in the thesis)

1. Effect of ionic-size change of the rare earth ion on the electrical properties of the hole doped double perovskite $\text{Gd}_{0.95}\text{Sr}_{0.05}\text{BaCo}_2\text{O}_{5.5}$
J.Janaki, V. Rajaji, T. Geetha Kumary, **S. Kalavathi** and A. Bharathi
57 th DAE Solid State Physics Symposium, Mumbai
(AIP conference proceedings **1512** (2013) 924-925)
2. Blue green and UV emitting ZnO nanoparticles synthesized through non-aqueous route
M. Rajalakshmi, S. Sohila, S. Ramya, R. Divakar, Chanchal Ghosh and **S. Kalavathi**
Optical Materials **34** (2012) 1241–1245
3. Influence of Ni doping on the electrical and structural properties of FeSb
J. Janaki, Awadhesh Mani, A. T. Satya , T. Geetha Kumary, **S. Kalavathi** and A. Bharathi
Phys. Status Solidi B, **249** (2012) 1756
4. Synthesis, characterization and evaluation of titanium carbonitride surface layers with varying concentrations of carbon and nitrogen
P.K. Ajikumar, M. Kamruddin, **S. Kalavathi**, A.K. Balamurugan, S. Kataria, P. Shankar, A.K. Tyagi
Ceramics International **38** (2012) 2253–2259
5. Effect of reactive gas composition on the microstructure, growth mechanism and friction coefficient of TiC overlayers
P. K. Ajikumar , M. Vijayakumar, M. Kamruddin, **S. Kalavathi**, N. Kumar, T.R. Ravindran, A.K. Tyagi
Int. Journal of Refractory Metals and Hard Materials **31** (2012) 62– 70
6. A study on the redistribution of ion-implanted nitrogen in Ti-modified austenitic steel
J. Arunkumar,, C. David, C. Varghese Anto, K.G.M. Nair, **S. Kalavathi**, R. Rajaraman, G. Amarendra, B.K. Panigrahi, P. Magudapathy, John Kennedy
Journal of Nuclear Materials **414** (2011) 382–385
7. Synthesis and Characterization of SnS Nanosheets Through Simple Chemical Route
S. Sohila, M. Rajalakshmi, C. Muthamizhchelvan, **S. Kalavathi**, Chanchal Ghosh, R. Divakar, C. N. Venkiteswaran, N.G. Muralidharan, A. K. Arora, and E. Mohandas.
Materials Letters **65** (2011) 1148-1150

8. Specific heat studies on pristine and oxygenated iron tellurides
Awadhesh Mani , J. Janaki, T. Geetha Kumary, N. Thirumurugan,
S. Kalavathi, and A. Bharathi
Solid State Communications **151** (2011) 1210
9. Formation of embedded Indium nano clusters in Silica and their stability
under thermal treatment and ion irradiation
P. Santhana Raman, K.G.M. Nair, Jay Ghatak, Umananda M. Bhatta,
P.V. Satyam, **S. Kalavathi**, B.K. Panigrahi and V. Ravichandran
J. Nano Sci. Nano Tech **10** (2010) 755
10. Intermixing and formation of Pd-V-Mg intermetallics in Pd/Mg/Si films
G.L.N. Reddy, Sanjiv Kumar, Y. Sunitha, **S. Kalavathi**, V.S. Raju
Journal of Alloys and Compounds **481** (2009) 714-718.
11. Positron annihilation and X-ray diffraction studies on tin oxide thin films
K. Prabakar, S. Abhaya, R. Krishnan, **S. Kalavathi**, J. Jayapandian,
G. Amarendra
Nuclear Inst. and Methods in Physics Research, **267 B** (2009) 1167
12. Phonon confinement and substitutional disorder in $Cd_{1-x}Zn_x$ S nano crystals
Satyaprakash Sahoo, S. Dhara, V. Sivasubramanian, **S. Kalavathi** and
A.K. Arora
J. of Raman Spectroscopy, **40** (2009) 1050
13. Structure and Photoluminescence properties of ion beam synthesized SiC
nano Particles in Si
K. Saravanan, B. K. Panigrahi, S. Amirthapandian, **S. Kalavathi**,
A. K. Srivastava and K. G. M. Nair
J. of Nano science and Nano Technology **9** (2009) 5523
14. Effect of flowing sodium on corrosion and tensile properties of AISI type
316 LN Stainless Steel at 823 K
N. Sivai Bharasi , K. Thyagarajan , H. Shaikh , A.K. Balamurugan,
Santanu Bera, **S. Kalavathi** , K. Gurumurthy , A.K. Tyagi , R.K. Dayal ,
K.K. Rajan , H.S. Khatak
Journal of Nuclear Materials **377** (2008) 378–384
15. Amorphous to crystalline induced $CoSi_2$ phase formation in Co-implanted Si
S. Abhaya, G. Amarendra, **S. Kalavathi**, B.K. Panigrahi, S. Saroja,
K.G. M. Nair, V. S. Sastry, and C. S. Sundar
Eur. Phys. J. Appl. Phys. **41**(2008) 107–110
16. Multiphonon Raman scattering in GaN nanowires
S. Dhara, Sharat Chandra, G. Mangamma, **S. Kalavathi**, P. Shankar,
K. G. M. Nair, A. K. Tyagi , C. W. Hsu, C. C. Kuo, L. C. Chen, and

K. H. Chen, K. K. Sriram
Applied Physics Letters **90** (2007) 213104

17. Realisation of magnetic anisotropy and $L1_0$ CoPt ordered phase by Pt ion irradiation on a Co/ Pt bilayer film
S. Balaji, S. Amirthapandian, B. K. Panigrahi, **S. Kalavathi**, Ajay Gupta and K. G. M. Nair
Journal of Physics: Condensed Matter, Volume **19** (2007) 356211
18. Synthesis and characterization of a granular Fe–Ge layer by ion implantation and subsequent ion beam annealing
S. Amirthapandian, B. K. Panigrahi, M. Rajalakshmi, **S. Kalavathi**
B. Sundaravel, Gupta Ajay and A. Narayanasamy
Journal of Physics: Condensed Matter, **19** (2007) 096003
19. Raman scattering studies of cobalt nano clusters formed during high energy implantation of cobalt ions in a silica matrix
P. Gangopadhyay, T. R. Ravindran, K. G. M. Nair, **S. Kalavathi**,
B. Sundaravel and B. K. Panigrahi
Applied Physics Letters, **90** (2007) 063108
20. Pressure-induced amorphization and decomposition in ZrV_2O_7 :
A Raman spectroscopic study
T. Sakuntala, A. K. Arora, V. Sivasubramanian, Rekha Rao,
S. Kalavathi and S. K. Deb
Phys. Rev. B, **75** (2007) 174119